11-2017

Development of Cardiac Atrial Kick Shear Wave Elastography to Assess Myocardial Stiffness

Aaron J. Engel
University of Nebraska-Lincoln, aaronjengel@gmail.com

DEVELOPMENT OF CARDIAC ATRIAL KICK SHEAR WAVE ELASTOGRAPHY TO ASSESS MYOCARDIAL STIFFNESS

by

Aaron J. Engel

A DISSERTATION

Presented to the Faculty of

The Graduate College at the University of Nebraska

In Partial Fulfillment of Requirements

For the Degree of Doctor of Philosophy

Major: Engineering

(Biomedical Engineering)

Under the Supervision of Professor Gregory R. Bashford

Lincoln, Nebraska

November, 2017

DEVELOPMENT OF CARDIAC ATRIAL KICK SHEAR WAVE ELASTOGRAPHY TO ASSESS MYOCARDIAL STIFFNESS

Aaron J. Engel, Ph.D.

University of Nebraska, 2017

Advisor: Gregory R. Bashford

Increased myocardial stiffness, which is characteristic of many cardiovascular diseases, leads to a loss of diastolic function and is a cause of diastolic heart failure. Current methods to estimate myocardial stiffness rely on pressure-volume relationships derived from invasive cardiac catheter measurements. Noninvasive methods to estimate myocardial stiffness include ultrasound-based and magnetic resonance-based shear wave elastography, where the stiffness of the tissue is related to the propagation speed of a shear wave. Currently, ultrasound-based cardiac shear wave elastography includes acoustic radiation force based methods; however, the *in vivo* generation and detection of the shear waves in myocardium is significantly degraded due to limited acoustic radiation force penetration and clutter noise introduced from the chest wall. A similar degradation of shear waves occurs in cardiac magnetic resonance elastography because of the external source used for shear wave generation. Consistently successful cardiac shear wave elastography is limited to patients with a thin chest wall and low body mass index. To meet the needs of the patients suffering from diastolic heart failure, the long-term goal of this research is to develop a cardiac shear wave elastography technique where the shear wave is

generated within the heart by the mechanical stimulus of the late diastolic atrial kick. The amplitude of this wave is at least one order of magnitude higher than acoustic radiation force induced shear waves and thus more easily visualized, having a higher chance of detection in a broader patient population. This dissertation introduces a method for shear wave speed estimation in shear wave elastography and compares it to conventional methods. A method termed cardiac atrial kick shear wave elastography is introduced to measure the atrial kick shear wave speed. A pilot study was performed using this method which measured the atrial kick shear wave speed and compared it to common measures of cardiac health taken at the clinic and in conventional echocardiogram reports. Results suggest that cardiac atrial kick shear wave elastography is a promising tool that can be used for assessment of diastolic function and myocardial stiffness.

Dedication

For my parents, Jay and JoAnn Engel, you have always been there. Without you, I would not be so curious about the world and I would not be so stubborn in my pursuits. Through you, I learned that we are capable of far more than we know.

Sob bakhair, azizam! Man ba qadre kaafee kalema soraagh nadaaram taa begoyam chiqadar dostat daaram. Az Hameen khaater ba takraar wa har roz megoyam ke tora har roz wa hamesha dost daaram. Man zolfhaye chang wa labkhandat raa dost daaram. Man qawaara kardanhaae shirin wa nahaaye raa ke sareman memaani, dost daaram. Harbaar toraa mebinam, az sardobaara aasheqat meshawam. Bazoodee baazham mebinamat, azizam! Roz we khoshe baraayat aarzo mekonam.

Acknowledgements

I would like to extend my deepest thanks to my advisor Greg Bashford for his guidance and support through my graduate experience. Thank you for believing in me and taking a chance on me. Thank you to my committee members Michael Hoffman, Pengfei Song, Jeyamkondan Subbiah, and Joseph Turner for offering thoughtful and valuable feedback on my endeavors throughout the years. It has been a pleasure to learn from all of you.

Thank you to my labmates past and present: Tiantian Xu, Mohammed Alwatban, Max Twedt, Ben Hage, Mohsen Hozan, and Lauren Wondra. It was an honor to work with you all. Thank you to all the undergraduates who've been more than willing to jump into research and work alongside us. Thank you to the Chase Hall staff Diann Young, Bonita "Bo" Delhay, and Ronica Stromberg for your help through the years with administrative work. You make it easier for all of us. Thank you to my friends Tim Martin, Chase Pfeifer, Eric Lund, Vasu Sharma, María Gabriela "Gaby" Arellano Bello and the many others who supported me and allowed me to have a life outside the lab. Thank you all.

Table of Contents

List of Symbols and Abbreviations

A’	Peak tissue velocity in Late Diastole
ACC	American College of Cardiology
AHA	American Heart Association
ANOVA	Analysis of Variance
ARF	Acoustic Radiation Force
AV	Atrio-ventricular
BMI	Body Mass Index
BSA	Body Surface Area
CC	Cross-Correlation
CNR	Contrast-to-Noise Ratio
CVD	Cardiovascular Disease
DD	Diastolic Dysfunction
DHF	Diastolic Heart Failure
E’	Peak tissue velocity in Early Diastole
ECG	Electrocardiogram
ECM	Extracellular Matrix
EF	Ejection Fraction
IQ	In-phase and Quadrature
IRB	Institutional Review Board
IVRT’	Isovolumetric Relaxation Time
IVS	Interventricular Septum
LA	Left Atria

LV	Left Ventricle
MAE	Mean Absolute Error
MRI	Magnetic Resonance Imaging
PI	Pulse Inversion
PRF	Pulse Repetition Frequency
PSD	Power Spectral Density
RA	Right Atrium
RF	Radio Frequency
ROI	Region of Interest
RV	Right Ventricle
S’	Peak tissue velocity in Systole
SNR	Signal-to-Noise Ratio
STFFT	Short-time Fast Fourier Transform
SWE	Shear Wave Elastography
SWS	Shear Wave Speed
TDI	Tissue Doppler Imaging
TOF	Time-of-Flight
TTP	Time-to-Peak

List of Tables

List of Figures

Chapter 1.

Introduction

1.1. Elastography: Imaging the Stiffness of Tissues

Hippocrates, often considered the father of modern medicine, advocated for the study of disease by means such as palpation and auscultation, touching and listening to the body for signs of abnormalities. From studies on the character of the swelling of the body he concluded that, “Swellings that are painful, big and hard, indicate a danger of death in the near future; such as soft and painless, yielding to the pressure of the finger, are of a more chronic character (Katz and Katz 1962).” Nearly 2500 years ago, Hippocrates demonstrated and wrote that the stiffness of the tissue was a characteristic feature allowing for differentiation of disease. To this day physicians palpate the surface of the body, searching for abnormalities, trusting their experience to guide their judgment in the treatment of their patients.

Elastography, in this manner, has been carried out for over two millennia. Physicians probe the surface of the body with their fingers and visualize abnormalities within the eyes of their mind. Yet, a flaw in this technique is the fingers are always on the surface of the body and complex structures deep within the body cannot be easily visualized. Medical imaging techniques such as X-ray, ultrasound, and magnetic resonance imaging (MRI) extended the eyes of the physician into the body, to see what could not be seen.

While truly "feeling" (with human senses) beneath the skin is not currently possible, it is possible to use the methods developed to see beneath the surface, such as ultrasound, to extend the fingers of the physician past the surface and further into the body, to feel what could not be felt. The research conducted and presented in this dissertation investigates the mechanical properties of tissues through the use of ultrasound imaging. To help explain this, the remainder of this section presents a brief introduction of ultrasound imaging and its progression into elastography as a tool to visualize the mechanical properties of tissues.

Ultrasound is a noninvasive imaging modality which uses high frequency sound waves to visualize the internal structures of the body. Its roots reach back to the mid 1900's in sonar as a method to detect objects beneath the surface of water and then as a method of nondestructive testing through the use of a handheld "reflectoscope" (Firestone 1946). This paved the way for ultrasound research of the human body with medical applications such as the investigation of fetal growth (Donald et al. 1958) and cardiac anatomy and movement (Edler and Lindström 2004). Figure 1.1 shows an image of a heart taken with ultrasound imaging methods presented in Chapter 2. Here, the tissue structure and muscle appear bright and are delineated from the blood which has a darker appearance.

A next natural step after visualization of the internal structure of tissues is to visualize deformation to the internal structures. Analysis of deformations using

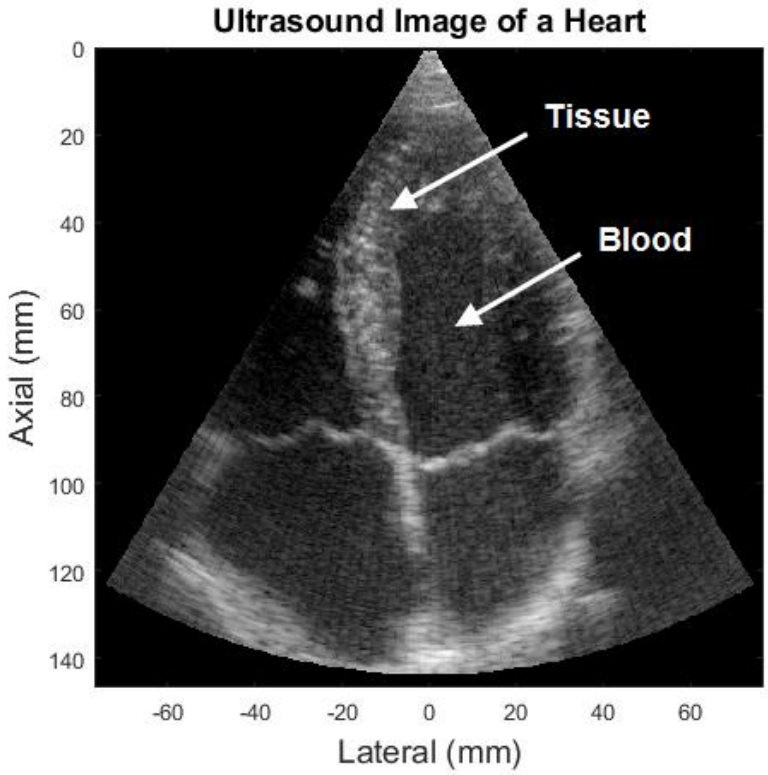

Figure 1.1 Ultrasound image of the heart showing 4 chambers. Overall the image has a "grainy" appearance. The muscle of the heart has a brighter image response while the blood appears as a darker region.

ultrasound imaging allows for the nondestructive and noninvasive evaluation of the mechanical properties of tissues. This is important because often the ultrasonic visualization of tissue structure of not a good indicator of the physiological or pathologic condition of the tissue (Wagner et al. 1983; Wagner et al. 1988). This is shown in Figure 1.2 where a traditional ultrasound image fails to adequately visualize a hard inclusion embedded in a soft tissue phantom; however, the corresponding elastography image is able to visualize the hard inclusion and shows the clinical viability and necessity of elastography.

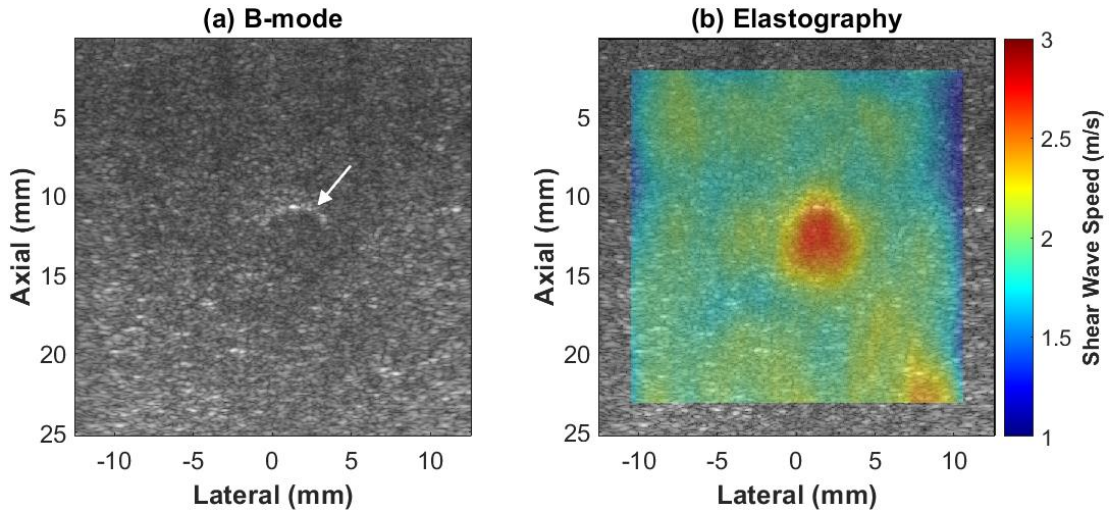

Figure 1.2 Example of inclusion phantom where a hard inclusion is inserted into a soft background. (left) A traditional ultrasound image. The inclusion is difficult to visualize. (right) Elastography type image where the inclusion is better visualized. Imaged using a Verasonics Vantage with a method developed in Chapter 3.

Ultrasound-based elastography is becoming more widely used in the clinic (Shiina et al. 2015), and different methods have been used for various clinical applications including the staging of liver fibrosis (Nightingale et al. 2015; Palmeri et al. 2008; Sandrin et al. 2003) and breast cancer (Barr et al. 2015; Evans et al. 2010), the assessment of the condition of the musculoskeletal system (Brum et al. 2014; Cortes et al. 2016; Eby et al. 2013), the quantification of arterial stiffness in the progression of atherosclerosis (Apostolakis et al. 2016; Bernal et al. 2011; Maksuti et al. 2015), and the investigation of the stiffness and orientation of the fibers in the myocardium (Couade et al. 2011; Pernot et al. 2011; Song et al. 2016b).

In addition to ultrasound-based elastography, magnetic resonance elastography (MRE) is proving to be a useful tool for the visualization of tissue stiffness (Muthupillai et al. 1995; Muthupillai and Ehman 1996). MRE is being actively developed for clinical applications in tissues such as the liver (Venkatesh et al. 2013), the brain (Kruse et al. 2008; Manduca et al. 2001), the lung (Mariappan et al. 2012), and the heart (Elgeti et al. 2010; Elgeti et al. 2014; Wassenaar et al. 2016).

As a noninvasive method for mechanical testing of tissue, elastography methods work by first disturbing the tissue in some way and then evaluating and quantifying the response (Greenleaf et al. 2003). The methods previously implemented use an external disturbance such as a compression (O'Donnell et al. 1994; Ophir et al. 1991), vibration (Parker et al. 1990; Yamakoshi et al. 1990; Zhao et al. 2014), or a push from an extended burst of sound from the ultrasound transducer (Bercoff et al. 2004; Chen et al. 2009; Sarvazyan et al. 1998). However, in some cases the disturbance can be applied not only from an external source, but also from normal physiological motions (Konofagou et al. 2011; Pernot et al. 2007). This is usually limited to motion produced from the beating of the heart. While ultrasound-based elastography has been performed by analyzing the disturbances produced by heart valve closures (Kanai 2005; Strachinaru et al. 2017; Vos et al. 2017), and the propagation of the electrical activation of muscle contraction (Provost et al. 2011; Provost et al. 2013), there has been little development of cardiac

elastography which use the disturbances caused by muscle contractions (Pislaru et al. 2014).

1.2. Long Term Goal of Research

The long-term goal of this research is to develop an ultrasound based elastography method—using the cardiac muscle contraction as the impulse for tissue deformation—to noninvasively assess the *in vivo* stiffness of the heart. This is clinically relevant for a variety of cardiac pathologies including damage from myocardial ischemia and infarction, and hypertrophic cardiomyopathy. As these conditions progress, there is a loss of cardiac function, and this can result in Diastolic Heart Failure (DHF).

1.3. Contribution of Research in this Dissertation

To meet the long-term goal to develop a cardiac elastography method to assess myocardial stiffness, this dissertation is organized as follows:

Chapter 2 provides the clinical motivations for this research, introduces the anatomy and physiology of the heart, and shows how increases in myocardial stiffness can result in DHF. From this, a more in-depth exploration of ultrasound-based elastography is provided. The traditional methods and theory behind elastography as a technique to measure the *in vivo* stiffness of tissues will be explored.

Chapter 3 demonstrates the ability of ultrasound elastography to characterize and image the stiffness of tissues. The response from an external

vibration to the surface of tissue mimicking ultrasound phantoms having different stiffness is imaged and quantified. A method is developed which provides an accurate estimation of tissue stiffness in a 2D space and allows the visualization of stiffness overlaid on a traditional ultrasound B-mode image.

Chapter 4 introduces Cardiac Atrial Kick Shear Wave Elastography as a method to estimate the *in vivo* stiffness of the heart. Here, the stimulus for tissue deformation is not an external vibration as in Chapter 3, but rather the contraction of a section of the myocardium on one side of the heart which produces movement on an adjacent section of passive and non-contracting myocardium. An *in vivo* study was performed which correlated the result from the elastography measurement to conventional measures of health.

Chapter 5 summarizes the research in this dissertation and proposes future research. This includes the investigation of different methods used to visualize tissue movement using ultrasound and a method to measure the stiffness of the heart from vibrations caused by the closure of heart valves.

Chapter 2.

Background Information and Literature Review

2.1. Clinical Motivation

Aristotle identified the heart as the most important organ in the body, life begins and ends with the beating of the heart (Peck 1942). Centuries later, the physician William Harvey proposed in his work, "On the Motion of the Heart and Blood in Living Beings (1628)", that blood flows in a circle throughout the body and that the heart, being the center of the circulatory system, was the driving force responsible for pumping blood throughout the body. The disruption or impairment of this driving force has significant negative outcomes, thus diseases of the heart are the leading cause of death in the United States (Heron 2016).

The work presented in this dissertation demonstrates an ultrasound-based cardiac elastography method to help reduce the burden that these diseases place on society. To understand how ultrasound elastography fits into the initial clinical diagnosis and evaluation of cardiac diseases, it is necessary to first discuss the normal form and function of the heart. Then, with an understanding of a healthy heart, the pathological heart is investigated. Specifically, the condition of the heart as it relates to DHF is discussed and the need for the development of methods which quantify myocardial stiffness is presented. This chapter ends with an in-depth analysis of the possible methods which may be used to estimate myocardial stiffness.

2.2. The Circulatory System

The body requires a near constant supply of oxygen and nutrients in order to survive. Blood is the carrier for these nutrients and flows through a network of vessels to reach and perfuse nearly every tissue within the body. A simplified version of this network, or circulatory system, is shown in Figure 2.1. This total circulatory system is composed of two smaller circulatory systems in a type of double loop configuration. One loop is composed of the heart-lung or pulmonary circulatory system, while the other loop is the heart-body or systemic circulatory system.

2.2.1. Pulmonary circulation

The pulmonary circulation, the top loop in Figure 2.1, is responsible for regulating the exchange of deoxygenated blood into oxygenated blood. The deoxygenated blood flows from the heart through the pulmonary artery and into the lungs where it moves through a network of alveolar capillaries. Alveoli are small gas filled sacs, air pockets in the lung, and the site for the gas exchange of the pulmonary circulation. Specifically, as blood passes through the alveolar capillaries, carbon dioxide which saturates the blood is replaced with the oxygen contained in the alveoli. After the gas exchange, the oxygenated blood then returns back to the heart through the pulmonary vein so it may enter the systemic circulation.

2.2.2. Systemic circulation

The systemic circulation, the bottom loop of Figure 2.1, is the network of arteries and veins which work to supply oxygen and nutrients to the body. This system begins at the heart with the oxygenated blood having just exited the pulmonary circulation. As the heart muscle contracts, blood flows out of the heart to the body through the aorta. The aorta then branches off into a large network of arteries which sends blood to the separate parts of the body. With more and more branching the vessels get smaller and smaller until blood is forced through capillaries where oxygen and nutrients gets exchanged for carbon dioxide and waste products. Following this, blood then flows through veins to return to the heart and enters the pulmonary circulation where the process begins again.

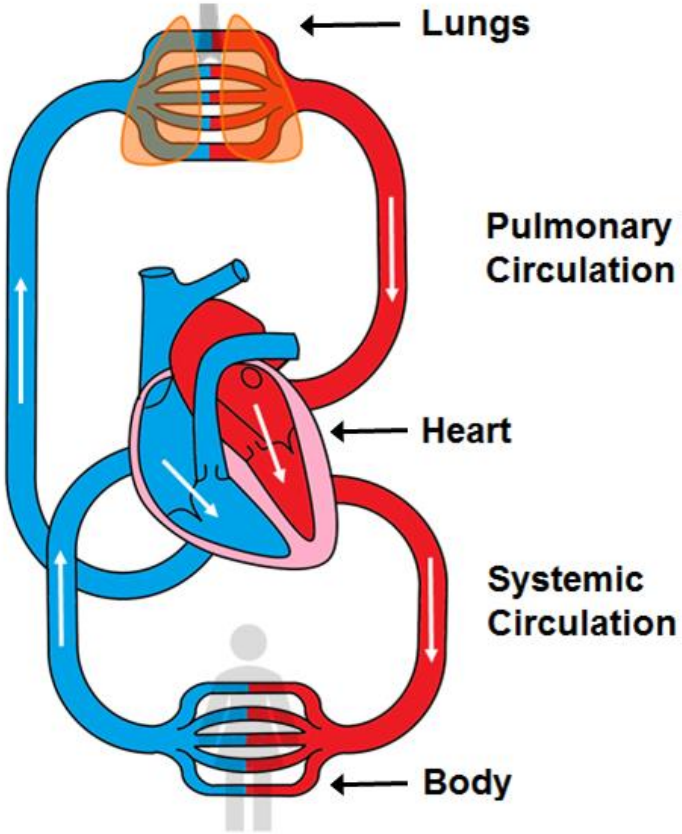

Figure 2.1 Simplified Circulatory System. The upper loop represents the pulmonary circulation from heart to lungs where blood is oxygenated. The lower loop represents the systemic circulation from the heart to the body where blood transfers oxygen to the tissue.

2.3. Cardiac Anatomy

The cardiac anatomy, the center of the circulatory system, can be defined by the type of function it is asked to perform and the pathway for blood in the body. The pathway for blood was shown as a double looping circulatory system consisting of the pulmonary and systemic circulations, where blood passes through the heart once for each loop. Because of this, there are two sides for the heart, two separate pumps for each circulatory system. These two pumps are

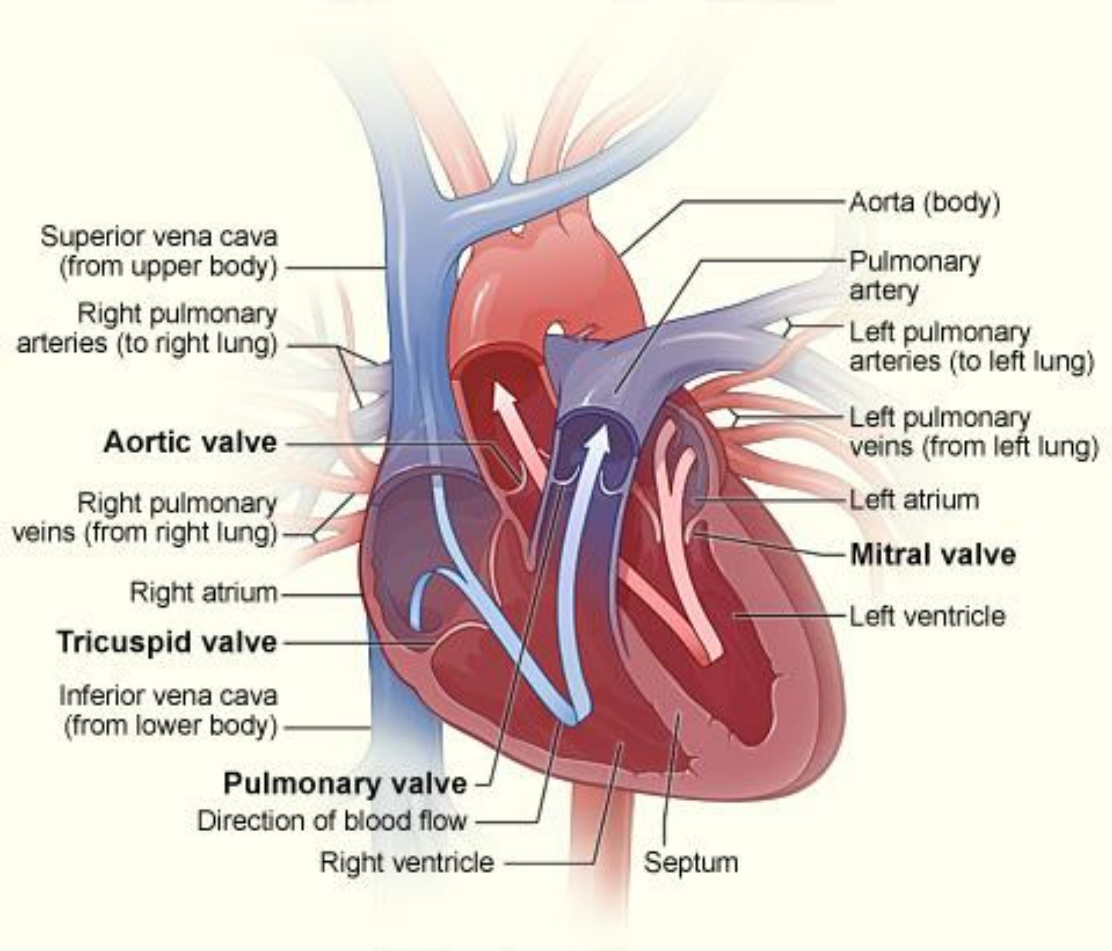

Figure 2.2 Cardiac anatomy. From nhlbi.nih.gov.

simply called the right heart and left heart. The right heart is responsible for the movement of deoxygenated blood into the pulmonary circulation while the left is responsible for the movement of oxygenated blood into the systemic circulation.

Figure 2.2 shows the cardiac anatomy in a more in-depth manner than shown in Figure 2.1. The orientation of the heart and the blue and red coloring of arteries and veins are similar. Two chambers can be seen when looking at one side of the heart. These are the smaller “receiving” chamber, the atrium, and the larger “pumping” chamber, the ventricle. The atrium is responsible for collection of

blood as it returns to the heart, through the veins, from the body or the lungs. The ventricle is responsible for the delivery of blood away from the heart through arteries. Together, the four chambers of the heart are the right atrium (RA), right ventricle (RV), left atrium (LA), and left ventricle (LV). The part of the myocardium which separates chambers is the septum. The interventricular septum (IVS) separates the LV and the RV.

Within the heart there are four valves which regulate the movement of blood through the circulatory system and prevent backflow. In order and along the pathway of blood returning from the body and filling into the RA, the valves are **1)** the tricuspid valve, separating the RA from the RV, **2)** the pulmonary valve, separating the RV and the pulmonary artery, **3)** the mitral valve separating the LA from the LV, and **4)** the aortic valve separating the LV from the aorta. The opening and closing of these valves allow the chambers of the heart to collect and store blood during the different phases of the heart cycle.

2.3.1. Cardiac Functions—Systole and Diastole

The pulsatile manner in which the heart drives blood through the circulatory system suggests that there are two main phases of the heart cycle—an "on" phase and an "off" phase. The on phase is termed systole, and reflects the active contraction of the ventricles as they work to pump blood toward either the lungs (from the RV) or the body (from the LV). Both the RV and LV pump approximately equal amounts of blood during the systolic phase of the heart cycle.

Following systole is the off phase termed diastole. This phase is considered the resting or relaxing phase of the heart where the ventricles fill up with blood which will later be pumped out during systole. The contraction of systole followed by the relaxation of diastole allows the heart to work as a pump and ensures the body is supplied with sufficient oxygen and nutrients to sustain life.

Figure 2.3 shows ultrasound images of the heart which illustrate the differences in the heart between systole and diastole. These were taken using an apical 4-chamber view which allows for identification of all four chambers of the heart and the valves which separate them. The ventricles are noticeably larger during diastole as they are filling with blood. The IVS is in the middle of the image and appears thicker during systole. It is thinned and elongated downward during

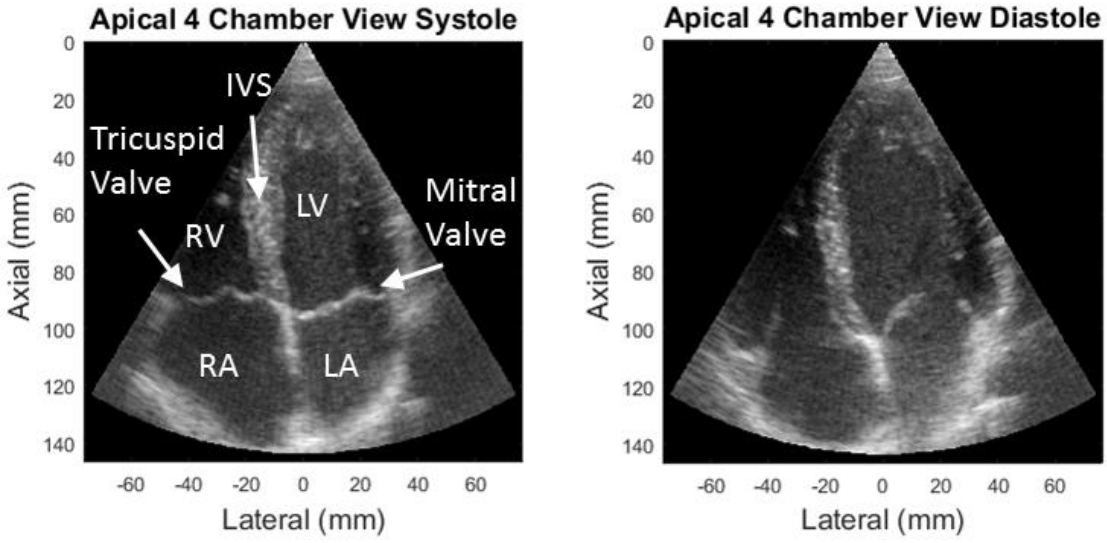

Figure 2.3 Apical 4 chamber view of the heart in (left) systole and (right) diastole. In this view the 4 chambers are visible as well as the mitral and tricuspid valves separating the atria from the ventricles. In systole, the ventricles are contracted and the ventricular chamber is small, the atria are filling up with blood. In diastole, the ventricular chambers are growing larger and filling with blood flowing from the atria.

diastole. Part of this downward elongation is discussed in Chapter 4 to form an ultrasound-based elastography method.

2.3.2. Cardiac Electrophysiology

Luigi Galvani discovered, in 1790, that by applying an electrical stimulus to an isolated muscle the muscle would contract as if it were alive (Piccolino 1997). Decades later, in 1844, Carlo Matteucci performed experiments where an isolated muscle was made to contract by placing it upon a beating heart. No outside electrical stimulus was applied. This brought about the discovery that the heart must produce its own electricity, and the beating of the heart was the result of its own spontaneous and semiperiodic generation of electricity. The first human recording of cardiac electrical activity, and electrocardiogram (ECG), was performed by Augustus Waller in 1887 (Waller 1887). Today, an ECG is performed by placing multiple electrodes on the surface of the body surrounding the heart and then calculating differences in the voltages recorded between the electrodes (Dubin 1996). Throughout this dissertation, all ECGs used in experiments were taken using a three electrode setup. The difference between two electrodes was calculated while the third was used as a ground reference. In this way, the electrical activity on the axis connecting the two differencing electrodes is visualized. Specifically, the propagation of electrical activity through the heart is visualized and deflections seen in an ECG are identified as waves. An example of an ECG recording is seen in Figure 2.4. Five features of the ECG signal are typically

identified (P, Q, R, S, T) and termed “waves.” These waves are related; each is primarily due to the propagation of a single electrical “event” which propagates throughout the heart and induces cardiac muscle contraction.

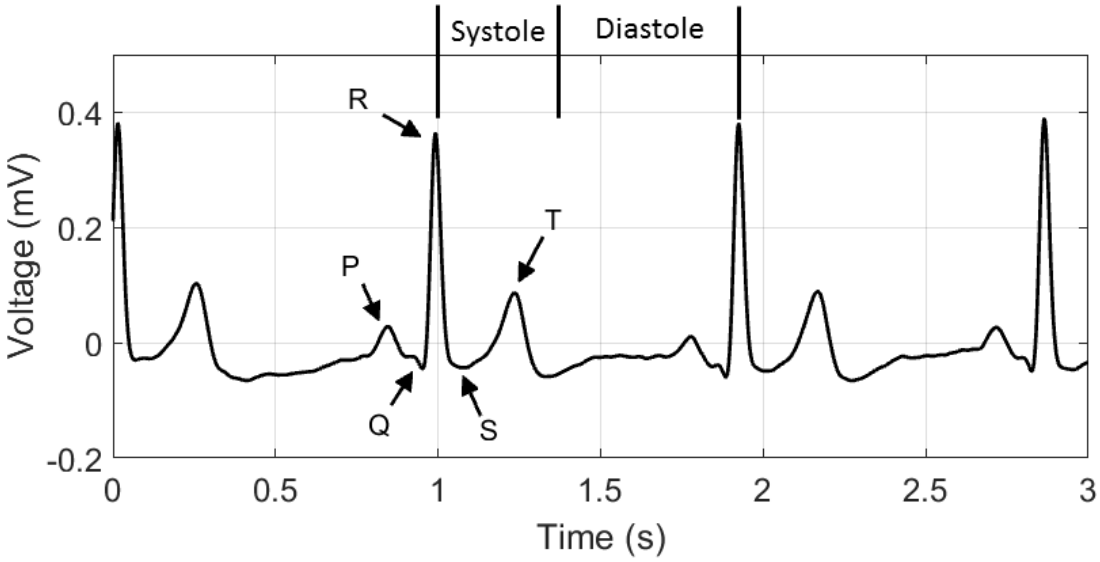

Figure 2.4 An ECG recording where the P,Q,R,S, and T waves are identified. The QRS-complex marks the beginning of systole. Diastole generally begins after the onset of the T-wave. The P-wave is the start of the heart cycle, associated with atrial contraction, the Q,R, and S-waves are associated with ventricular contraction. The T-wave is associated with the “resetting” of the ability of the ventricles to contract.

The heart cycle, referring to the series of both electrical and mechanical events that includes systole and diastole, begins with the spontaneous and semiperiodic electrical activation of the sinoatrial (SA) node, where the SA node is located on the surface of the RA. Following its activation, the electrical activity propagates across the atria causing the myocardium of the atria to contract and is associated with the P-wave of the ECG. This contraction of the atria, or the atrial “kick”, is a final push to fill the ventricles with blood near the end of diastole. Prior

to the atrial kick, ventricular filling is a passive event due to differences in pressure between the atria and the ventricles.

The Q, R, and S-waves together are known as the QRS-complex and are associated with the rapid propagation of electrical energy spreading across the bulk of the ventricular myocardium causing ventricular contraction and the systolic phase to commence. From the P-wave to the QRS-complex, the electrical energy initially propagating across the atria makes its way to the ventricles through the atrio-ventricular (AV) node. The advancing electrical wave is unable to directly move from the atria to the ventricles through the myocardium because the myocardium of the upper and lower chambers are electrically isolated. The AV node is the only path for electrical propagation and the speed of conduction is slow when compared to the conduction speed of the myocardium. This insulation, and the slow conduction speed of the AV node, results in the pause between the end of the P-wave and the beginning of the QRS-complex. The pause between the contraction of the atria and the ventricles is beneficial to cardiac function as it allows time for the ventricles to fill with blood during the atrial kick.

The QRS-complex is the most dominant signal in the ECG and thus is often used to trigger data acquisition for separate imaging techniques such as MRI and ultrasound for their synchronization with the heart cycle. In this way, the pattern of the ECG can be used to identify cardiac events throughout the heart cycle for different imaging modalities. In Chapter 4, the movement of the IVS which is caused the contraction of the atria during the atrial kick is studied.

2.4. Heart failure and what can go wrong

As the main job of the heart is to supply oxygenated blood and nutrients to the body, when the heart fails to do this, it is termed heart failure. The incidence of heart failure is increasing (Velagaleti et al. 2008). It is listed as a cause of death in 11% of deaths in the United States (Mozaffarian et al. 2015), and the cost of treatment was estimated at $30 billion for the year 2012 (Heidenreich et al. 2013). Heart failure itself is a subset of cardiovascular disease (CVD), which is the leading cause of death in America since 1919, and listed as a cause of death on 54% of all deaths in the United States for 2014 (Benjamin et al. 2017). Heart Failure is defined by the American College of Cardiology (ACC) and American Heart Association (AHA) as "a complex clinical syndrome that results from any structural or functional impairment of ventricular filling or ejection of blood (Yancy et al. 2013)." Given this, heart failure can arise from many different diseases or conditions and may originate elsewhere in the body. It may affect one or both sides of the heart and impair not only the contractile function, but the relaxing function as well (Jessup and Brozena 2003).

Diagnosis and determination of the underlying cause is difficult in patients with heart failure as the symptoms often overlap with symptoms of other diseases (McMurray et al. 2012). The first symptom of heart failure is often shortness of breath as the systemic organs suffer from inadequate blood perfusion and the body becomes starved of oxygen. Patients may also feel weak or fatigued and the symptoms are often mild and may first appear during exercise or when the heart is

stressed is some way (New York Heart Association. Criteria Committee and New York Heart Association 1994).

2.4.1. Diastolic Heart Failure and Diastolic Dysfunction

DHF refers to heart failure that has been caused by an abnormal function during the diastolic phase of the heart cycle—without a corresponding loss of function during the systolic phase. Over half of all patients with heart failure have DHF, and the percentage of patients diagnosed with DHF has increased from ~30% in 1987 to greater than 50% in 2001 (Gaasch and Zile 2004; Owan and Hodge 2006; Paulus et al. 2007).

Diastolic dysfunction (DD), one of the requirements for diagnosis of DHF, refers to the inability to of the heart to relax and fill properly (Zile and Brutsaert 2002). Causes for DD leading to DHF are varied. Because of the heart's central location in the cardiovascular system—which then affects nearly all tissues in the body—conditions affecting regions both distal and proximal to the heart can lead to adverse cardiac conditions. These conditions include, but are not limited to, arterial hypertension (Diamond and Phillips 2005), valvular heart disease (Mandinov et al. 2000), restrictive and hypertrophic cardiomyopathy (Asher and Klein 2002; Maron 2002; Maron et al. 2014), myocardial ischemia (Bonow et al. 1981), myocardial infarction (Thune and Solomon 2006), diabetes (Poirier et al. 2001), and kidney diseases (Parfrey et al. 1996). Because of the high number of diseases that can lead to DD, it is common, and found in about 10-35% of the

general population with prevalence increasing to greater than 50% of the population over the age of 75 (Abhayaratna et al. 2006; Kuznetsova et al. 2009; Redfield et al. 2003).

2.4.2. Cardiac Remodeling in the Presence of Disease

DD is often the result of the response and adaptation of the heart in the presence of disease. The heart continuously adapts itself due to changing physiological conditions (Cohn et al. 2000). The most well-known example of this adaptation is the Frank-Starling mechanism (Frank 1959; Starling 1918), which simply states that in order to maintain cardiac output, the amount of blood supplied to the body, the heart contracts more forcefully as more blood enters the ventricular chambers. This mechanism does not physically change the structure of the heart but rather its function. Changes in the structure of the heart, cardiac remodeling, can occur due to chronic or acute changes in physiological conditions. In some cases this remodeling is beneficial for cardiac function and can occur with no adverse health effects, such as the physiologic enlargement of the heart of a trained athlete (Scharhag et al. 2002). In other cases, the remodeling of the heart is pathologic and results in adverse health effects and can lead to DHF.

As an example of the progression of a disease leading to pathologic cardiac remodeling and DHF, the rest of this section will explore the response of the heart when the systemic circulation is under chronic high blood pressure (hypertension). This systemic hypertension may be the result of an underlying

disease; however, because many diseases can result in systemic hypertension a specific underlying disease is unimportant for this example. When the systemic circulation is under hypertension, the LV has to work harder to pump blood to the body. The Frank-Starling mechanism ensures that the same blood volume is delivered to the body regardless of blood pressure (Sonnenblick and Downing 1963); however, the LV chamber is not isolated from the increased pressure and is itself under hypertension (Elzinga and Westerhof 1973).

The heart begins to remodel itself as a form of protection against the increased blood pressures within the LV chamber and the increased stress upon the chamber wall (Sasayama et al. 1974). The form of this remodeling can be described with the Law of Laplace for the heart, which is written as:

$$\tau = \frac{PR}{2h} \tag{2.1}$$

where τ is the circumferential wall stress, P is internal chamber pressure, R is the chamber radius, and h is thickness of the chamber wall. An increased chamber pressure increases wall stress and the only way for the heart to reduce this stress is to undergo concentric hypertrophy, a thickening of the chamber wall (Grossman et al. 1975). The normal remodeling of the heart under concentric hypertrophy is to modify the myocardial extracellular matrix (ECM) to increase the amount of cardiomyocytes (cardiac muscle cells) within the wall. The wall becomes thicker by stacking the new cardiomyocytes up with the existing cardiomyocytes in parallel

layers (Bernardo et al. 2010). The ECM, which acts as scaffolding to guide the layering and growth of the cardiomyocytes, is composed of a collagen fiber network. The collagen fibers are mechanically stiffer than the cardiomyocytes which grow around them. The collagen fibers of the ECM normally synthesize and degrade over time (Berk et al. 2007), which results in normal hypertrophy with no loss of cardiac function. However, under pathological conditions, the synthesis and degradation of the collagen fiber network may become altered and begin to accumulate and undergo random crosslinking. This degrades the integrity of the ECM and leads to myocardial fibrosis and an increased stiffness of the myocardium (Weber 1989). With increasing myocardial stiffness, less blood enters into the ventricular chamber and DD becomes present. The heart must further adapt to maintain adequate blood supply to the body. If it cannot, then the outward signs and symptoms of DHF, such as shortness of breath, become more evident (Zile et al. 2004; Zile et al. 2015).

The preceding example was of the remodeling of the heart under chronic systemic hypertension; however, this is not the sole cause of DHF, rather it is only one of the diseases which can lead to an increased myocardial stiffness and eventually DHF.

2.4.3. The Need for Elastography

A full range of both structural and functional measurements of the heart are needed to diagnose DHF (Nagueh et al. 2016; Paulus et al. 2007). As evidence of

DD is needed for the diagnosis, and an increased myocardial stiffness leads to DD, the measurement of myocardial stiffness is essential in the diagnosis and management of patients with DHF. Current methods to measure myocardial stiffness include cardiac catheterization, where the patient may be placed under general anesthesia and will experience ionizing radiation of X-ray based fluoroscopy. Currently, there are no standard noninvasive clinical measures of myocardial stiffness which can be used to assess the progression of DD and the cause of symptoms of those with DHF. More objective and noninvasive measures are needed to reduce false positives and detect its early stages (Mosterd et al. 1997). Ultrasound elastography has the potential to provide an objective measure of myocardial stiffness. To better understand this, ultrasound is first introduced followed by a discussion of some current methods used in ultrasound elastography.

2.5. Principles of Medical Ultrasound

Figure 2.5 Typical ultrasound transducer used in medical imaging. The light gray band on the face of the transducer houses the components which transduce electrical energy into mechanical energy, and vice versa, to emit ultrasound into the body and record ultrasound echoes returning to the transducer.

Medical ultrasound is an imaging modality which uses high frequency sound waves, typically 1- 30 MHz, to visualize structures within the body. An ultrasound imaging procedure to acquire these images is performed by placing an ultrasound transducer on the surface of the body where the transducer acts as both the transmitter and the receiver to send ultrasound into the body and then record the resulting echoes. A gel is typically placed in between the transducer and the body to act as a coupling agent to improve the transfer of acoustic energy from the transducer face to the body. Figure 2.5 shows an example of a transducer used in

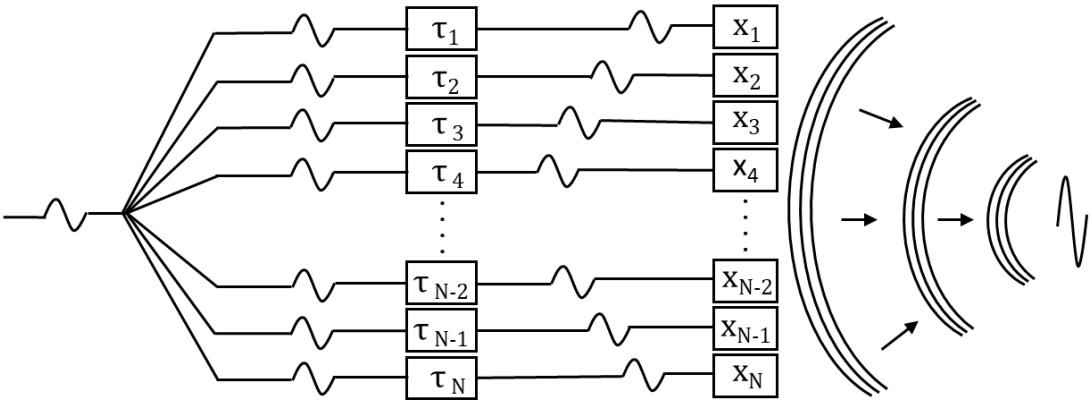

Figure 2.6 Transmit structure for an N element array where x_n signifies the transducer elements. Here the signal travels from left to right. A single pulse is applied and split into each channel where a time delay τ is applied before emitting the ultrasound into the tissue. This is a onetime focusing event.

medical imaging. This type of transducer consists of multiple elements in an array rather than a single transducing element. Because single elements in the array can be excited individually and at different times, the array structure allows for the electronic manipulation of the acoustic transmit profile and provides a means to focus and steer the ultrasound beam. In this way, a high-resolution image can be formed over a large region of space. Figure 2.6 shows the setup for transmitting and focusing sound into one region in space. Here, one signal is split onto multiple channels and time delays are applied to steer the beam. The time delays for each channel are calculated based on **1)** the distance between the desired point in space and the transducer element and **2)** an assumed or average speed of sound in the body of 1540 m/s. Figure 2.6 shows delays applied to focus sound in the imaging plane. These delays may also be applied in such a way as to transmit unfocused

sound into the body. This is often performed in ultrasound elastography in order to increase the imaging frame rate as a single unfocused transmit can cover the entire imaging region. These unfocused transmit methods will be discussed later.

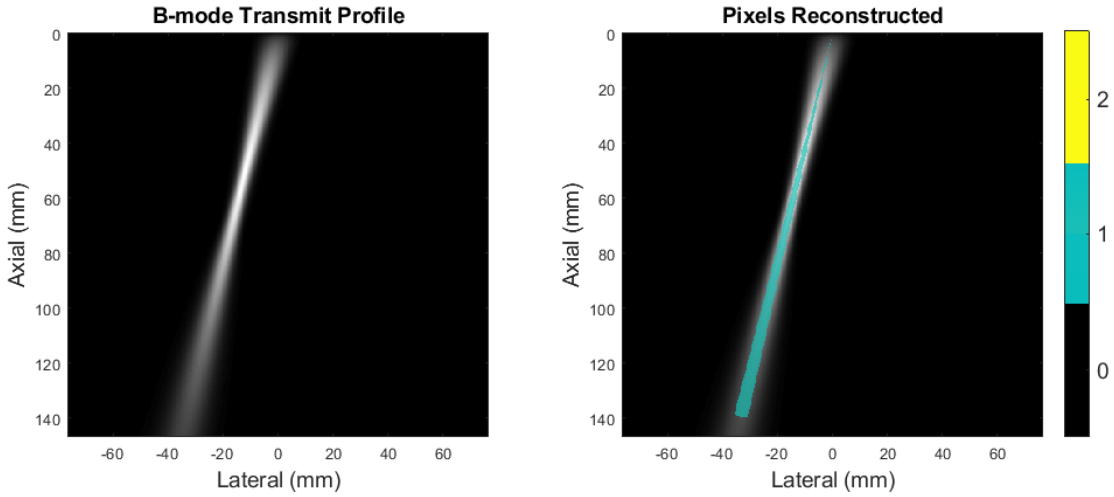

Figure 2.7 B-mode ultrasound transmit profile where the transmit is focused at a depth of 70 mm. An image is formed incrementally by using multiple transmits and sweeping each transmit laterally across the imaging frame. The colorbar shown the number of contributions for a single transmit/receive reconstruction.

Figure 2.7 on the left shows the transmit profile for a conventional focused ultrasound data acquisition event. The brightness of this figure represents the acoustic energy for a single ultrasound transmit. Using the structure shown in Figure 2.6 the beam is focused at a depth of 70 mm and steered laterally. On the right of Figure 2.7 a green band is overlaid on top of the grey scale image of the transmit intensity. This green band signifies the region of pixels to be reconstructed for this particular transmit/receive event. Pixels are only reconstructed in the center region where the acoustic transmit intensity is the greatest. Data acquisition for a complete imaging frame is performed by sweeping

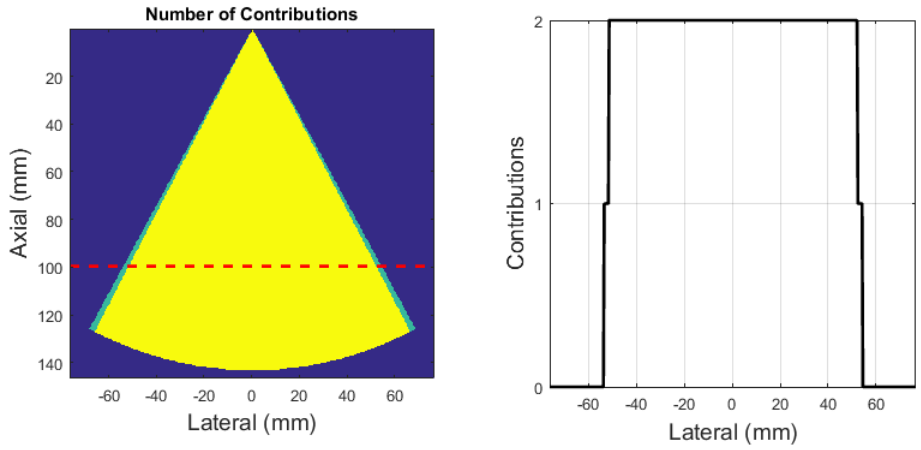

Figure 2.8 (left) Number of coherent compounding for each pixel in the B-mode image reconstruction. The central region shows 2 contributions per pixel and the borders only 1. Each contribution is a reconstruction from different angled ultrasound transmits. (right) The number of contributions for a depth of 100 mm. Data taken from the red dashed line on the left.

the transmit/receive events laterally and reconstructing pixels in the region of greatest ultrasound transmit acoustic energy. Because the acoustic energy is spread out for each transmit, there is an overlap of energy from one transmit to the next and pixels reconstructed in one transmit/receive event overlap with pixels reconstructed from spatially adjacent transmit/receive events. This overlap allows for the averaging of the reconstructions from spatially adjacent transmit/receive events and helps to improve the image signal-to-noise ratio (SNR) in the image. This improvement is achieved because the underlying structure being imaged remains the same while the acoustic noise is random and incoherent; thus, during summation the signal from the structure is summed coherently while the noise is summed incoherently and therefore reduced. Figure 2.8 on the left shows the

number of reconstructions for each pixel in one imaging frame. A slice is taken at a depth of 100 mm and the number of contributions at this depth is shown on the right. For this data acquisition sequence two contributions are made per pixel for most of the imaging frame.

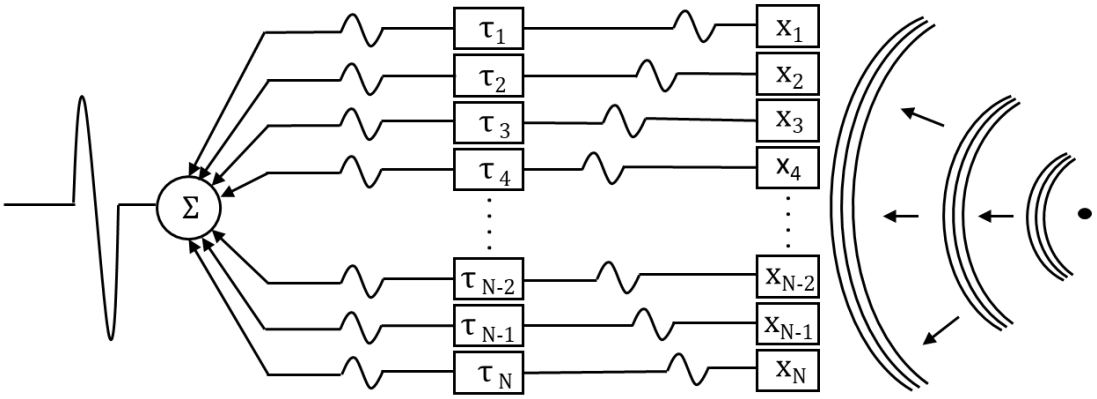

Figure 2.9 A delay and sum beamformer. Here the signals travel from right to left. Acoustic reflections returning to the transducer are first time aligned and then summed to form a final acoustic signal originating from a point in space. τ_n is the time delay applied to the n^{th} channel. On receive, this can be performed for every point in the imaging space to reconstruct an image.

As previously stated, reconstruction for an imaging frame is performed on a pixel by pixel basis based on the recorded echoes from the corresponding transmit event (Daigle 2009). Figure 2.9 shows the setup for a delay-and-sum beamformer which performs the image reconstruction. It is similar to the structure used for focusing on transmit; however, the time delays for receive beamforming can be applied to focus on every point in the imaging space. After the delay is applied, each signal is aligned in time and can be summed together.

To further show the necessity of the delay and sum beamformer Figure 2.10 shows the radio frequency (RF)-data echoes recorded from an ultrasound transmit on a 64-element transducer. This RF-data recording was taken while focusing the acoustic transmit beam laterally through the imaging plane. It can be seen that the signals on different transducer elements are not aligned in time, and the first few samples show how the initial acoustic reflection becomes more and more delayed as the element number increases. The delays between elements are reduced as the sample number increases for echoes returning from far away from the transducer. For these echoes the wave front incident on the transducer becomes flat. This can be seen from the high amplitude reflection starting around sample number 2500 where the required delays are less obvious. Figure 2.11 shows a close-up of the ultrasound data recorded from a single element. From here the carrier frequency is seen as the constant oscillation. This oscillation is not used for direct imaging; rather, it is the amplitude of the wave which carries the information which is used for visualizing the tissue structure.

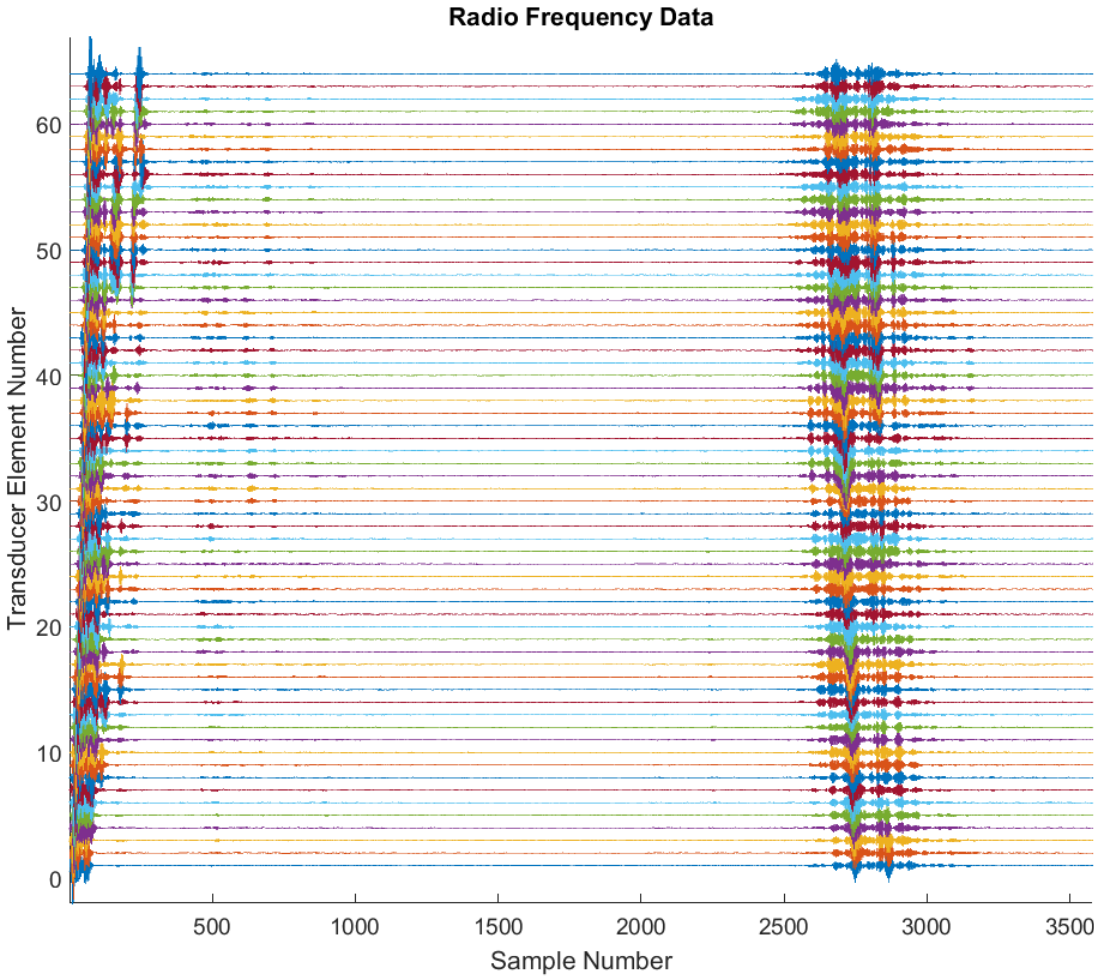

Figure 2.10 Ultrasound data recorded from a single transmit into the body. Here, the transducer has 64 elements. The data is aligned and summed to reconstruct the signal coming from a specific region in the imaging field.

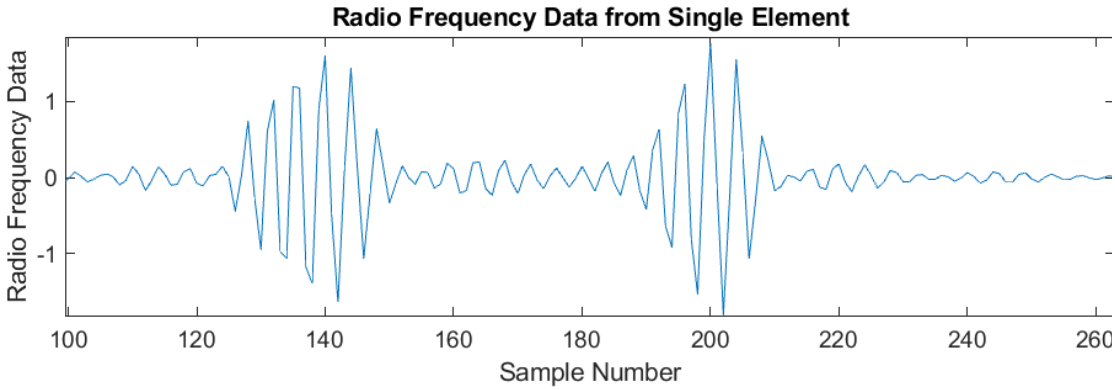

Figure 2.11 Close-up of the ultrasound data recorded on a single element from a single transmit into the body.

2.5.1. B-Mode Imaging

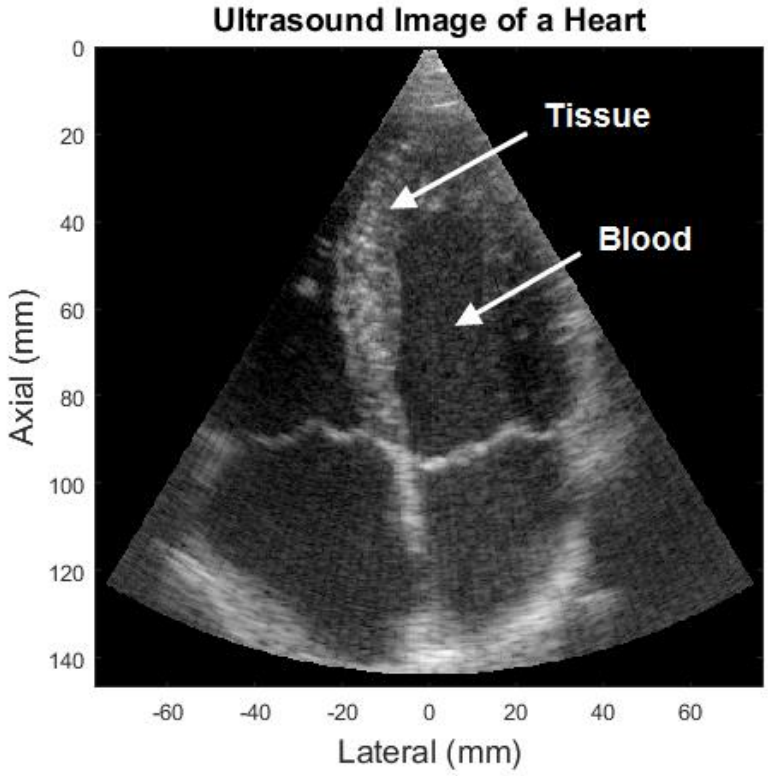

Figure 2.12 Copy of Figure 1.1. B-mode ultrasound image of the heart where the brightness corresponds to higher acoustic reflections.

As previously mentioned, a common method in ultrasound imaging is to present the sonographer with an image representing the underlying structure of the tissue. An example of this is shown in Figure 2.12 where a heart is visualized in a grey scale image. This type of image is termed a B-mode image. What is essentially being imaged is the amplitude of the acoustic reflections, where brighter regions in the image are associated with higher amplitude acoustic reflections. This image was acquired in the same steps as previously described. Ultrasound is transmitted and focused into the imaging region, the RF-data is

recorded, passed through a delay-and-sum beamformer and reconstructed for every pixel. However, what is reconstructed is not the real component of the RF-data but rather the RF-data represented as a complex data set. To acquire the complex data set the real component of the RF-data is recorded and converted into an In-phase and Quadrature (IQ) complex data form using a Hilbert transform. The B-mode image is formed by taking the amplitude of the reconstructed IQ-data image and log compressing the result for display to the user.

2.6. Methods in Ultrasound Elastography

A simple way to translate ultrasound imaging to elastography—imaging the *in vivo* stiffness of tissues—is shown in Figure 2.13. This imaging procedure can be done by **1)** placing the transducer on the surface of the body and collecting an initial B-mode image, and then **2)** apply a slight force to the transducer, pushing it into the body causing tissue displacement, and then collecting a second B-mode image. Following this, a strain image may be estimated by calculating the deformation of the ultrasound speckle pattern between the two collected images (O'Donnell et al. 1994; Ophir et al. 1991). From there, Young's modulus may be calculated if the stress field acting upon the tissue is homogeneous; however, this is rarely the case in diagnostic imaging where most tissues are heterogeneous. Thus, strain imaging, while able to provide a useful qualitative image of tissue deformation, still suffers from the same problems associated with manual

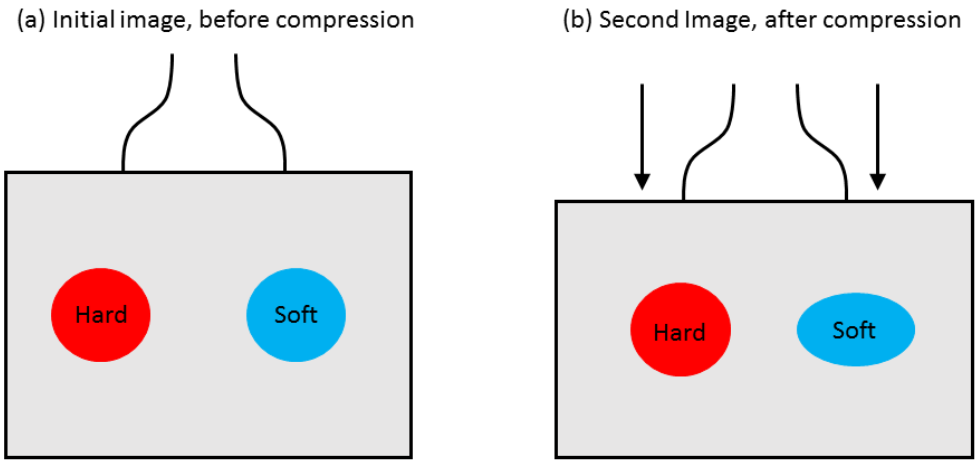

Figure 2.13 Example of strain imaging setup. (a) An initial reference image is acquired prior to any tissue compression, and (b) the tissue is compressed and a second image is acquired. The degree of displacement is then calculated and displayed. Softer tissues deform more than harder ones.

palpation. This problem is that further into the tissue, as the tissue becomes more heterogeneous, the stress field becomes complex, and non-uniform forces act upon the tissue causing deformation. The strain field represents the combination of the intrinsic stiffness of the tissue and the overall geometry (Greenleaf et al. 2003; Ophir et al. 2002). Thus, the question, "How hard is this?" can only be answered with a relative score of tissue stiffness. Young's modulus cannot be estimated accurately.

To overcome the issue with strain imaging, a technique termed Shear Wave Elastography (SWE) was introduced (Sarvazyan et al. 1998). SWE is a method which **1)** generates a shear wave in a tissue and **2)** tracks the speed of the wave as it moves through the tissue. The equation of motion describing wave propagation in a homogeneous, isotropic, infinite, and linear elastic media is written as:

$$(\lambda + 2\mu)\nabla(\nabla \cdot \mathrm{u}) - \mu\nabla \times \nabla \times u = \rho u_{tt}, \quad (2.2)$$

where λ is Lamé's 1st parameter, μ is the shear modulus, ρ is the density of the tissue (approximately 1000 kg/m^3 for soft tissues (Allen et al. 1959a; Allen et al. 1959b)), u is the displacement of the tissue, u_{tt} indicates the second temporal derivative of u, and ∇ is the del operator. Because shear waves are divergence free ($\nabla \cdot u = 0$), the first term on the left-hand side goes to zero and the shear wave equation of motion can be written as (Sandrin et al. 2002a):

$$\mu\nabla^2 u = \rho u_{\mathrm{tt}}. \quad (2.3)$$

By collecting the constants, the shear wave speed (SWS, c_s) is then proportional to the shear modulus by (Nichols et al. 2011):

$$\mu = \rho c_s^2. \quad (2.4)$$

The shear modulus represents the ability of the tissue to resist shear stresses. This may be visualized as one material sliding on top of another causing deformation, where the forces causing deformation are parallel to the surface. This is contrasted to Young's modulus where the force is perpendicular to the surface and causes either compression or tension. The relationship between Young's modulus and Shear modulus is written as:

$$\mu = \frac{E}{2(1+\nu)} \tag{2.5}$$

where ν is Poisson's ratio. Poisson's ratio is a measure of lateral strain to axial strain and is limited to a range of $0 < \nu < 0.5$. For incompressible materials $\nu = 0.5$. This means that a 1 unit axial strain results in a 0.5 unit lateral strain on both sides of the tissue being compressed. Because biological soft tissues are composed of mostly incompressible water, Poisson's ratio is approximately 0.5 and from Eq. (2.5):

$$\mu = \frac{E}{3}. \tag{2.6}$$

Thus, from Eq. (2.4) and (2.6) the intrinsic stiffness of tissues, the shear modulus and Young's modulus, are proportional to the square of the SWS. This forms the basis of SWE, and the estimation of the SWS is critical to the accurate and objective assessment of the stiffness of tissues.

2.6.1. Shear Wave Generation

There are several methods for SWE. These can be classified by how the shear wave is generated. The first method implemented was by simply shaking the surface of the tissue (Muthupillai and Ehman 1996; Sandrin et al. 1999). In this method, a mechanical actuator vibrates the tissue at a low frequency, typically 50-400Hz, and a low amplitude shear wave propagates through the tissue. This is a

technique which allowed multiple research teams to investigate various tissues using ultrasound (Nenadic et al. 2011; Sandrin et al. 2002b; Zhao et al. 2014) and MRI imaging systems (Manduca et al. 2001; Wassenaar et al. 2016). However, the ultrasound transducer and imaging setup must be significantly modified to perform imaging, and shear waves may have difficulty penetrating deeper or more complicated tissue structures such as the heart.

Another method for SWE includes Acoustic Radiation Force (ARF) based SWE (Nightingale et al. 2003; Sarvazyan et al. 1998). The acoustic radiation force is the force associated with sound propagation. As sound propagates, it pushes constantly on the tissue causing displacement. Thus, in ARF based SWE, an acoustic push first displaces the tissue, then if the tissue has an elastic component and can hold a shear stress, a shear wave is generated which propagates outward and away from the initial push location. The shear wave in this method can be localized to specific areas allowing for the selective investigation of tissues; however, the amount of a significant push in the heart is challenging due to acoustic attenuation and transducer heating. Figure 2.14 shows the example setup for both the mechanically induced and ARF induced shear waves in SWE.

These two methods have a source of shear wave generation external to the body, which have challenges generating shear waves within the heart. Other methods have a source of generation internal to the body and are usually associated with the heart cycle (Kanai 2005; Konofagou et al. 2011; Pislaru et al. 2014; Vos et al. 2017). Because of the challenges associated with externally

generating a shear wave in the heart, a method has been developed that will be described in Chapter 4 for cardiac SWE where the source of wave generation is within the heart—the contraction of the atrial myocardium during the atrial kick.

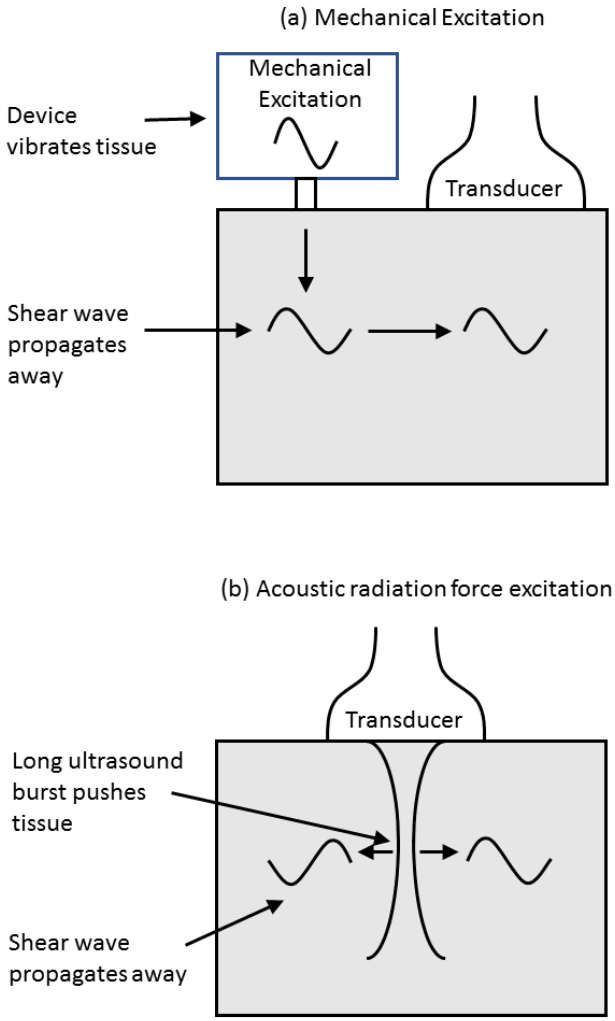

Figure 2.14 SWE based on the generation of shear waves from (a) the mechanical excitation at the surface of the tissue, and (b) from the ARF of an extended burst of ultrasound.

2.6.2. Shear Wave Visualization

Regardless of the method chosen for shear wave generation, shear wave detection and tracking is necessary for all methods. In this dissertation shear wave visualization is accomplished by a phased based tissue velocity measurement which was first developed to image blood flow but is also used to image tissue movement. The change in phase is calculated from the recorded IQ echo data from consecutive ultrasound transmits. Because the ultrasound wavelength is directly related to the frequency of the transmitted ultrasound pulse and the speed of sound in water, a distance is calculated from the change in phase of the recorded IQ data. Further, because the time difference between ultrasound pulses is known the phase shift estimation is analogous to a velocity estimator. This is represented by the 1-lag autocorrelation based method and is written as (Kasai et al. 1985; Loupas et al. 1995):

$$v = \frac{c}{2}\,\frac{PRF\,\tan^{-1}\left(\frac{\sum_{m=0}^{M-1}\sum_{n=0}^{N-2}[Q(m,n)I(m,n+1)-I(m,n)Q(m,n+1)]}{\sum_{m=0}^{M-1}\sum_{n=0}^{N-2}[I(m,n)I(m,n+1)+Q(m,n)Q(m,n+1)]}\right)}{2\pi f_{rcv}}, \quad (2.7)$$

where v is the axial tissue velocity, the velocity towards and away from the transducer, c is the speed of sound in the body which is approximately 1540 m/s. The Pulse Repetition Frequency (PRF) is the frequency of ultrasound image acquisition, and f_{rcv} is the frequency of the recorded echoes.

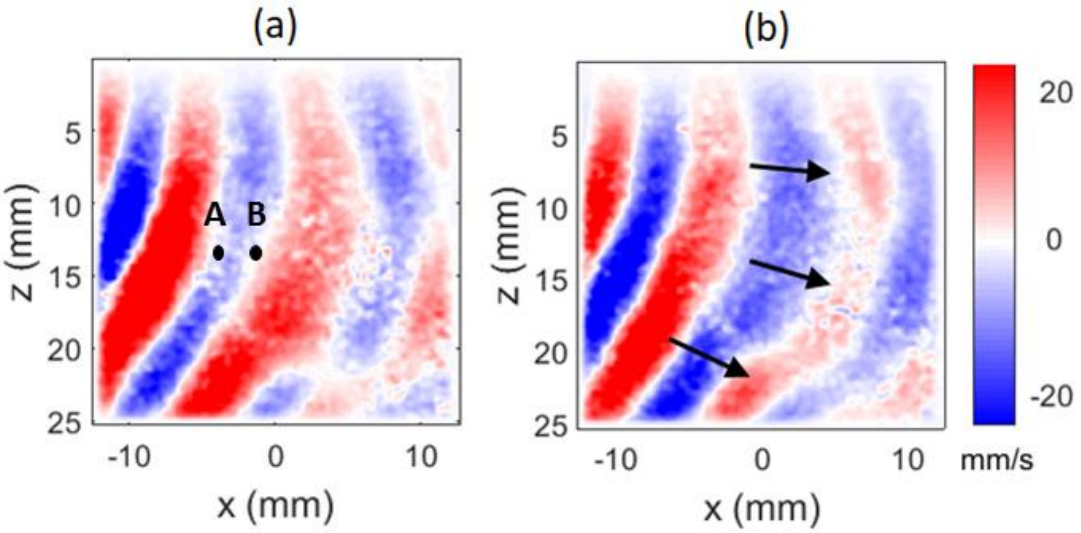

Figure 2.15 Tissue velocity from the whole data imaging frame. Visualization is at two different times. (a) 10 ms and (b) 20 ms after the start of data collection. Red indicates tissue particle movement toward the transducer while blue indicates particle movement away from the transducer. The transducer is oriented at the top of the image and looking down. From (a) to (b) the waves propagate left to right with the black arrows indicate the movement. Two points are chosen in (a) as A and B and tissue velocity at these points for all time are shown in Figure 2.16.

Tissue velocity should not be confused with the SWS; rather, it is the imaging of tissue velocity which allows for the visualization of the shear wave movement and for the subsequent estimation of SWS. A shear wave is typically defined as wave motion where the individual particle motion is perpendicular to the direction of wave propagation. Thus, for a wave traveling laterally (left to right in Figure 2.15) through an imaging region the particle motion (i.e. its tissue velocity) is oscillatory towards and away from the transducer (up and down in Figure 2.15). Because tissue velocity estimators measure movement towards and away from the transducer they are a potential candidate for visualization of shear

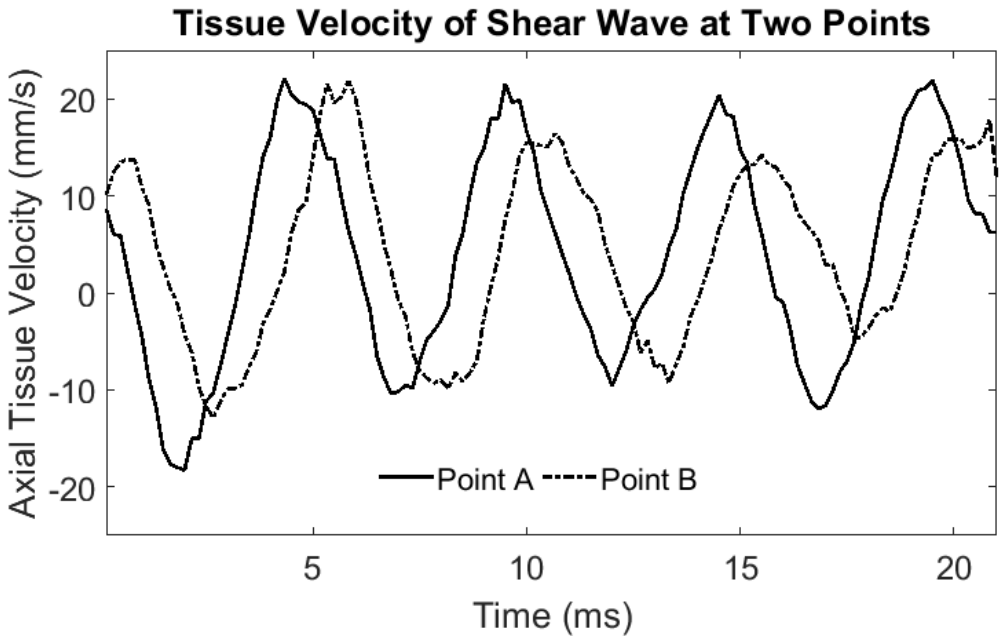

Figure 2.16 Shear wave tissue velocity from the two points labeled in Figure 2.15 (a). The points are separated by about 2 mm and it takes about 1 ms for the wave to propagate from point A to Point B.

wave motion. An example of a shear wave is shown in Figure 2.15. The reconstructed tissue velocity of the wave for two whole data frames is shown for two different times. The wave is seen advancing from left to right. Two points separated by a distance of about 2 mm are labeled in this figure, A and B. Figure 2.16 shows the tissue velocity reconstructed at these two points in the imaging frame for an entire data collection sequence. From here it can be seen that the oscillatory motion of the tissue at point B is delayed compared to the motion at point A. From the data shown in Figure 2.15 and Figure 2.16 the SWS can be detected and quantified and the mechanical properties of tissues can be characterized with a high dynamic range (Sarvazyan et al. 2013).

2.6.3. SWS Estimation

As previously shown in Eq. (2.3), the equation of motion for shear wave propagation in an isotropic, homogeneous, incompressible media can be written as:

$$u_{tt} = c_s^2 \nabla^2 u \tag{2.8}$$

where u is the 3-D shear wave spatiotemporal signal, u_{tt} is the second temporal partial derivative of u, and $\nabla^2 u$ is the Laplacian of u. For a purely elastic media the shear modulus μ is related through the material density ρ by (Sarvazyan et al. 2013):

$$\mu = \rho \left(\frac{f_{mech}}{f_{sp}} \right)^2 = \rho c_s^2, \tag{2.8}$$

where f_{mech} is the frequency of mechanical excitation, f_{sp} is the local spatial frequency, and c_s is the SWS.

Many approaches have been taken for robust estimation of SWS. Imaging of the SWS can be performed by estimating the local spatial frequency from a propagating shear wave. f_{sp} has been estimated over multiple scales using local spatial frequency estimators and provided a robust estimation of shear elasticity from a single imaging frame; however, resolution was dependent on shear wavelength and visualization of sharp boundaries was limited (Manduca et al. 2001). Phase based estimations selectively filter for the shear wave frequency f_{mech},

where the phase gradient of the resulting shear wave signal provides f_{sp}. This technique assumes propagation of a plane wave and has been implemented successfully in transient elastography (Catheline et al. 1999).

Inversion of Eq. (2.8), the second-order wave equation, was implemented and required second order spatial derivatives and several imaging frames for second order temporal derivatives (Bercoff et al. 2004). By assuming independence of temporal and spatial variables, a method for inversion of the Helmholtz equation was implemented which only relied on second-order spatial derivatives. This method was able to recover SWS from a single imaging frame (Oliphant et al. 2001). Because the SWS is estimated from the equation of motion for waves in the media, these methods assume only waves are present in the tissue. Both approaches relied on second-order derivatives which were difficult to estimate because of inherently low SNR in the data. To overcome this limitation, time-of-flight (TOF) based approaches to SWS estimation were introduced (McLaughlin and Renzi 2006; Palmeri et al. 2008; Tanter et al. 2008). These approaches can be broken up into various forms of cross-correlation (CC), and time-to-peak (TTP) methods. For an example using the signals in Figure 2.16, the SWS can be estimated using the following:

$$c_s = \frac{\Delta d}{\Delta t}, \tag{2.9}$$

were Δd is the distance between points used to produce the signals, and Δt is the lag between the two signals. The CC method estimates Δt by performing a CC of the signals and locating the maximum of the CC result. A 2-D approach for CC based TOF methods was developed and implemented to estimate SWS from any direction of wave propagation (Song et al. 2014a; Zhao et al. 2014). These approaches perform multiple cross-correlations along the direction of wave propagation to provide a moving average estimate for SWS. The TTP method tracks the arrival time of the maximum value of the shear wave signal and then performs a first-order spatial differentiation to estimate the SWS. TTP methods are often chosen because of the attenuation of the shear wave as it propagates through a tissue (Palmeri et al. 2008). The assumption for this method is that the maximum value does not change locations in the signal as the wave propagates; thus, tracking its location tracks the shear wave. The tracking of other locations in the shear wave signal have also been implemented which track zero-crossings, or 25%, and 50% of the leading edge of the signal (Apostolakis et al. 2016; Shahmirzadi et al. 2012; Strachinaru et al. 2017).

Chapter 3.

Validation of Shear Wave Elastography

3.1. Introduction

This chapter describes experiments intending to validate SWE and proposes a new method for 2-D SWS estimation. The theory leading to this method is described in section 3.1.1. The content of this chapter will demonstrate the feasibility of the new estimation method and compare and contrast the method to other current methods of 2-D SWS estimation.

3.1.1. Theory

In a 3-D medium, the wave field $\boldsymbol{u}$ can be written as the superposition of waves originating from some source and propagating along all possible paths (Snieder 1999):

$$u(t) = \sum_{P} \boldsymbol{S}(t; P), \tag{3.1}$$

where P is a unique path in the medium. $\boldsymbol{S}$ is an arbitrary waveform associated with a particular path P and may vary with time t due to geometric spreading, attenuation, or interactions at interfaces along the path. By grouping terms in Eq. (3.3) based on the direction each path takes through space, the wave field can be rewritten as:

$$\boldsymbol{u}(t) = \sum_{\theta} \boldsymbol{U}(t;\theta) \tag{3.2}$$

where **U** is an arbitrary time varying waveform propagating in the direction θ:

$$\boldsymbol{U}(t;\theta) = \sum_{S(P)\in\theta} \boldsymbol{S}(t;P). \tag{3.3}$$

By defining ξ as a new axis along the direction of wave propagation, the arbitrary waveform **U** can be defined as existing on the characteristic curve, $\xi - c_s t = 0$. Assuming the shape of **U** changes only due to attenuation and not through pathway interactions, Eq. (3.3) becomes:

$$\boldsymbol{U}(\xi,t) = \boldsymbol{U}_0(\xi - c_s t)e^{-\alpha t}, \quad c_s > 0, \;\; \alpha \geq 0 \tag{3.4}$$
$$\boldsymbol{U}_0(\xi) = \boldsymbol{U}(\xi,0).$$

By the method of characteristics, Eq. (3.5) is the solution to the 1-D first order wave equation:

$$\boldsymbol{U}_t + c_s \boldsymbol{U}_\xi = -\lambda \boldsymbol{U}, \qquad c_s > 0, \;\; \alpha \geq 0, \tag{3.5}$$

where $\boldsymbol{U}_t$ and $\boldsymbol{U}_\xi$ are the first derivatives of time and space respectively. The local inversion algorithm can be written as:

$$c_s = \left| \frac{\boldsymbol{U}_t + \alpha \boldsymbol{U}}{\boldsymbol{U}_\xi} \right|, \quad \alpha \geq 0, \tag{3.6}$$

where the absolute value forces a positive SWS. Because $\boldsymbol{U}_t = O(\omega \boldsymbol{U})$ and for weakly attenuating waves $\omega \gg \alpha$, the leading order approximation becomes:

$$c_s \sim \left| \frac{\boldsymbol{U}_t}{\boldsymbol{U}_\xi} \right|. \tag{3.7}$$

Thus, for this method it is required that $\boldsymbol{U}$ be continuous and differentiable.

3.1.2. Requirements and Experimental Validation

This new method assumes local propagation of plane waves and relies on first-order partial derivatives for a robust estimate of 2-D SWS. Directional filters are used to meet the assumption of local plane shear wave propagation. The method is validated by comparing the SWS estimated from the proposed method to **1)** conventional SWS estimation methods and **2)** a mechanical compression test. The SWS is estimated on three homogeneous phantoms of varying Young's modulus and one inclusion phantom representing heterogeneous tissue.

3.2. Methods

For validation, three homogeneous gelatin phantoms were made using 5%, 7%, and 9% gelatin by weight, and the one inclusion phantom was made which was composed of 5% gelatin as a background and 9% gelatin in the inclusion (See APPENDIX A for a description of the procedure). All phantoms contained 1% propanol by weight. A programmable research ultrasound system (Vantage 256, Verasonics Inc., Kirkland WA, USA) was configured to provide both the B-Mode image and the SWS map by the method proposed in section 3.1.1. A wideband, small parts linear array transducer with a center frequency of 10.0 MHz was used for imaging (L12-3v, Verasonics Inc., Kirkland WA, USA). Each phantom was imaged in five spatially different locations and the SWS were estimated using the method presented here.

3.2.1. Shear Wave Generation and Visualization

Shear waves were introduced by an external mechanical shaker (Type 4810, Brüel and Kjaer, Nærum, Denmark). A 20 cycle, 3 V amplitude, 200 Hz signal was produced by a function generator (Aglient 33250A, Agilent Technologies, Inc., Santa Clara, CA, USA). A power amplifier (Type 2716c, Brüel and Kjaer, Nærum, Denmark) with a gain of 18 dB was used to drive the shaker to introduce detectable shear waves in the phantoms. To induce shear waves into the media and limit the direction of wave propagation to the dominant path (directly from the shaker), a bar was used at the phantom-shaker interface (Gennisson et al. 2003). The

transducer was placed perpendicular to the long axis of the bar as shown in Figure 3.1.

Figure 3.1 Experimental setup for SWE on a gelatin phantom using an external mechanical vibration for shear wave generation. The setup consists of (a) the mechanical actuator, (b) the tissue mimicking phantom, and (c) the ultrasound transducer. Shear waves are generated by the up and down vibration of the mechanical actuator. The bar on touching the surface of the phantom ensures the shear waves will be quasiplanar as they propagate through the imaging plane of the transducer.

Immediately following cessation of the external mechanical excitation, a high frame rate plane wave imaging method was used to reduce the SNR on the image and provide the frame rate necessary for visualization of shear wave motion (Tanter et al. 2002; Tanter and Fink 2014). A PRF of 6000 Hz and pulse center frequency of 10 MHz was used for ultrasound SWE imaging. Images were captured at three transmit angles ($-4°, 0°, 4°$). Figure 3.2 shows the plane wave transmit profiles and the individual transducer element delay used in this study. Plane wave images were formed using a pixel based beam forming approach where dynamic receive beamforming is performed for each pixel in the reconstructed image

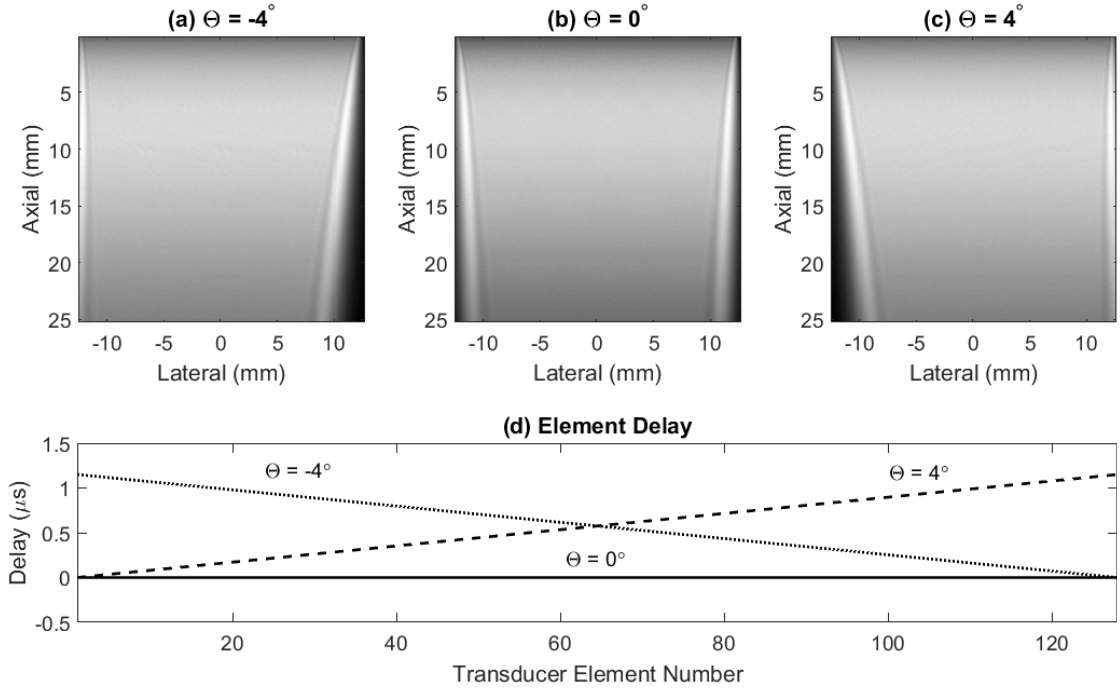

Figure 3.2 Ultrasound transmit profile for the SWE imaging sequence consisting of 3 differently angled plane wave images at (a) -4°, (b) 0°, and (c) 4°. (d) the individual element delays for each transmit.

(Daigle 2009). Axial and lateral spatial sampling for image reconstruction was 0.1 mm.

The final 3-D IQ data size was 256 × 256 spatial pixels and 129 frames in time. Shear waves were imaged following cessation of external mechanical vibration to ensure the entire imaging plane contained shear waves and could be used for SWS estimation. The total time for data collection was 121.5 ms, which included 100 ms used for mechanical excitation.

Assuming no discontinuity in the shear waves, the order of partial differentiation is interchangeable, and any partial derivative of a solution is also a solution. Because the wave field is independent between dimensions, each dimension provides a solution. Thus, the axial velocity component of the shear wave field is a solution to the wave equation for shear wave propagation and can be used in the inverse problem. The axial component of shear wave velocity was estimated using a two-sample 1-D autocorrelation method on the IQ data from consecutive frames of the plane wave images taken from the same angle (Kasai et al. 1985). To remove noise, a 3 × 3 pixel (0.3 mm × 0.3 mm) spatial median filter was used on each frame in the shear wave signal. A three-sample temporal moving average of the velocity was performed to improve the SNR. A final 5 × 5 pixel (0.5 mm × 0.5 mm) spatial average was applied to the velocity estimate. The shear wave imaging frame rate remained at 6000 Hz.

3.2.2. Directional and Temporal Filtering

Directional filtering was performed in the 3-D spatiotemporal frequency domain for selection of laterally moving waves. Filtering is described using cylindrical coordinates rather than rectangular coordinates. The radial, azimuthal and height components in the cylindrical coordinate system correspond to the absolute spatial frequency, the direction of wave propagation, and the temporal frequency components of the shear wave motion signal. For a robust 3-D Fourier transformation, every dimension of the spatiotemporal shear wave motion signal was Tukey windowed with a ratio of tapered-to-constant section of 0.1. As will be described in section 3.2.3, the SWS was not estimated from data frames affected by the windowing function; thus, a Tukey window was chosen as it better preserves the center of the data for SWS estimation (Harris 1978). Using an inverse 3-D Fourier Transform for each direction, the spatiotemporal-frequency shear wave signal was converted back to the spatiotemporal domain to provide the analytic shear wave signal.

Wideband directional filters similar to those used in (Deffieux et al. 2011; Manduca et al. 2003) were designed to separate two directions of shear wave propagation ($\theta = 0°, 180°$), where the dominant path of wave propagation was assumed to be in the lateral direction across the phantom. Figure 3.3 shows the combination of the spatial frequency and directional windowing filters as well as a zoomed in view of the temporally averaged spatial frequency Power Spectral

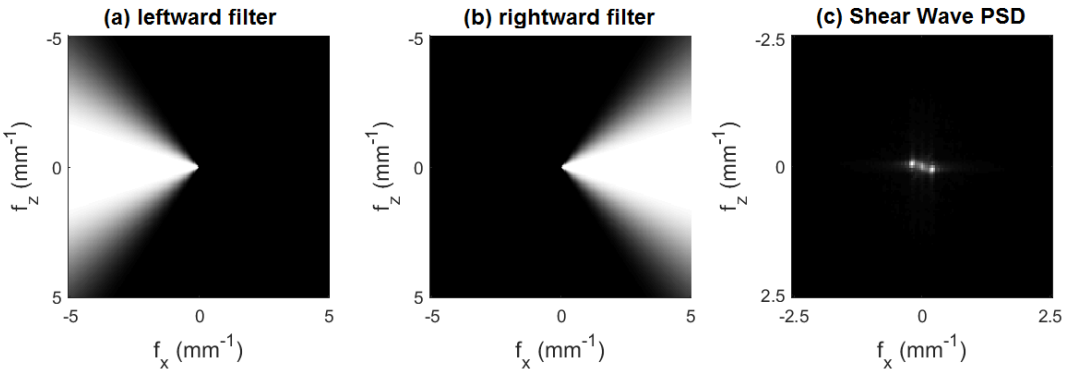

Figure 3.3 Directional filter separating out the (a) leftward and (b) rightward propagating shear waves. (c) a zoomed in PSD of a shear wave field.

Density (PSD). Because waves propagating in the elevational direction may correspond to higher speeds, a SWS higher than 5 m/s were filtered out. These were filtered using a fourth-order high-pass Butterworth filter with -3 dB cutoff frequency of 0.4 mm^{-1}. The windowing function for the directional filtering was a Tukey window with a tapered-to-constant ratio of 0.75 (Harris 1978), where the bounds of the Tukey window were at $\pm\pi/3$ about the desired direction.

Figure 3.4 shows the temporal frequency filter, which was a sixth-order band-pass Butterworth filter with -3 dB cutoff frequencies of 128 Hz and 1.38 kHz to selectively filter the 200 Hz excitation signal seen in the PSD. Negative frequencies were kept at zero and the positive frequencies were doubled to ensure no loss in signal power. In this way, the signal is both temporally filtered and Hilbert transformed in the frequency domain (Marple 1999).

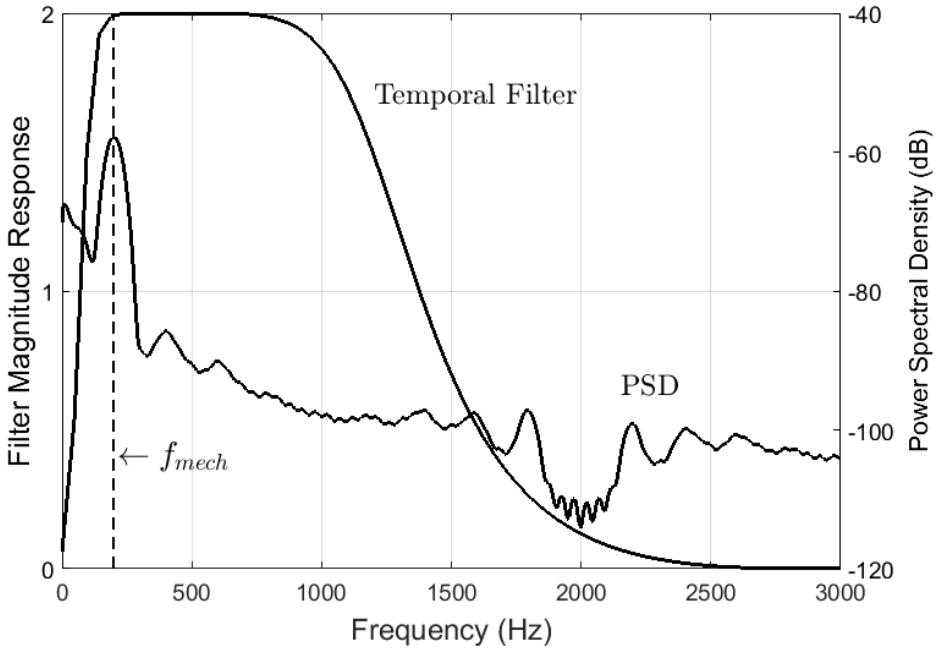

Figure 3.4 Temporal filter used to select for the shear wave mechanical excitation frequency of 200 Hz. The temporal filter is not symmetric as all negative frequencies are zeroed out. The magnitude response is 2 to account for the zeroing out of the negative frequencies.

3.2.3. SWS Estimation

Because the shear wave may propagate in the lateral and axial directions, it is necessary to estimate the 2-D SWS. Assuming the post-directionally filtered waves are unidirectional within the estimation kernel, the gradient magnitude points in the direction of wave propagation and therefore was used as an estimate for the spatial derivative, $\boldsymbol{U}_{\xi} = \sqrt{\boldsymbol{U}_x^2 + \boldsymbol{U}_z^2}$. The local shear wave inversion used was:

$$c_s = \left| \frac{\boldsymbol{U}_t}{\sqrt{\boldsymbol{U}_x^2 + \boldsymbol{U}_z^2}} \right|. \tag{3.8}$$

Robust numerical differentiation was performed by estimating $\boldsymbol{U}_x$ and $\boldsymbol{U}_z$ using 2-D Savitzy-Golay filters with a 4th order polynomial over a 45 × 45 pixel region, and $\boldsymbol{U}_t$ was estimated using a 1-D 4th order Savitzy-Golay filter over 11 frames in the waveform (Krumm 2001; Savitzky and Golay 1964). The filters are shown in Figure 3.5, and were convolved with the shear wave signal to perform differentiation.

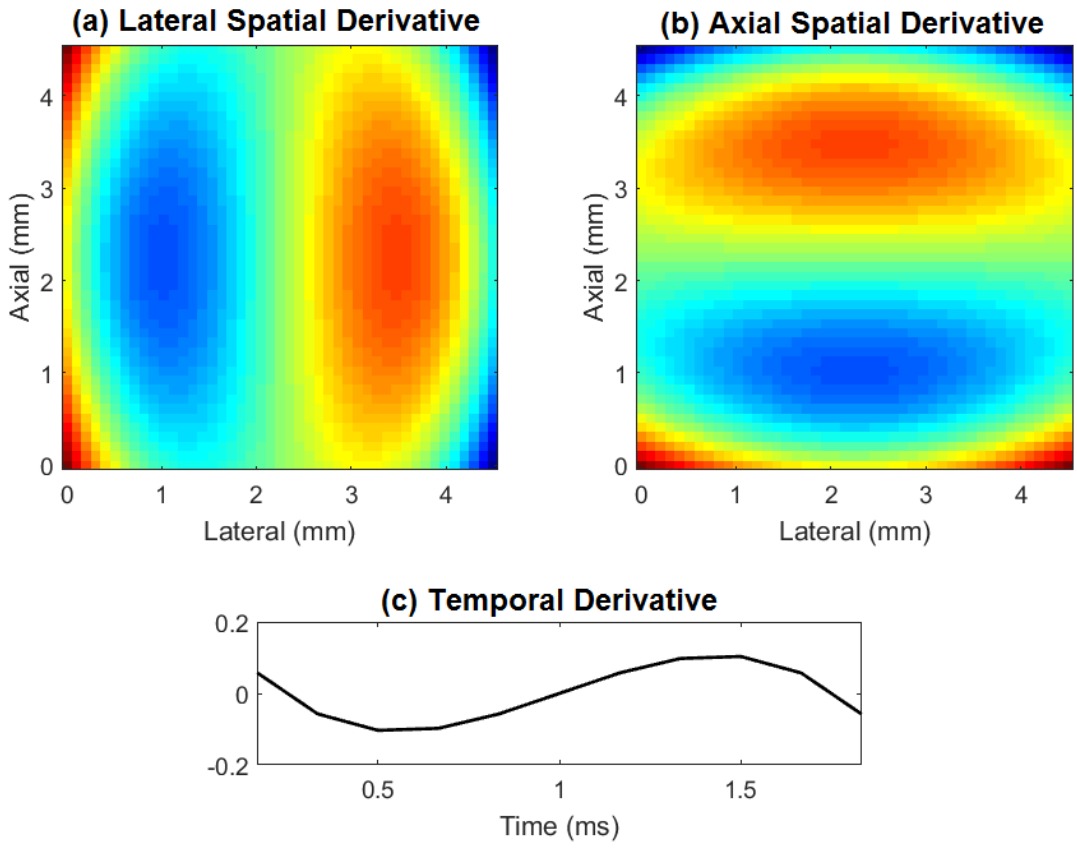

Figure 3.5 Svatsky-Golay filters used for robust numerical differentiation. (a) the lateral 2-D filter used to estimate $\boldsymbol{U}_x$, (b) the axial 2-D filter used to estimate $\boldsymbol{U}_z$ and (c) the temporal filter used to estimate $\boldsymbol{U}_t$. The frame rate for the temporal derivative is 6000 Hz.

This method for wave speed estimation was tested on a computer-generated data set consisting of circularly propagating waves. The MATLAB code showing how these were generated in shown in APPENDIX B. Figure 3.6 (a-c) shows three frames taken from the data set. Waves are shown propagating away from the source which is located in the center of the image. Wave speed decreases with distance. Figure 3.6 (d) shows the resulting wave speed map which matches the

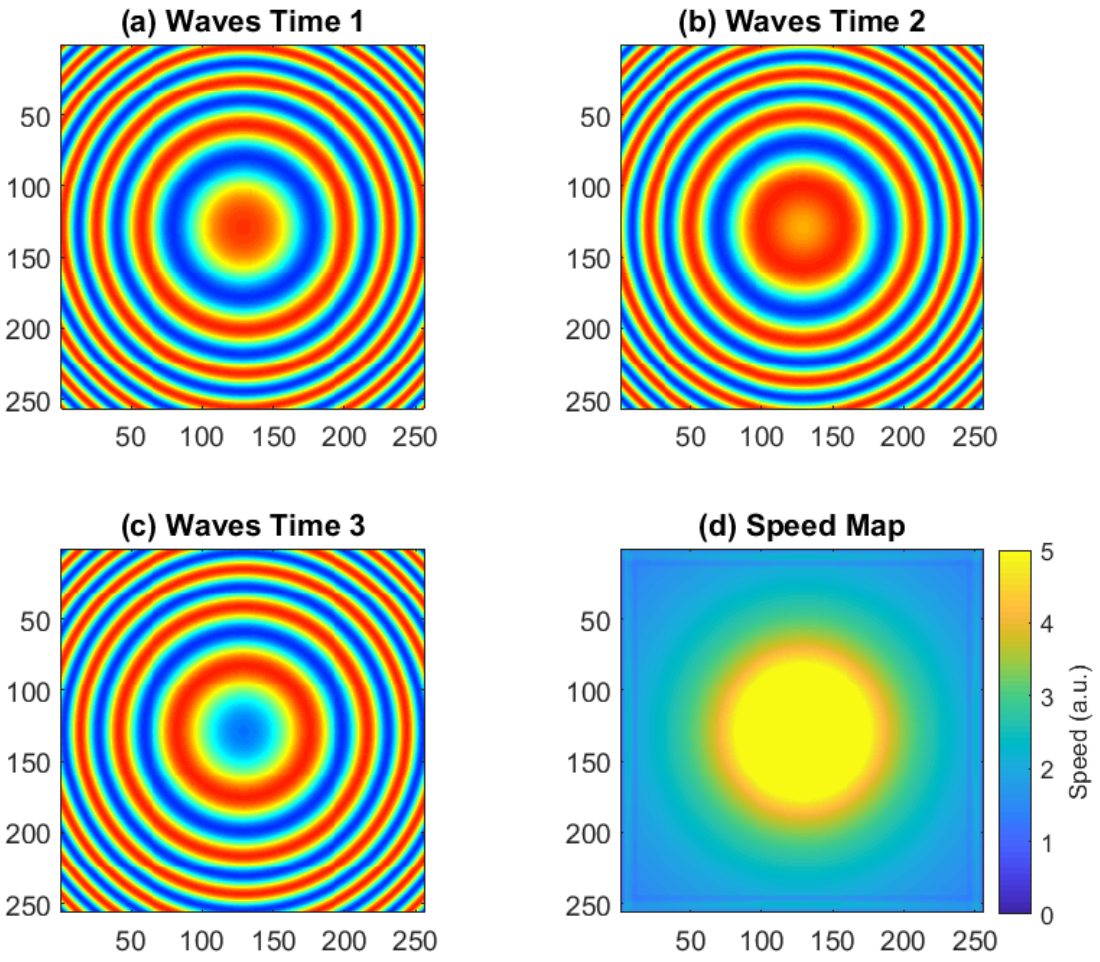

Figure 3.6 (a-c) Three frames taken from a data set of circularly propagating waves. Waves propagate away from the source located at the bottom left of the frame and wave speed decreases with distance. (d) Estimated wave speed using the 1D wave equation. The wave speed goes to infinity at the source.

pattern seen in the data set. Here, because waves are propagating away from the source, the local direction of propagation is always unidirectional and no directional filtering was necessary. However, this cannot be assumed when imaging real tissues and directional filtering is needed.

The final SWS map was calculated by weighted averaging of the directionally filtered speed maps. Weights were calculated in each frame from the percentage of total energy contained at each pixel in the shear wave signal for all valid frames (Deffieux et al. 2012). Only frames unaffected by the temporal Tukey windowing were used for averaging. A total of 214 speed maps ($|\theta| = 2, |n| = 107$) were used in the weighted averaging to produce the final SWS map, given by:

$$c_s(x,z) = \sum_n \sum_\theta c_s(x,z,n,\theta) \frac{|\boldsymbol{U}(x,z,n,\theta)|^2}{\sum_{n,\theta} |\boldsymbol{U}(x,z,n,\theta)|^2}. \quad (3.9)$$

No further spatial averaging was performed on the SWS estimate.

3.2.4. Comparison of SWS Estimation Methods

For comparison to conventional methods, the same post-directionally filtered shear wave data were used to estimate the SWS. The method for 2-D CC used a spatial step size of 20 pixels (2.0 mm), and performed subsample peak estimation by cubic spline interpolation around the maximum point. All spatial and temporal differentiation filters used in the study were kept constant. Because speed estimation via the TTP method uses cyclical shear waves, this method

requires selection of a single shear wave from the data set. For the homogeneous phantoms, a region of interest (ROI) was chosen from the center of each final shear speed map with a spatial size of 15 mm × 15 mm and the mean and standard deviation were taken from the pixels in the ROI. The inclusion phantom contained two ROIs, 5 mm × 20 mm for the background and an 11 mm diameter ROI for the inclusion. Contrast-to-noise ratio (CNR) was calculated by:

$$\mathrm{CNR} = \frac{|\overline{c}_{sI} - \overline{c}_{sB}|}{\sigma_B}, \tag{3.10}$$

where $\overline{c}_{sI}$ and $\overline{c}_{sB}$ are the mean SWS of the inclusion and background respectively and σ_B is the standard deviation of the background SWS.

3.2.5. Mechanical Testing

The nominal SWS was estimated from the average Young's modulus as measured using a compression test (TMS-Pro, Food Tech. Corp., Sterling, VA, USA). Figure 3.7 shows the experimental setup of the compression testing. Compression tests consisted of five samples (~1 cm^3) taken from each phantom, and compressed at a rate of 2 mm/second for 1 second. Young's modulus was calculated from the average slope of the stress-strain curve and the nominal SWS was calculated from the relationship $E = 3\rho c_s^2$, where $\rho = 1000$ kg/m^3 was assumed for all phantoms. Compression tests were performed within 2 hours of

the shear wave imaging. Figure 3.8 shows representative stress-strain curves from the compression test, where the different slopes separate the phantoms.

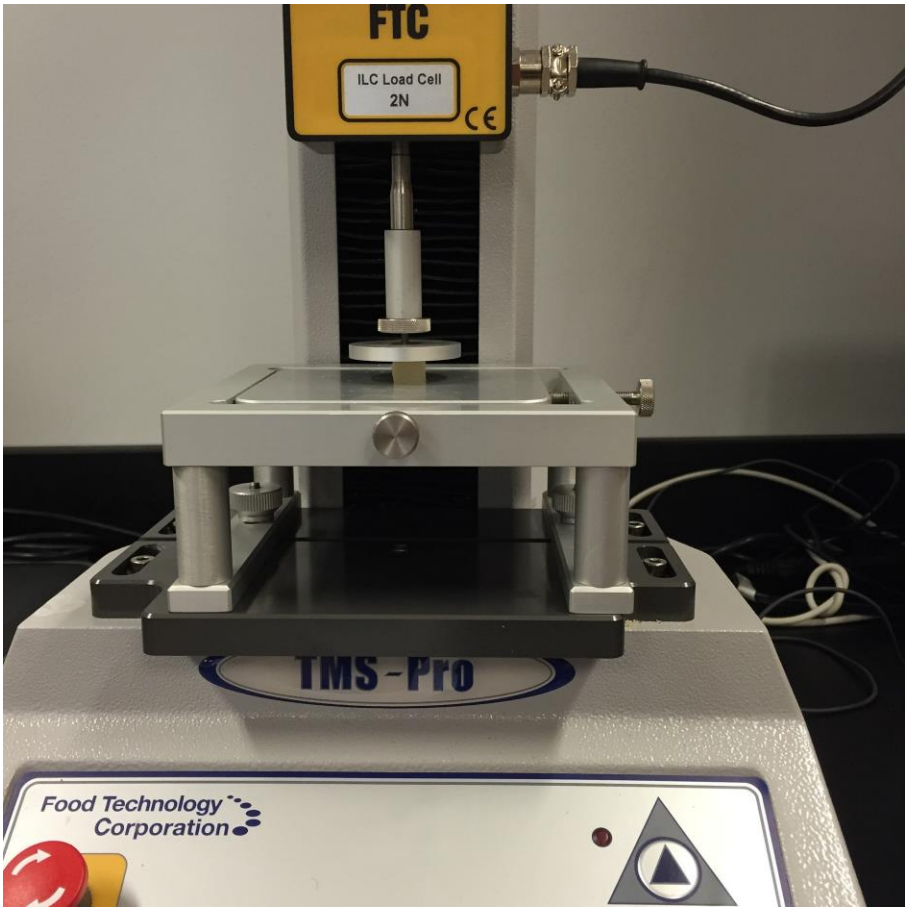

Figure 3.7 Mechanical testing of the ~1 cm^3 blocks taken from the gelatin phantoms. Each gelatin block was compressed at a rate of 2 mm/s for 1 s to estimate Young's modulus and nominal SWS.

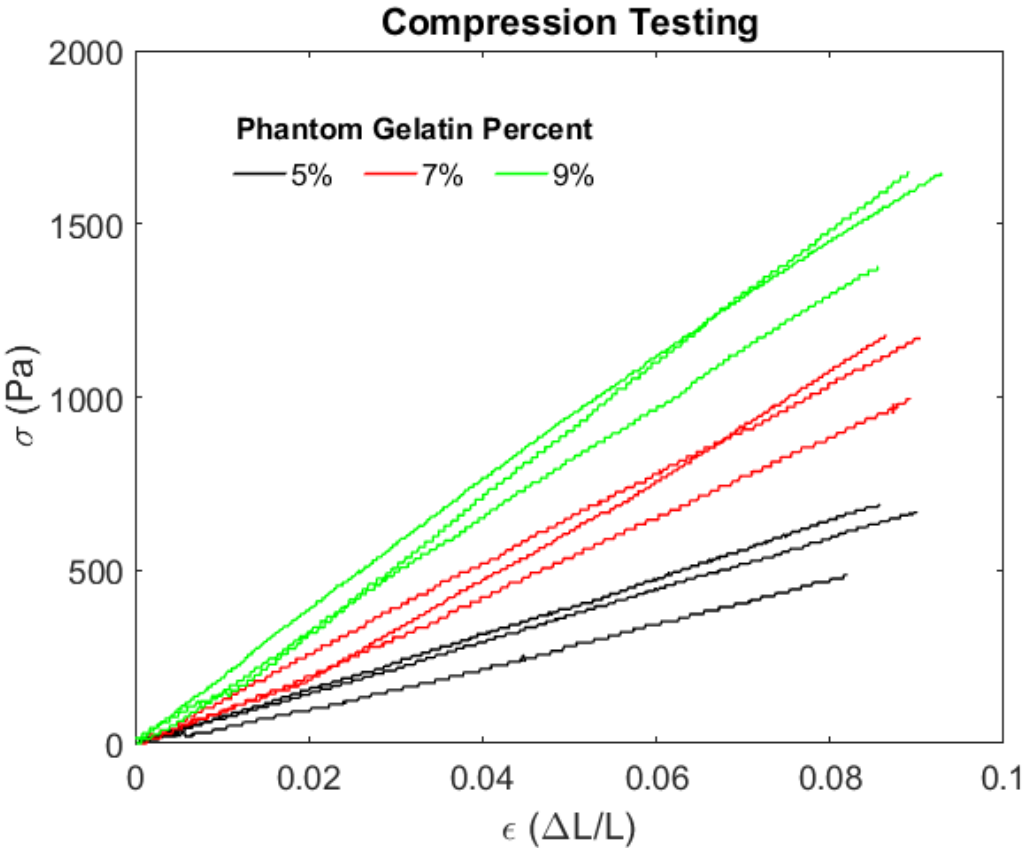

Figure 3.8 Representative stress-strain curves from compression testing of the three phantoms of varying concentrations of gelatin. The slopes of the curves separate phantoms of different gelatin concentrations. Higher gelatin concentrations results in increased stiffness.

3.3. Results

Figure 3.9 shows the *x*-*t* plane of the 3-D spatiotemporal data taken from the center of each phantom (depth of 12.6 mm). The inverse slope of the characteristic curves is representative of the SWS. In Figure 3.9 (d), the slope can be seen to change in the center of the phantom, this represents changing stiffness of the inclusion as compared to the background. Figure 3.10 shows representative images of the shear wave signal from the inclusion phantom taken at 4 ms and 12 ms after start of imaging. This is different from the characteristic curves of Figure 3.9. The change is SWS is most readily visualized by the increase in the wavelength of the shear wave, this increase in wavelength is seen in the center of the inclusion phantom. The corresponding 2-D SWS estimation is shown in Figure 3.11. Similar 2-D SWS maps were acquired from all other imaging frames.

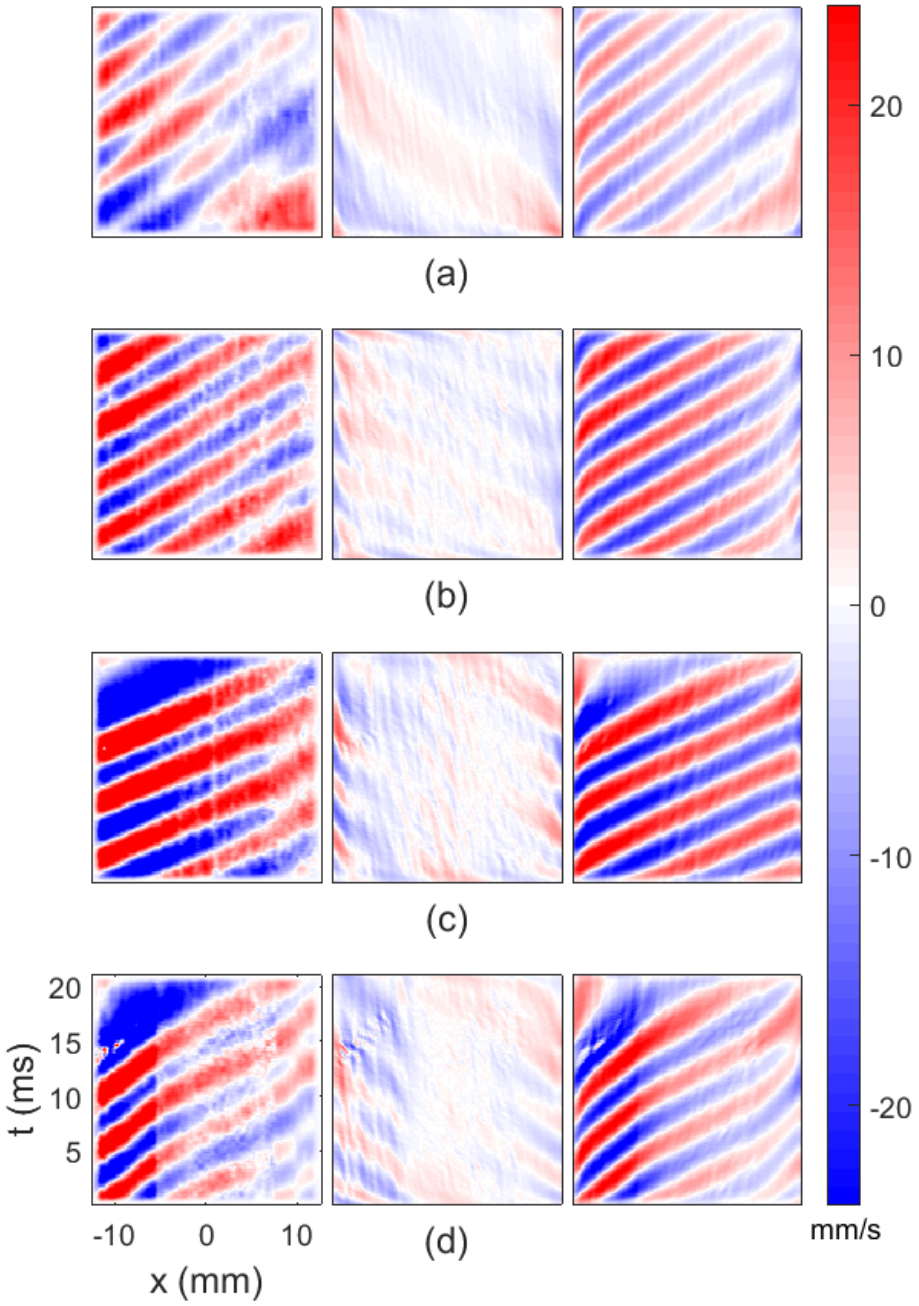

Figure 3.9 Shear waves for phantoms of different stiffness and containing (a) 5%, (b) 7%, and (c) 9% gelatin concentration. The slope of the wave represents the SWS. (d) Inclusion phantom showing different SWS in the center of the phantom than the sides. Columns represent the (left) unfiltered shear wave, (center) the leftward propagating shear waves, and (right) the rightward propagating shear waves.

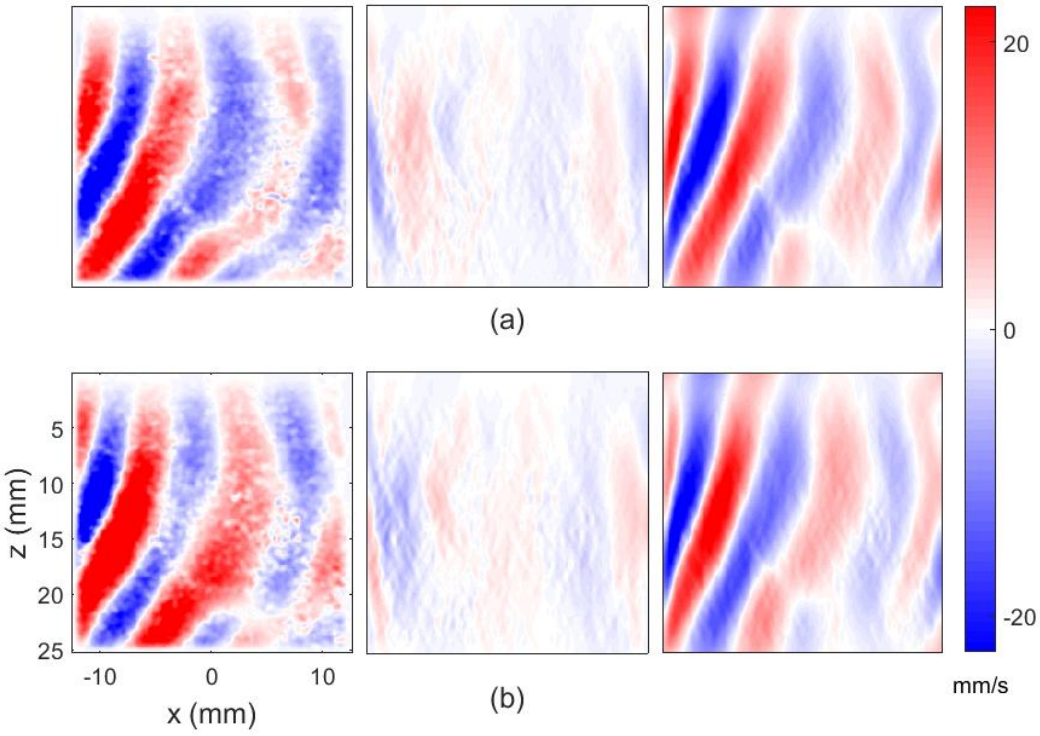

Figure 3.10 Visualization of the continuous shear wave field at a time of (a) 4 ms and (b) 12 ms after the start of imaging. Columns represent the (left) unfiltered shear wave, (center) the leftward propagating shear waves, and (right) the rightward propagating shear waves.

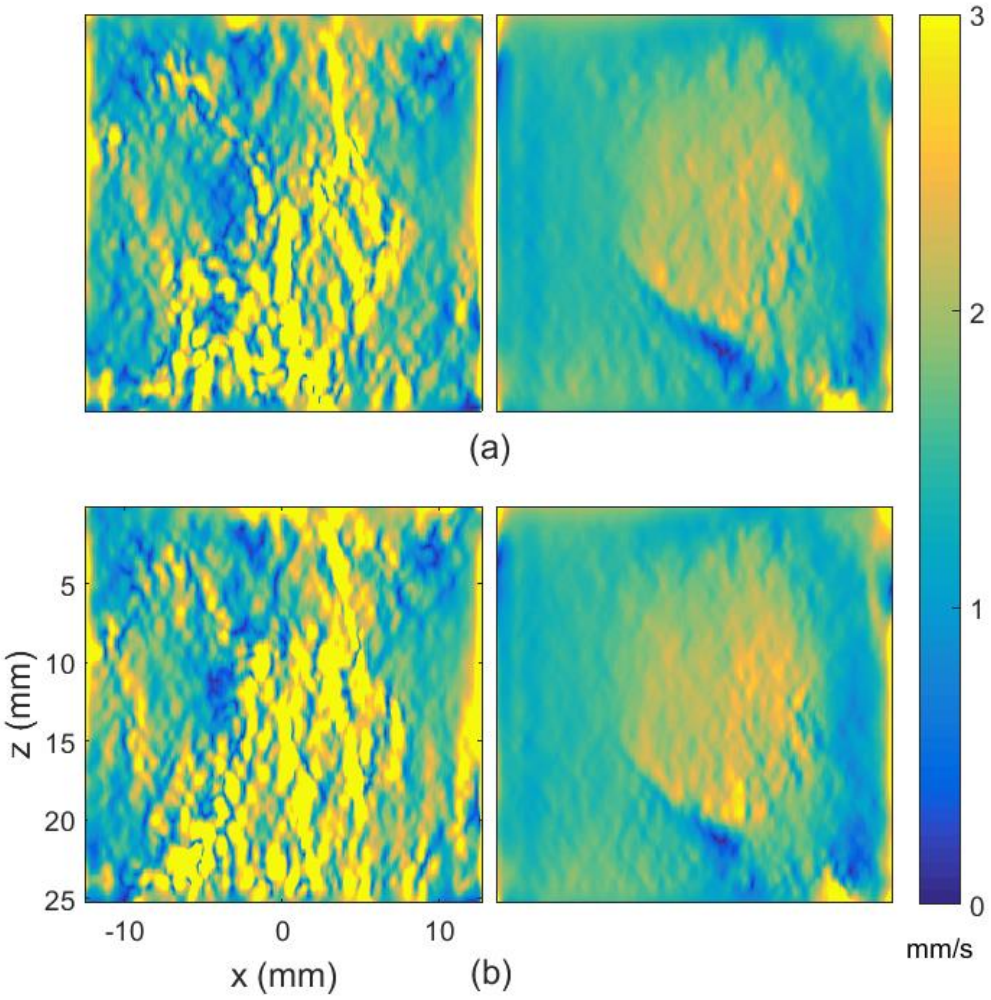

Figure 3.11 Estimation of SWS from the rightward and leftward propagating shear waves for the times (a) 4 ms and (b) 12 ms after the start of imaging. An inclusion phantom was imaged.

For energy based weighted averaging, SWS estimates were multiplied by their energy content normalized to all energy in the post directionally filtered waves at that pixel. Figure 3.132 shows the amplitude of the left-to-right propagating wave. For the inclusion phantom, the right-to-left propagating wave was negligible and is not shown. Figure 3.12 shows representative estimates of the SWS using the

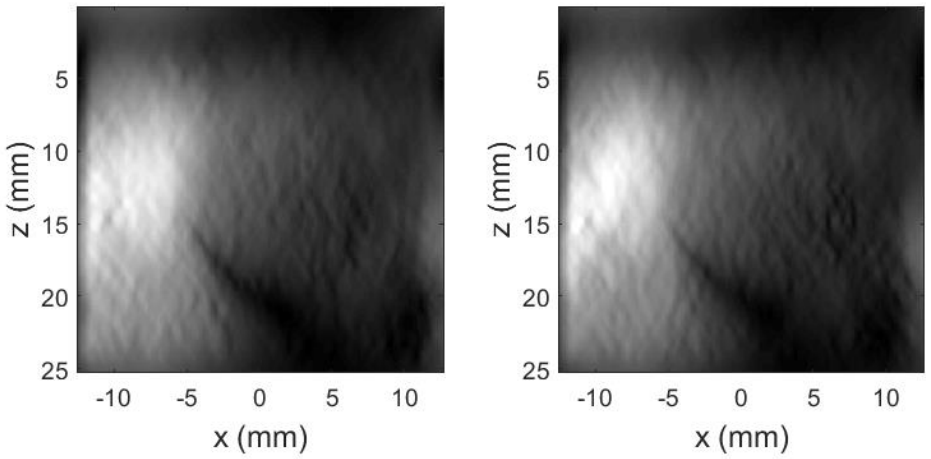

Figure 3.132 Shear wave energy for different times of the rightward moving wave. Energy attenuates as the wave propagates.

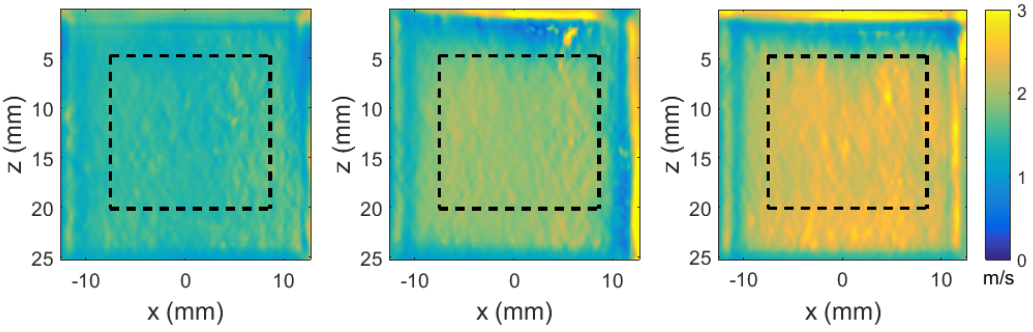

Figure 3.12 Estimated SWS for gelatin phantoms of increasing stiffness. SWS within the black dashed box represents where the mean and standard deviation were taken.

proposed method for three homogeneous phantoms. These are similar across all images taken for each homogeneous phantom. For all methods, the representative means and standard deviation across the pixels within the ROI are shown in Table

3.1. All SWS estimation methods are similar to each other and the SWS estimation using mechanical testing .

Table 3.1 SWS measured from individual phantoms

	SWS (m/s)		
	5% phantom	**7% phantom**	**9% phantom**
TMS-Pro	1.56 ± 0.05	2.12 ± 0.12	2.54 ± 0.10
Experiment	1.52 ± 0.10	1.86 ± 0.10	2.37 ± 0.15
2nd order Wave Eq.	1.45 ± 0.07	1.87 ± 0.11	2.41 ± 0.32
2-D TTP	1.54 ± 0.06	1.83 ± 0.29	2.36 ± 0.16
2-D CC	1.55 ± 0.08	2.04 ± 0.10	2.69 ± 0.20

Figure 3.14 shows the comparison of the average SWS from the compression test, the proposed method of inversion of the first-order wave equation, inversion of the second-order wave equation, the 2-D TTP, and the 2-D CC. Because the compression test provides only an average estimate of SWS for each sample, the mean and standard deviations for the shear wave methods shown here are taken from the average estimate of SWS calculated from the ROI for each imaging sequence. Figure 3.15 shows the inclusion phantom estimated from each SWS estimation method. Table 3.2 shows the data used for CNR estimation for each of the methods, where statistics were taken from the ROIs shown in Figure 3.15 (a). Computational time for a single direction (256 × 256 pixel) 2-D SWS map on a general computing desktop with an Intel i5 CPU at 2.8 GHz took 5 s in MATLAB with no optimization for reduced reconstruction time.

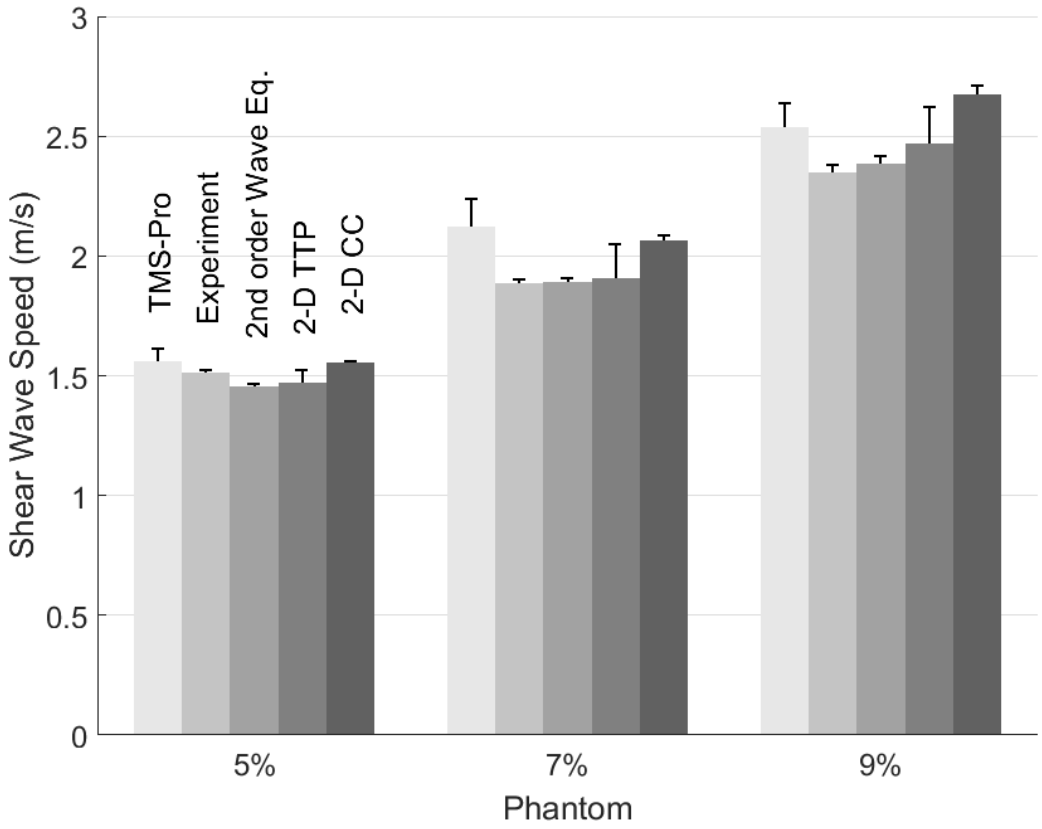

Figure 3.14 SWS estimates from the four ultrasound based methods and the mechanical compression test using phantoms of 5%, 7%, and 9% gelatin concentration.

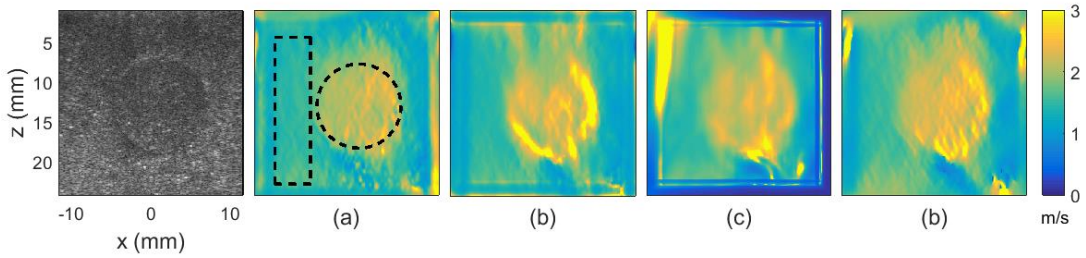

Figure 3.15 SWS map of for the inclusion phantom using 4 methods of SWS estimation. (a) the proposed 1st order wave equation, (b) the 2nd order wave equation, (c) the 2D-TTP method, and (d) the 2D-CC method.

Table 3.2 SWS measured from inclusion phantom

	SWS (m/s)		
	Background	**Inclusion**	**CNR**
TMS-Pro	1.56 ± 0.05	2.54 ± 0.10	N/A
Experiment	1.50 ± 0.06	2.24 ± 0.23	12.47
2nd order Wave Eq.	1.47 ± 0.06	2.33 ± 0.44	14.19
2-D TTP	1.50 ± 0.07	2.24 ± 0.17	10.92
2-D CC	1.58 ± 0.07	2.34 ± 0.19	11.24

- TMS-Pro indices are derived from the homogeneous phantom test.

3.4. Discussion

There are a few approaches to estimate SWS from Eq. (3.6). The proposed method performs an inversion of the associated partial differential equation and estimates c_s from Eq. (3.9). Further methods include TTP and CC based approaches. These methods assume some part of the shape of the wave does not change as it propagates along the characteristic curve. TTP tracks a single point on the waveform (typically a maximum point), and estimates speed based on movement of the single chosen point, while the CC method relies on all points in the waveform. TTP allows for the possibility of multiple peak tracking, where errors from noise can be smoothed out as more peaks pass over a region. For CC, estimation of c_s is performed across all time and a single estimate for c_s is recovered. Because periodic shear waves were imaged, a CC based method for c_s estimation might suffer from errors due to false peaks (Ramamurthy and Trahey 1991). This may not be a problem when imaging a transient pulse; care must be taken when imaging cyclical waves. The proposed method of direct inversion of Eq. (3.8) relies on first-order differentiation for more robust estimates of temporal and spatial derivatives, and provides an estimate of c_s at every time sample where the wave is present. Compounding multiple c_s estimates per direction provides for a robust final estimate. Because an elasticity estimate can be made with very few imaging frames, real time elasticity estimation may be possible using this method. By implementing the proposed method, SWS can be estimated efficiently and accurately while using conventional laboratory equipment, and with improving

GPU capabilities further improvements may be made which only require the number of frames necessary for temporal differentiation and filtering.

Estimates made on homogeneous phantoms using the proposed method are comparable to those found from inversion of the second-order wave equation, 2-D TTP, and 2-D CC methods. From Figure 3.14, because each measurement was taken from an image in different spatial locations of the phantom, the variance between the mean c_s values from each image within the same phantom suggests good repeatability of measurement and homogeneity throughout the phantom. Images made on the inclusion phantom are comparable with the proposed method and most closely match the 2-D CC method. Each method estimated a slow SWS directly below the inclusion. This estimation was caused by the splitting of the shear waves which introduces a sharp gradient perpendicular to the direction of wave propagation and breaks the assumption of a plane wave in the estimation kernel. Further studies which track the true direction of wave propagation may help to decrease this phenomenon.

Shear waves were generated by a mechanical excitation from a single location; thus, shear waves were assumed to resemble plane waves propagating away from the source with little to no reflection from boundaries or inclusions. In this experiment the shear wave is seen to propagate both laterally and axially. Because the direction of propagation may not be known entirely beforehand, to capture most of the energy in a single direction and maintain the form of the wave, wideband directional filters were implemented using a Tukey window with a

tapered-to-constant ratio of 0.75, where the window was $\pm\pi/3$ about the desired direction of wave propagation. The truncated directional bounds allowed the Tukey window to have smooth/sharp drop off while maintaining directionality. If shear waves were assumed to be propagating in unknown directions, or generated at several angles by acoustic radiation force, several narrower directional filters would need to be implemented. This would increase SNR and provide a smoother final image, but may filter out sharp boundaries between tissues of significantly different SWS. Regardless of the number of directional filters, the method proposed here assumes the shear wave is approximated by a plane wave in the estimation kernel. A minimum number of directional filters should be used to meet this assumption. A study with different directional windowing functions might better describe reconstruction image quality for final c_s estimates.

Energy based compounding was used because higher shear wave energy increases the SNR used for SWS estimation. In homogeneous media the shear wave can be assumed to occupy the entire imaging frame. For complex media like a tendon, several layers of differing shear modulus may be present in the imaging frame and shear waves with high SNR may only exist in a given layer for a fraction of the imaging time. With overlapping waves propagating in multiple directions, attenuation due to viscosity lowers the energy of the waves over time and estimates closer to the source contain a higher SNR. Strong reflection from boundaries within the media may also be used for estimates. The energy based compounding method implemented here allows for selective weighted averaging

at times where the initial shear waves are no longer present or where reflected waves may be more dominant.

This study used 20 cycles of external mechanical excitation for generation of near steady state conditions for propagation of shear waves over the entire media. This can be seen in Figure 3.9 where the post-directionally filtered waves cover the entire lateral imaging region for the duration of imaging. Although the external shaker requirement may reduce portability and practicality in most clinical applications, it provides more force for generation of shear waves for imaging elasticity deep with the media or in a much stiffer tissue. Thus, development of an unobtrusive fixation device for an external excitation source may improve usability while providing the force needed to image stiff (such as tendon) or deep tissues (such as the heart).

The use of ARF based SWE allows for the control of shear wave excitation and limits the dominant path of wave propagation in the imaging plane. Because imaging and shear wave excitation are coupled, this may provide improved system usability and reduce shear speed estimation variance over multiple imaging acquisitions. However, because the shear wave only resides in portions of the image at one time, the lower amount of total shear wave energy may reduce the SNR and degrade the estimate for shear speed. This may be overcome by introducing multiple acoustic impulses in a single acquisition event (Song et al. 2012). A study implementing the proposed method of c_s estimation on transient

waves produced from acoustic radiation might better show its use in ARF based SWE.

3.5. Conclusion

This study presented a new inversion method using first-order differentiation for robust estimation of 2-D SWS. This method was validated on homogeneous and inclusion phantoms and results were comparable to measurements from a compression test and three other conventional SWS estimation methods. Implementation on a dedicated device with optimized hardware and software should allow for efficient real-time imaging of the elastic modulus of tissue.

Chapter 4.

Cardiac Atrial Kick Shear Wave Elastography

4.1. Introduction

Estimation of myocardial passive stiffness is important for the assessment of diastolic function and the differential diagnosis of disease. Current methods for myocardial stiffness estimation are made through invasive measures using cardiac catheterization, where the patient may be placed under general anesthesia and will undergo X-ray based fluoroscopy. Both of these are an increased risk for the patient due to ionizing radiation or complication during or following the procedure. To reduce the risks associated with cardiac catheterization, a noninvasive measurement of myocardial stiffness through ultrasound based SWE is developed and presented in this chapter. Implementation of this method helps to ease diagnosis for patients who are suffering, reduce risk, and improve patient outcomes.

Among various methods of introducing shear waves into the myocardium, currently, acoustic radiation force (ARF)-based cardiac SWE shows promise (Couade et al. 2011; Pernot et al. 2011; Song et al. 2016b); however, *in vivo* applications in humans are limited. Difficulties in ARF-based cardiac SWE arise from the poor SNR inherent to cardiac ultrasound. In low SNR imaging, the minute displacements (~μm) of the ARF-induced shear wave are challenging to detect which results in unreliable SWS measurements of the myocardium. This

poses a challenge for clinical applications because **1)** an increasing body mass index (BMI) is associated with reduced SNR in ultrasound, and **2)** elevated BMI is a significant risk factor for reduced diastolic function leading to DHF (Russo et al. 2011). Thus, the population at most risk and who might benefit most from cardiac SWE may not receive its benefits.

To overcome this limitation, a method of cardiac SWE is developed and presented in this chapter which uses shear waves intrinsic to the heart. Here, the shear wave is generated from the heart itself, where the atrial contraction (atrial kick) during late diastole acts as a mechanical stimulus at the base of the heart to generate a wave traveling through the passive ventricular myocardium. This wave travels through the myocardium prior to the electrical activation and contraction of the ventricular myocardium; thus, it may be used to complement electromechanical wave imaging methods which image the timing and propagation of myocardial contraction (Costet et al. 2014; Konofagou and Provost 2012; Provost et al. 2011). The atrial kick shear wave follows (or is associated with) the P-wave seen in an electrocardiogram (ECG). In this way, the atrial kick SWS is an indicator of late diastolic myocardial stiffness and can provide diagnostically useful information to clinicians.

Previous studies performed on the heart used conventional scanning sequences (Pislaru et al. 2014; Pislaru et al. 2017). When imaging uses a conventional line by line scanning sequence the field of view needs to be narrowed to achieve the high frame rates necessary for SWE. Because the field of view is

narrowed in conventional imaging, the tissue being imaged typically needs to be oriented axially as in the apical 4-chamber view. Further, multiple echocardiograms are needed to assess different regions of the heart, such as the IVS and the LV free wall. The use of diverging wave imaging can help to solve the limitations of conventional line by line imaging, open us the use of other cardiac views, and reduce the time for data collection in the clinic.

Moreover, because this method uses the atrial kick shear wave—which to date has only limited research in humans—it is necessary to evaluate the relationship of this wave with other factors/measurements of cardiac health. This will give clinicians a better understanding of how the atrial kick SWS fits into and enhances their current echocardiography reports.

4.1.1. Pulse Inversion Imaging

Pulse Inversion (PI) imaging is a method which has been shown to improve the ultrasound image resolution, contrast, imaging range, and image quality in hard to image patients (Gong et al. 2017; Kornbluth et al. 1998; Thomas and Rubin 1998). Further, PI methods are shown to improve the imaging of tissue displacements in SWE by improving the visualization of the shear wave and thus the SWS estimate (Doherty et al. 2013; Song et al. 2013). This part of the research implements an imaging method which uses PI to better estimate the atrial kick SWS.

To understand how PI works it is first necessary to understand the nonlinear properties of acoustic wave propagation. Previously it was stated that acoustic waves propagate at an average of 1540 m/s in the soft tissues of the body. This speed comes from a linearization of the continuity equations defining acoustic wave propagation. If a second term is included, the wave equation becomes nonlinear and the speed of sound can be defined by (Kinsler et al. 1999):

$$c = c_0 + \beta u, \tag{4.1}$$

where c is now the nonlinear speed of sound, c_0 is the original speed of sound, 1540 m/s, β is to coefficient of nonlinearity, and u is the tissue particle velocity. Because the initial transmitted acoustic wave is a sinusoid, by differentiation the tissue particle velocity is then also a sinusoid. This means that the acoustic speed of sound is different for different parts of the wave. Because of this, the original transmitted sinusoid tends to distort as it propagates and the distortion increases as the ultrasound wave propagates further into the tissue. Figure 4.1 shows an example of this distortion and how it shifts the frequency content of the wave from

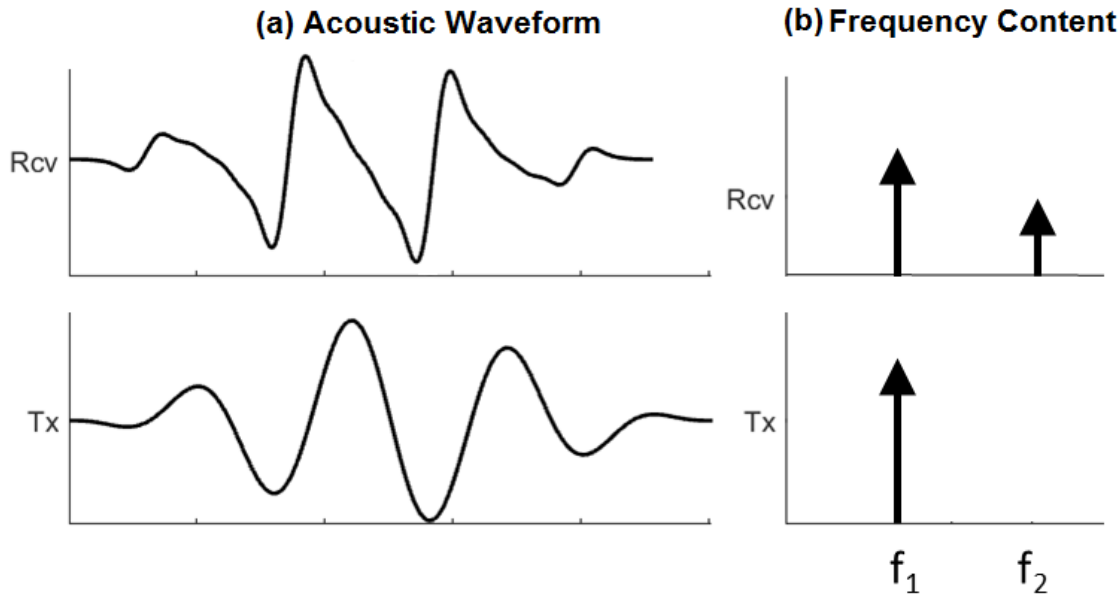

Figure 4.1 (a) Acoustic waveforms for a sinusoidal transmit and the distorted received waveform cause by nonlinear acoustic wave propagation. (b) The frequency content of the original and distorted waves. In the distorted wave the frequency is shifted up to a higher harmonics where represents the fundamental frequency, or transmit frequency, and represents the 2nd harmonic frequency ($f_2 = 2f_1$).

the transmit frequency to higher harmonic frequencies which are integer multiples of the fundamental frequency. Ultrasound harmonic imaging typically uses only the 2nd harmonic; thus, that is all that is shown here.

PI imaging selectively filters for the 2nd harmonic frequency while canceling out the fundamental transmit frequency. The cancellation is done by adding together the RF-data from consecutive transmit/receive events where the transmit pulse waves are identical except for having an opposite polarity. Figure 4.2 shows the two transmit pulses used in pulse inversion. Here, no distortion has occurred and when the two waveforms are added together they cancel out. This cancellation is the way of filtering out the fundamental frequency.

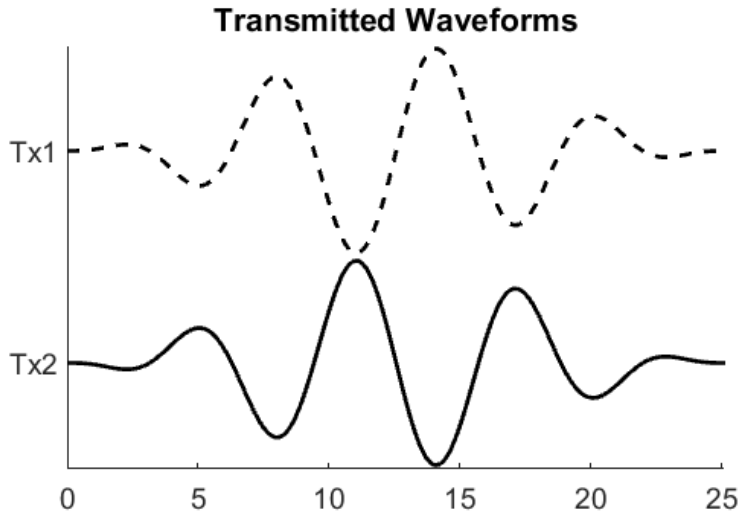

Figure 4.2 Ultrasound transmit waveforms used in PI. A single pulse is transmitted into the body which is followed by an opposite polarity pulse. If they are added together they sum to zero.

When recording the RF-data the waveforms will be distorted. This is shown in Figure 4.3. Because the transmit waveforms are opposite polarity the nonlinear distortion acts of different parts of the waveform and when adding them together only the fundamental frequency cancels out and the 2nd harmonic frequency is doubled. This cancelation of the fundamental and doubling of the 2nd harmonic forms the bases of PI imaging methods. One consequence of this method is the effective frame rate is halved when compared to non-PI methods. Because of its known benefits in SWE and B-mode imaging, PI is used in this part of the research and discussed further in section 4.2.3.

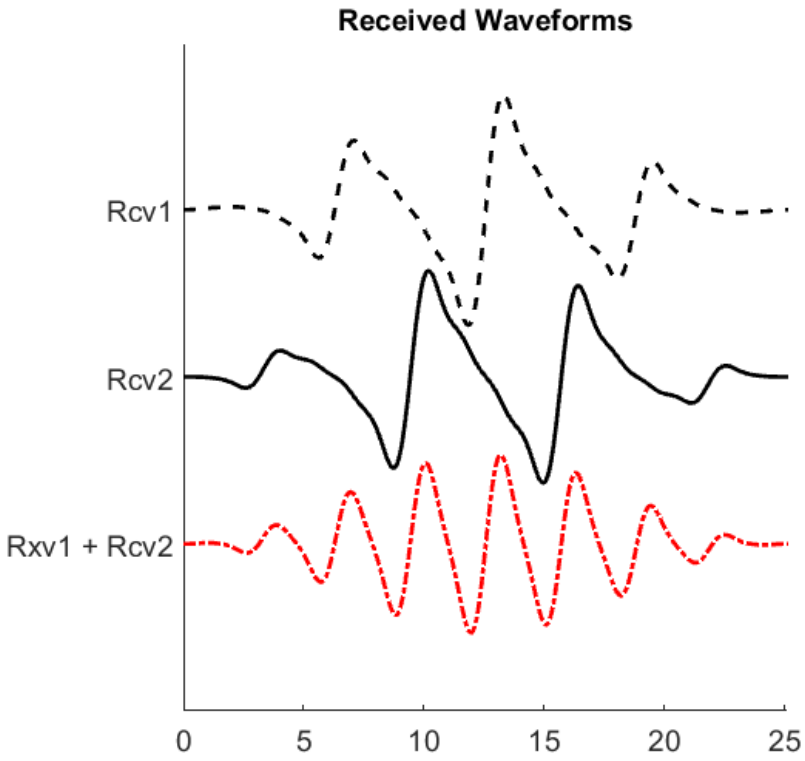

Figure 4.3 The received and distorted waveforms from the two opposite polarity pulses. Because the nonlinear distortion acts on different parts of the waveform their summation cancels out the fundamental frequency but not the 2nd harmonic frequency.

4.2. Methods

4.2.1. Ultrasound Data Acquisition — Cardiac Atrial Kick Shear Wave Elastography

A programmable research ultrasound platform (Verasonics Vantage, Verasonics Inc., Kirkland, WA, USA) and a 64-element cardiac phased array transducer (P4-2v, Verasonics Inc., Kirkland, WA) were used for this study. The ultrasound machine was programmed to perform both B-mode echocardiography and Cardiac Atrial Kick SWE.

Figure 4.4 shows the data acquisition sequence for the ultrasound machine. This sequence begins with a continuous B-mode imaging session to orient the transducer and find the optimal view of the heart for SWE. An apical 4-chamber view was chosen for data acquisition because shear wave motion is maximized in this view. Once the apical 4-chamber view was found the SWE mode was activated. Immediately prior to activation of the SWE sequence the subject was asked to exhale and then to hold their breath for the duration of the sequence, approximately 1.3 seconds.

The SWE mode was designed to record ultrasound data in sync with the heart cycle. This was accomplished by triggering the start of the SWE ultrasound data collection from the QRS-complex of an ECG. Figure 4.5 shows the ECG unit and an example of the ECG signal used to synchronize data collection with the heart cycle. The ECG was run using a data acquisition software (MyDAQ, National Instruments Corp., Austin, TX) with a LabVIEW interface. Following the ECG

trigger, ultrasound data were recorded in two steps **1)** a single B-mode image which was to be used as a reference image was recorded, and **2)** acquisition of 1400 frames of a high frame rate tissue Doppler imaging (TDI) sequence which was designed to visualize tissue motion throughout the heart cycle. The frame rate for this sequence was 1100 Hz. Acquisition of the TDI sequence immediately followed the B-mode reference image. The data were saved and the SWS was estimated from the TDI data offline.

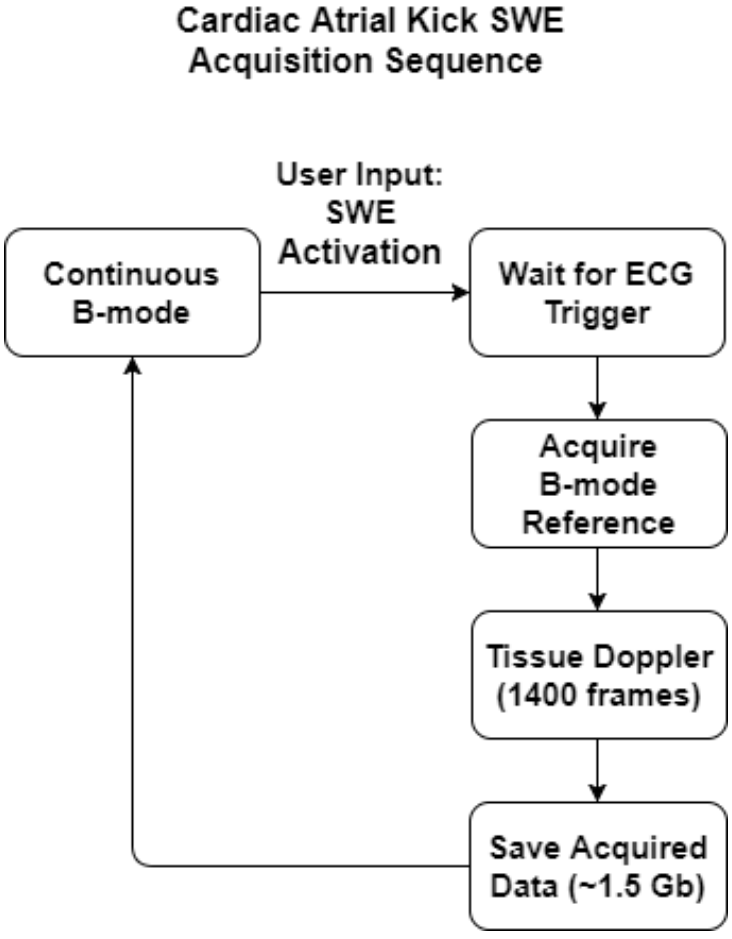

Figure 4.4 The data acquisition sequence for Cardiac Atrial Kick SWE on the Verasonics Vantage ultrasound machine.

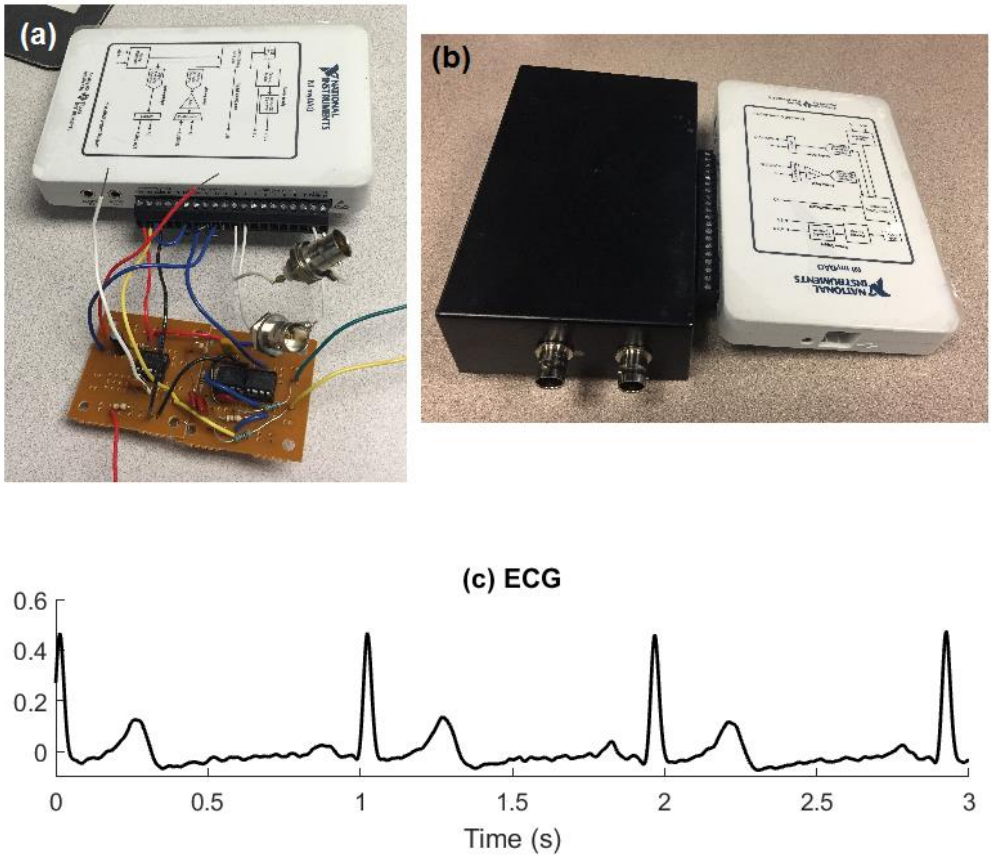

Figure 4.5 (a) ECG circuit, (b) housing for the ECG, and (c) the ECG output in a Lead II configuration.

4.2.2. The Ultrasound Imaging Sequence for B-mode and TDI

Ultrasound imaging for both the B-mode reference image and TDI sequence of the SWE mode consisted of a method where diverging and unfocused ultrasound transmit beams—rather than conventional focused ultrasound transmit beams—were used to insonify the entire heart (Hasegawa and Kanai 2011). Diverging wave transmits were chosen for the SWE mode because previous research has used plane wave imaging methods to insonify the entire imaging region (see Chapter 3); however, plane wave imaging methods do not necessarily

fit for cardiac applications. This is because in order to image the heart the transducer face needs to fit in an intercostal space (between the ribs); thus, it is much smaller than the required imaging region. Diverging waves spread out the acoustic intensity and allow the principles of SWE to extend to cardiac applications.

Figure 4.6 shows the distribution of acoustic energy on the ultrasound transmits used in the TDI sequence and the corresponding individual element transmit delays. Transmit delays for the multiple angles were calculated by moving the virtual focus laterally about the center of the aperture. To calculate these

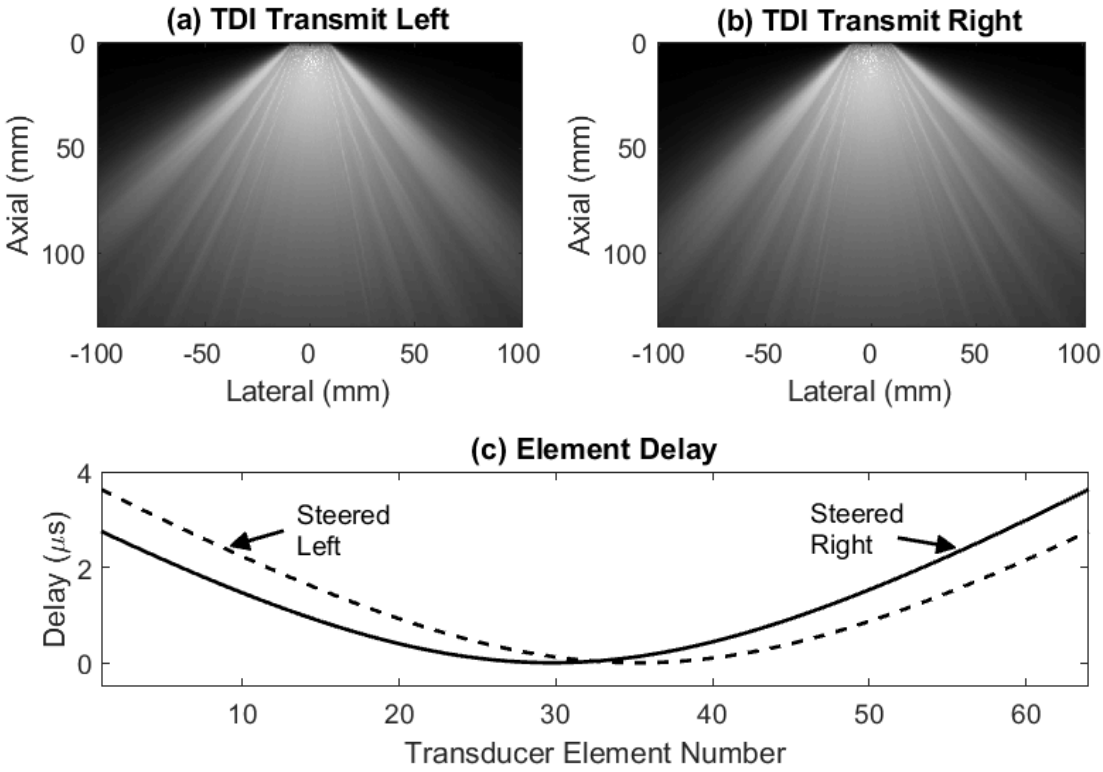

Figure 4.6 Transmit Profiles for (a) leftward and (b) rightward steered and unfocused transmit beams used for the TDI imaging sequence. (c) The transducer element delay calculated for both beams.

delays all ultrasound transmits used a virtual focus 7 mm behind the face of the transducer. As seen from the transmit intensity profiles this allowed acoustic energy to cover the majority of the imaging region. In Figure 4.6 (a) and Figure 4.6 (b) two similar but differently angled transmit profiles are shown. Two angles of insonation are used in TDI because the coherent summation of reconstructed ultrasound images taken using differently angled transmits helps to reduce clutter noise in the image and improve the SNR (Montaldo et al. 2009). A similar method was used in Chapter 3 to improve the SNR when visualizing the shear wave motion. The individual element delays for these two transmits, shown in Figure 4.6 (c), were calculated by moving the virtual focus laterally from -1 to 1 mm behind the face of the transducer.

The B-mode reference imaging consisted of the coherent summation of 12 differently angled insonations of the heart. To do this, the individual element delays for each of the transmits were calculated by moving the virtual focus laterally in 12 equally spaced increments from -3 to 3 mm behind the face of the transducer. A total of 12 transmits were used for B-mode imaging because ultrafast imaging of the heart was not necessary. Ultrafast imaging was needed in the TDI sequence to visualize the shear wave motion.

Figure 4.7 shows the TDI sequence which was designed to acquire data to visualize tissue movement and estimate the atrial kick SWS. From here it is seen that 4 total transmits are used to produce a single final image, where there are 1400 final images. The original transmit sequence consisted of a PI sequence and

the coherent summation of the two differently angled diverging wave transmits. The element PRF was 4.4 kHz and the effective SWE PRF was 1.1 kHz. The maximum tissue velocity before aliasing was 122 mm/s.

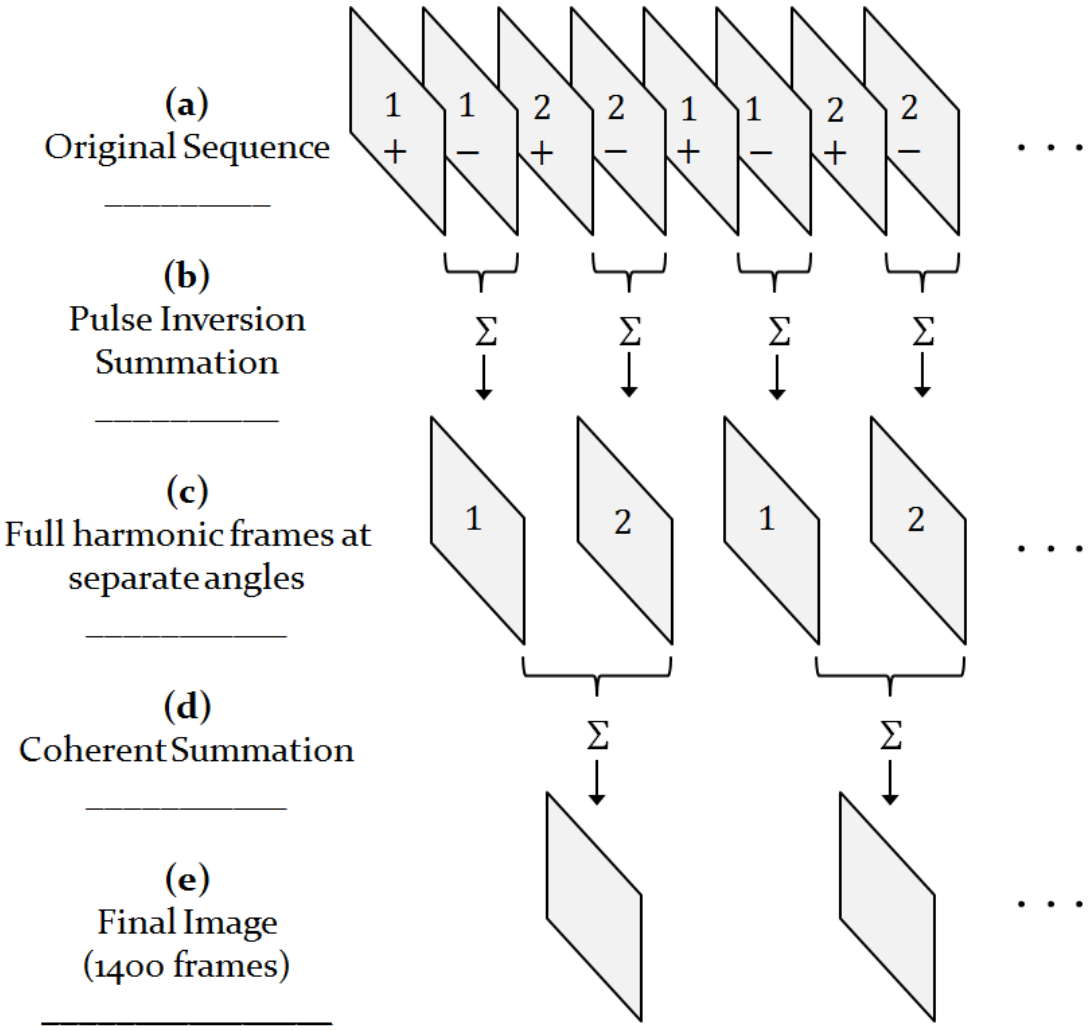

Figure 4.7 Imaging sequence which collects 1400 imaging frames which are used for tissue Doppler velocity estimation and the atrial kick SWS estimation. (a) The original sequence of interleaved polarity pulses, (+, -) and the separately angled frames of diverging transmits (1,2). (b) Pulse inversion is performed on the recorded RF data, (c) the harmonic frames at the two separate angels, (d) coherent summation performed on the full imaging frames, and (d) the final images used for SWS estimation.

4.2.3. PI with Diverging Transmit Waves

This study used an unfocused diverging wave ultrasound transmit. From Eq. (4.1) it was seen that the speed of sound differs with the particle velocity of the acoustic wave. From this, as the acoustic intensity increases the particle velocity also increases and this works to speed up the generation of the 2nd harmonic frequency. For a transmit beam focused in the imaging region, the generation of the 2nd harmonic signal occurs quickly at the focus; however, for diverging wave transmits there is no increase in acoustic intensity once the wave leaves the transducer and the generation of the 2nd harmonic is reduced when compared to focused imaging methods. Because of this, the visualization of the shear waves may also be reduced when using PI imaging with diverging transmit waves. To test the generation of the 2nd harmonic and the feasibility of using PI imaging with diverging waves for the SWE sequence, a series of tests were performed which measured the spectral content of the RF-data from both B-mode and Doppler transmit waveforms when transmitting into the body.

The spectral content was estimated in the following way. From a transmit profile similar to those of Figure 4.6, 10 transmit/receive events were performed. The transmit frequency for the PI sequence was chosen as 1.75 MHz and the 2nd harmonic receive frequency was 3.5 MHz. These frequencies were chosen as they both fell within the manufacturer-specified -6 dB bandwidth of the transducer (1.59 MHz – 3.72 MHz). An initial transmit with a frequency of 3.5 MHz was implemented for reference and comparison to the PI transmit sequence. For each

test, the RF-data were recorded and saved from each of the 64 elements of the P4-2v transducer and for all 10 transmit/receive events. This produced a total of 640 RF-data recordings. Welch's method was used to estimate the PSD for all recordings. The final PSD estimate was the average of all the individual PSDs. Welch's method estimates the PSD by first breaking up the signal into smaller and overlapping blocks of data, estimating the spectral content of each smaller block by Fourier transform, and then averaging the spectral content for all of the smaller blocks in the signal (Welch 1967). The length of each block was 1000 samples and the overlap factor was 90%. A Chebyshev window with sidelobes set to -200 dB was applied to the windowed RF-data prior to the Fourier transform. This ensured that any sidelobes in the resulting PSD was a consequence of the natural windowing of the transmit waveform.

Figure 4.8 (a-b) show the *in vivo* PSD of a 1-cycle B-mode pulse and a 4-cycle Doppler pulse for a transmit frequency of 3.5 MHz. The solid black lines at 1.59 MHz and 3.72 MHz represent the manufacturer-specified -6 dB cutoff frequencies of the transducer. The -6 dB frequencies from the estimated PSD generally matched the specified cutoff frequencies for the transducer. The Doppler pulse, a longer 4-cycle pulse, is seen to have a PSD similar in width to the more broadband B-mode pulse due to the two peaks at frequencies lower than the desired transmit frequency. It is hypothesized that these peaks are due to the natural rectangular windowing of the 4-cycle transmit pulse.

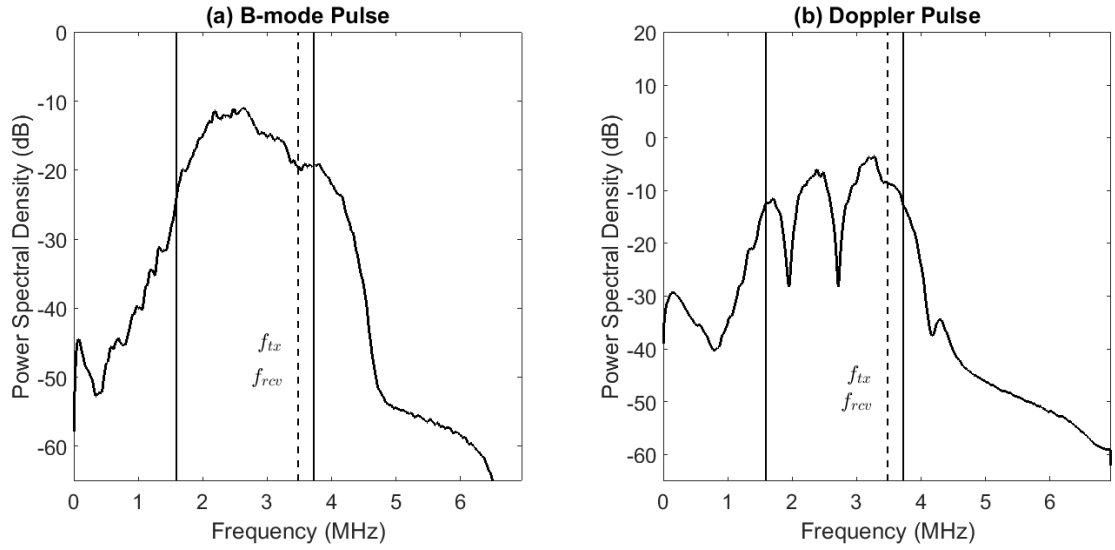

Figure 4.8 *In Vivo* PSD for (a) the 1-cycle B-mode transmit pulse, and (b) the 4-cycle Doppler transmit pulse. The black dashed line represents the transmit and receive frequency of 3.5 MHz while the solid black lines represent the reported -6 dB cutoff frequencies of the transducer.

The PSD of the harmonic imaging sequence was estimated from three different conditions, **1)** a single transmit/receive, **2)** a PI sequence of two transmits of opposite polarity summed after receive, and **3)** two transmits of equal polarity summed after receive.

Figure 4.9 (a) shows the PSD of the B-mode transmit pulse when the transmit frequency was 1.75 MHz. The 2nd harmonic and receive frequency for this was 3.5 MHz. For the single and double transmit pulses without PI the main lobe is centered around the transmit frequency. The double transmit summation is about 3 dB greater in magnitude than the single transmit pulse, which is expected as 3 dB represents double the power. The 2nd harmonic frequency is buried in what may be

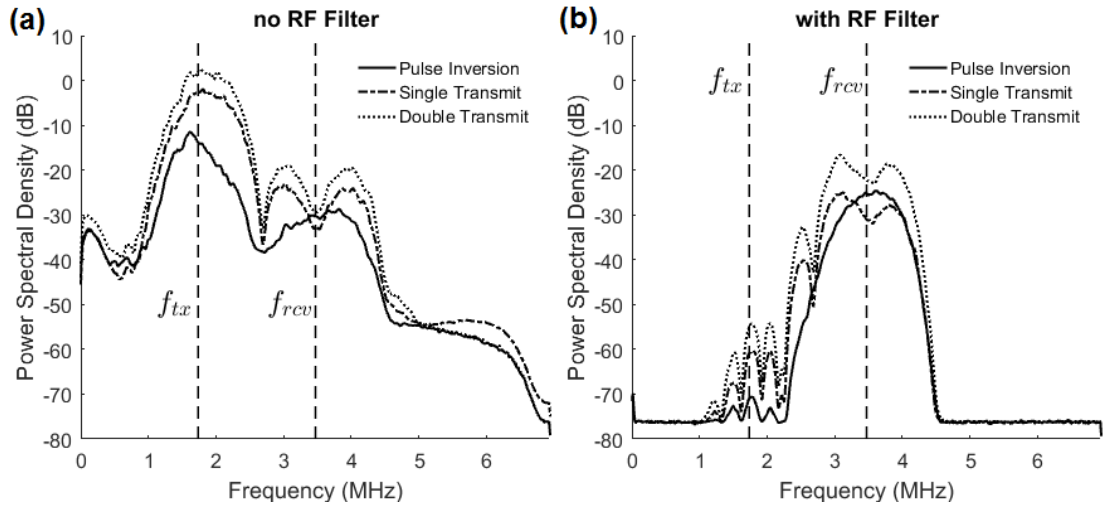

Figure 4.9 *In Vivo* PSD of the transmitted B-mode pulse (a) before filtering and (b) after RF-data filtering.

the side lobes from the main lobe. While the two side lobes appear to be elevated around the 2nd harmonic, suggesting it is generated, this elevation may be caused by the natural frequency response of the transducer. It cannot be determined from here if the 2nd harmonic is being generated. Moreover, assuming it is generated then an image reconstructed using the 2nd harmonic will be corrupted by data from the fundamental frequency. Simply filtering out the fundamental frequency will not work in this case. After application of the PI sequence the main lobe on the transmit frequency as well as the side lobes obscuring the 2nd harmonic are reduced and the peak around the 2nd harmonic is more prominent. This suggests that the 2nd harmonic is generated using the diverging transmit profile with the 1-cycle transmit waveform and that the PI sequence is working to cancel out the fundamental transmit frequency. However, even after application of the PI

sequence the magnitude of the fundamental is still several dB greater than that of the 2nd harmonic and filtering of the RF-data is still needed. Figure 4.9 (b) shows the response after applying the RF-data filter. Figure 4.11 shows the magnitude

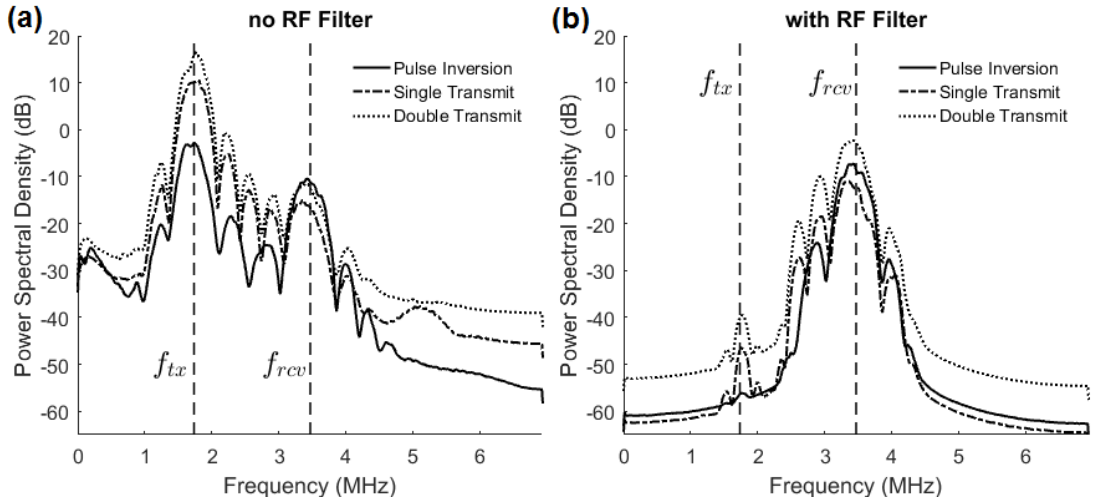

Figure 4.10 *In Vivo* PSD of the transmitted Doppler pulse (a) before filtering and (b) after RF-data filtering.

response of the filter.

Figure 4.10 (a) shows the PSD for the 4-cycle Doppler transmit pulse when using the same 1.75 MHz transmit frequency as the B-mode pulse. As before, the most prominent peak is centered around the transmit frequency and this lobe is narrower due to the extended transmit pulse. The single and double Doppler transmits show a more pronounced 2nd harmonic frequency than the B-mode pulse. This may be because the greater power in the extended transmit pulse generates the 2nd harmonic frequency faster, or because the side lobes fall off faster for the narrower bandwidth pulse and do not obscure the 2nd harmonic peak. After

application of the PI sequence the fundamental frequency was reduced and the peak around the second harmonic was increased by about 3dB. However, as before the fundamental frequency content dominates the 2nd harmonic and the RF-data would still need to be filtered. The PSD after filtering is shown in Figure 4.10 (b).

For both B-mode and Doppler transmits, PI enhanced the power of the 2nd harmonic while reducing the power of the fundamental frequency. This is the purpose of PI imaging (Duck 2002). A perfect cancellation of the fundamental frequency would occur if there were no movement of the underlying tissue and would thus isolate the 2nd harmonic. As seen in Figure 4.8 and Figure 4.9 the cancelation is imperfect. This is due to the rapid movement of the heart from one ultrasound transmit to the next. Because of the imperfect cancelation, the RF-data requires filtering to further isolate the 2nd harmonic before processing and image display. This would suggest that PI has no purpose when imaging rapidly moving tissue such as the heart; however, because PI reduced the side lobes from the fundamental and made the 2nd harmonic peak more prominent, it was implemented for this part of the research along with the RF-data filter shown in Figure 4.11.

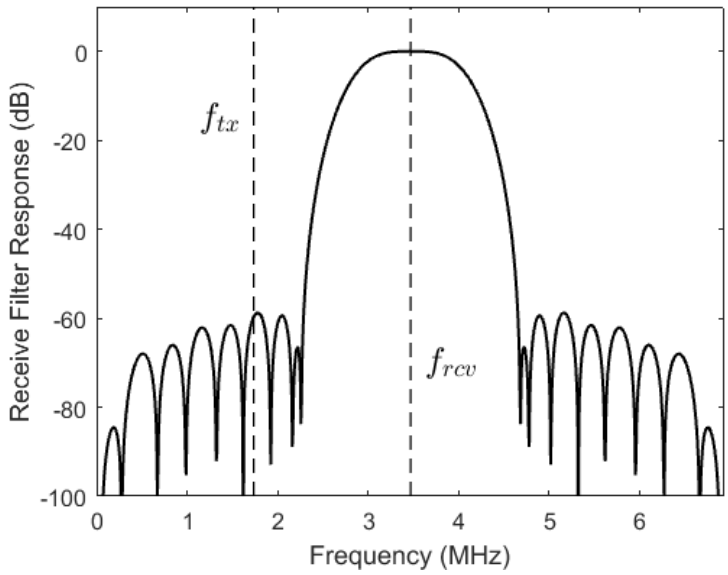

Figure 4.11 RF-data filter used for ultrasound data acquisition.

4.2.4. Estimation of the Atrial Kick SWS

The atrial kick SWS was estimated from the tissue velocity in late diastole. Tissue velocity was estimated from the IQ image data using the phase based 2-D autocorrelation method shown in Eq. (2.7). Autocorrelation coefficients were smoothed spatially using a 10×10 pixel (4.4×4.4 mm) moving average and temporally using a 3 pixel (2.7 ms) moving average. Figure 4.12 shows four frames of the tissue velocity during the atrial kick overlaid on the reference B-mode image. The atrial kick wave is of negative velocity and propagates up through the heart from the base to the apex. This corresponds to the contraction of the atria progressively pulling down the myocardium. The direction of propagation in relation to the tissue motion is suggestive of a longitudinal shear wave (Catheline

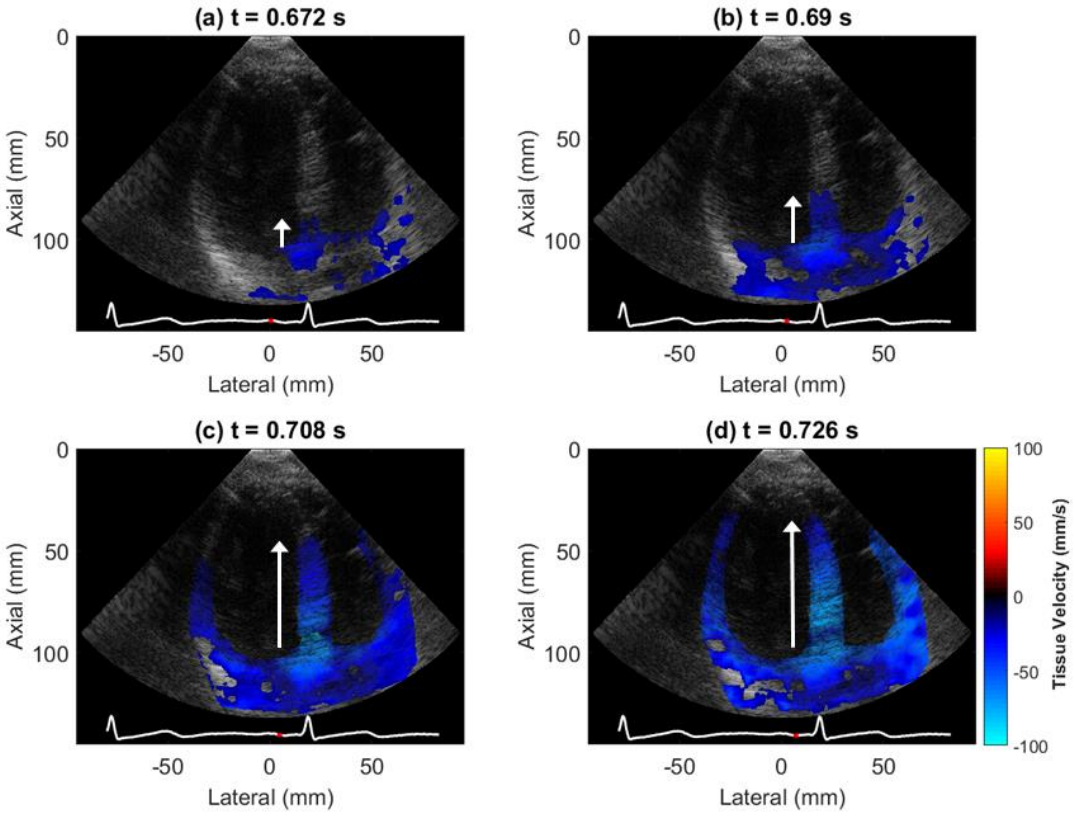

Figure 4.12 Wave Propagating through the heart at times of (a) 0.672, (b) 0.69, (c) 0.708, and (d) 0.726 seconds after the start of data collection. All images use the same colorbar to visualize tissue velocity. Tissue velocity above -15 mm/s is not shown here in order to visualize the wave propagating through the heart. The SWS is estimated from the wavefront. Arrows indicate wave propagating up through the heart.

and Benech 2015). Using the B-mode as a reference, a curve was drawn through the IVS, tissue velocity was reconstructed along the curve and plotted against time. The red dashed line in Figure 4.13 shows the curve through the interventricular septum. Figure 4.14 shows the representative tissue velocity along the IVS and through the heart cycle for four subjects. The atrial kick shear wave is seen in late diastole and corresponds with the P-wave in the ECG. The SWS was estimated from the slope of a linear regression along the leading edge of the wave. The linear

regression used a least absolute residual (LAR) method for robust SWS estimation. The leading edge was defined as the isovelocity line at 25% of the maximum tissue velocity of the atrial kick wave (Shahmirzadi et al. 2012). The white dashed line in Figure 4.14 in late diastole represents this linear regression. This method of SWS estimation was chosen because it allowed for measurement of the SWS from the wavefront and was not influenced by the non-wave-like motion which followed the initial wave propagation.

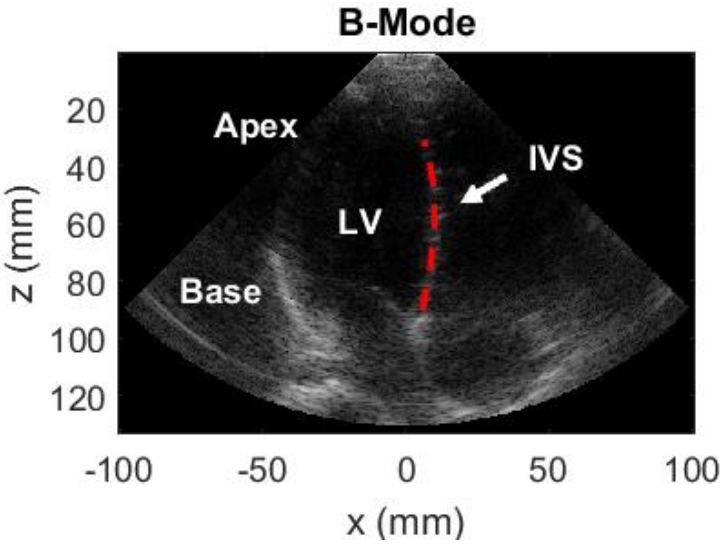

Figure 4.13 B-mode reference image. Tissue velocity is reconstructed along the red dashed line through the interventricular septum.

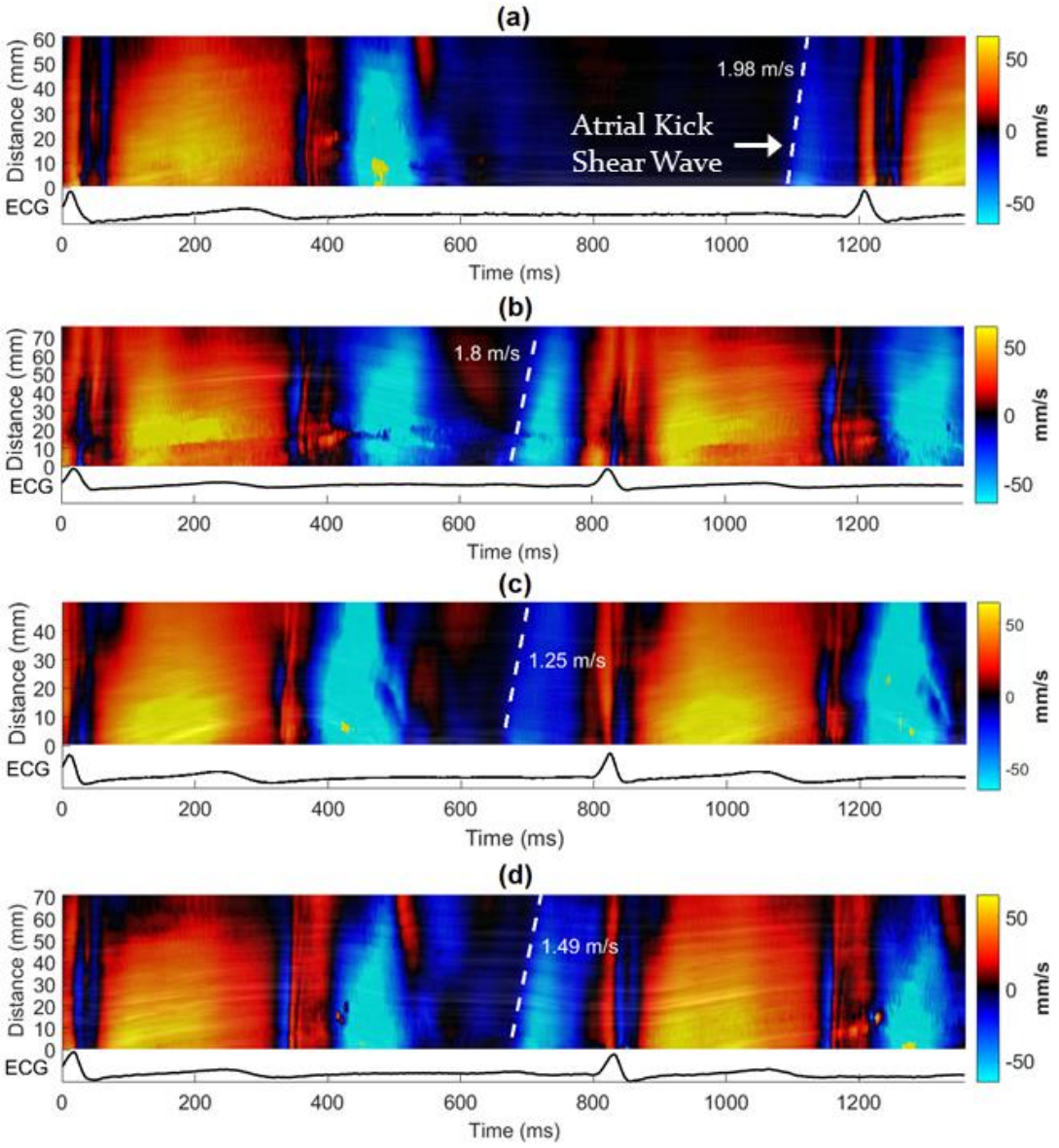

Figure 4.14 (a) – (d): Representative tissue velocity and ECG of four subjects recorded for about 1.27 seconds. Tissue velocity is reconstructed along the interventricular septum. The atrial kick shear wave is identified in late diastole and the slope of the white dashed line represents the atrial kick SWS.

Because the SWS estimate is in late diastole, the myocardium is considered to be relatively motionless (compared to imaging duration) before shear wave generation. This assumption may be violated in the event of E'-A' fusion. This is when the diastolic phase of the heart cycle is shortened and atrial contraction begins before the end of the early filling phase. Rather than two distinct patterns of tissue movement in diastole there is only one. Thus, no atrial kick shear wave is identified. Figure 4.15 shows an example of E'-A' fusion. SWS measurements were discarded when this occurred.

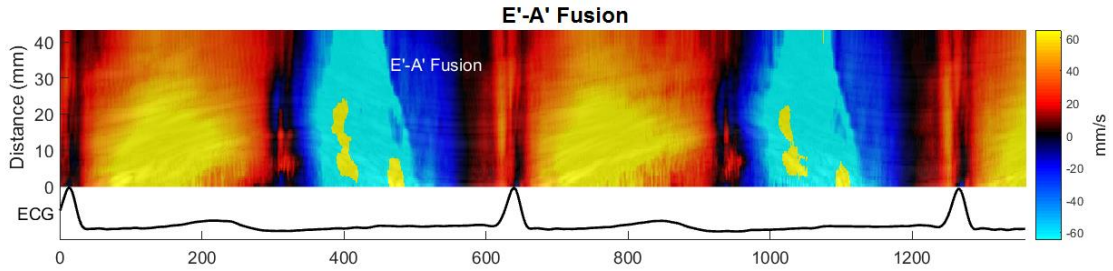

Figure 4.15 Example of E'-A' fusion from one of the subjects in this study. No atrial kick shear wave is seen in the tissue velocity measurement.

4.2.5. Subject Population

This research described here was approved by the University of Nebraska-Lincoln Institutional Review Board (IRB) and all participants provided their written informed consent before inclusion into the study. This research is composed of two parts, **1)** a study to assess the day-to-day variability of the SWS estimation, and **2)** a study investigating the relationship between the SWS and other measures of health. Four healthy adults were recruited into the first study of day-to-day variability while 14 healthy adults were recruited into the second study correlating measures of health to the SWS. Subjects were excluded if they had a history of heart disease.

4.2.6. Day-to-Day Variability of the Atrial Kick SWS

For the first study assessing the day-to-day SWS variability, participants in this study were scheduled for three consecutive days of ultrasound data acquisition. Scheduling was at the same time each day and participants were asked to refrain from caffeine intake and exercise prior to each visit. Each day consisted of a total of five ultrasound data acquisitions for a total of 15 data acquisitions per subject. To reduce potential bias from using the same ultrasound view for each data acquisition, ultrasound imaging was stopped between acquisitions and the transducer was removed from the surface of the body. The mean and standard deviation of the SWS was calculated from the five estimates on each day. A 1-way ANOVA test was performed to determine differences within each subject over the three days of data acquisition.

4.2.7. Comparison of Atrial Kick SWS to Common Health Measures

For this part of the research, prior to any ultrasound imaging, common clinical measures were recorded. These included the participant's age, sex, height, weight, blood pressure, and heart rate. Blood pressure was measured from the left arm using an automated blood pressure cuff. From the height and weight measurements the BMI and Body Surface Area (BSA) were estimated (Haycock et al. 1978). BSA was estimated because it is a parameter highly correlated to the size of cardiac structures and is commonly used as a reference measure to assess cardiac abnormalities (Lopez et al. 2010; Sluysmans and Colan 2005).

Ultrasound data acquisition followed the recording of the clinical data measurements. The measured ultrasound data included the atrial kick SWS, the peak tissue velocities in systole (S'), early diastole (E'), and late diastole (A'), and the isovolumetric relaxation time (IVRT'). The IVRT' was measured as the time between the ending of the S' wave and the beginning of the E' wave. From the peak tissue velocities in diastole the E'/A' ratio was calculated. These measurements were taken using tissue velocity measurements in the IVS at the depth of the mitral annulus and using recommended quantification methods in echocardiography (Lopez et al. 2010; Nagueh et al. 2009). A total of five measurements were taken for all ultrasound based measures and the mean and standard deviation for each participant were calculated.

Pearson's correlation coefficient (r) was calculated to investigate the linear relationship the conventional measurements and the atrial kick SWS. Statistical

significance of the linear correlations was found using a t-test, where p-values less than 0.05 were considered significant. Pearson's correlation coefficient is defined as:

$$r = \frac{cov(X,Y)}{\sigma_X \sigma_Y}, \tag{4.2}$$

where $cov(X,Y)$ is the covariance of the random variables X and Y which represent the SWS and the other measures of health and σ_X and σ_Y represent their standard deviations.

The intra- and inter-rater correlation of the SWS measurement was estimated. The intra-rater correlation was found by having the same reader select a line through the IVS on two separate occasions, from which the SWS was estimated. The inter-rater correlation of the SWS measurement was estimated by having two separate readers select lines through the IVS and estimating the SWS. The correlation between the results was calculated using Pearson's correlation coefficient. Statistical significance between the readings was found by first using a Fisher z-transformation on the coefficients and then performing a Z-test (Fisher 1921).

The mean absolute error (MAE) of the measurements were calculated by:

$$MAE = \frac{1}{N}\sum_{i=1}^{N} |A_i - B_i|, \tag{4.3}$$

where N is the total number of SWS estimates, and A_i and B_i represent the SWS measurements from the multiple readings. A paired student's t-test was performed to determine if the differences were statistically significant. Statistical significance was considered as a p-value less than 0.05.

4.3. Results

4.3.1. Day-to-Day Variability of the Atrial Kick SWS

Figure 4.16 shows the results of the day-to-day variability measurements. Subject three presented with an increased heart rate on day two which shortened diastole, causing E'-A' fusion, and resulted in no SWS estimate for that day. Subject four fell ill during the three days scheduled for data acquisition and was unable to attend on the third day. From the one-way ANOVA test, there was no statistically significant difference in the SWS for any subject across the three imaging days. Significance levels were ($p = 0.71$, $p = 0.97$, $p = 0$ 0.83, and $p = 0.27$) for subjects one through four respectively.

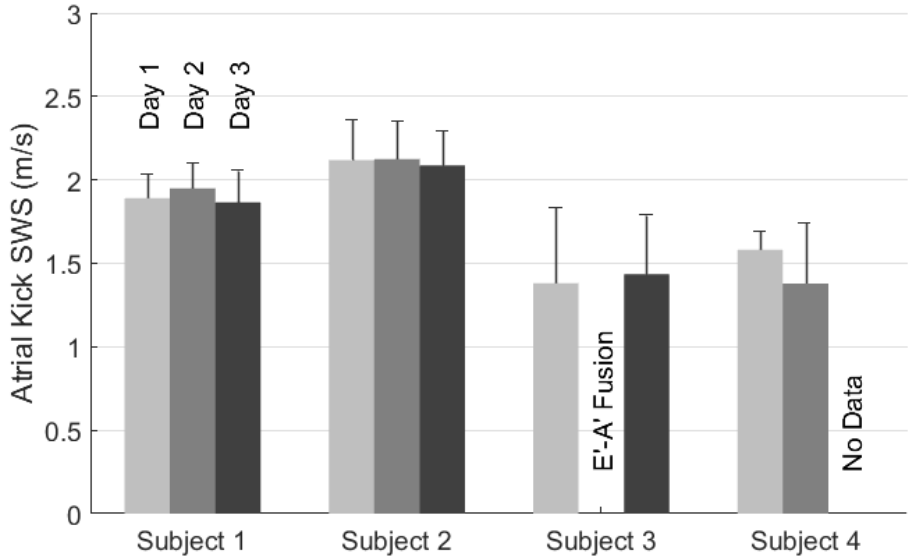

Figure 4.16 Estimated SWS (means ± standard deviation) for 4 subjects across three consecutive days. E'-A' fusions resulted in no estimate for subject 3 on day 2 while subject 4 was unable to compete data collection.

4.3.2. Estimation of the Atrial Kick SWS and Correlation to Common Health Measures

Figure 4.17 shows the mean and standard deviation of the atrial kick SWS for each of the 14 healthy subjects. Table 4.1 shows the overall subject characteristics in this study and Table 4.2 shows the ultrasound derived characteristics. For all subjects, the SWS was 1.78 ± 0.34 m/s. This falls within the range of previously reported SWS measurements (Couade et al. 2011; Pernot et al. 2011; Pislaru et al. 2014; Song et al. 2014b). When correlating the SWS to the conventional measures of health, only the systemic diastolic pressure, E', E'/A', and the IVRT' were found as statistically significant. Figure 4.18 visualizes these significant correlations along with the 95% confidence intervals and the 95% predictions intervals. There was no

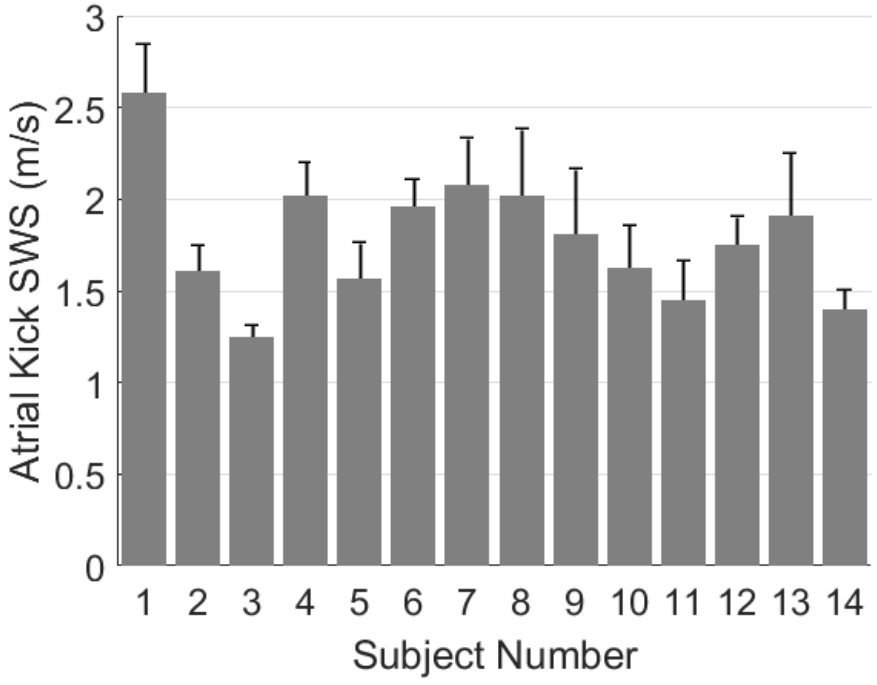

Figure 4.17 Mean and standard deviation of the atrial kick SWS for each subject.

statistically significant correlation found between systemic systolic pressure, heart rate, age, height, weight, body surface area, body mass index, or sex.

Table 4.1. SUBJECT CHARACTERISTICS

	Mean ± Std. (n=14)	***Range***	***Corr. to SWS (p)***
Age (y)	24.7 ± 3.0	21.1 – 29.3	0.40
Sex (male/female)	7/7	N/A	0.79
Heart Rate (bpm)	75.9 ± 11.2	61 – 94	0.31
Systolic Pressure (mmHg)	112 ± 10.7	104 – 139	0.08
Diastolic Pressure (mmHg)	79.2 ± 7.5	68 – 93	0.002*
Height (in)	67.9 ± 3.5	62.2 – 74	0.14
Weight (lbs)	155 ± 31	113 – 206	0.19
Body Surface Area (m^2)	1.84 ± 0.23	1.52 – 2.19	0.17
Body Mass Index (kg/m^2)	23.4 ± 3.13	19.4 – 28.6	0.42

*Indicates statistically significant linear correlation ($p < 0.05$).

Table 4.2 Ultrasound Derived Characteristics

	Mean ± Std. (n=14)	***Range***	***Corr. to SWS (p)***
Atrial Kick SWS (m/s)	1.78 ± 0.34	1.25 – 2.58	N/A
S' (mm/s)	102.5 ± 16.2	74 – 134	0.50
E' (mm/s)	152 ± 18.7	105 – 177	0.024*
A' (mm/s)	94.2 ± 16.5	64.5 – 121	0.27
E'/A'	1.68 ± 0.43	1.05 – 2.59	0.028*
IVRT' (ms)	69.8 ± 11.2	52.4 – 92.2	0.023*

*Indicates statistically significant linear correlation ($p < 0.05$).

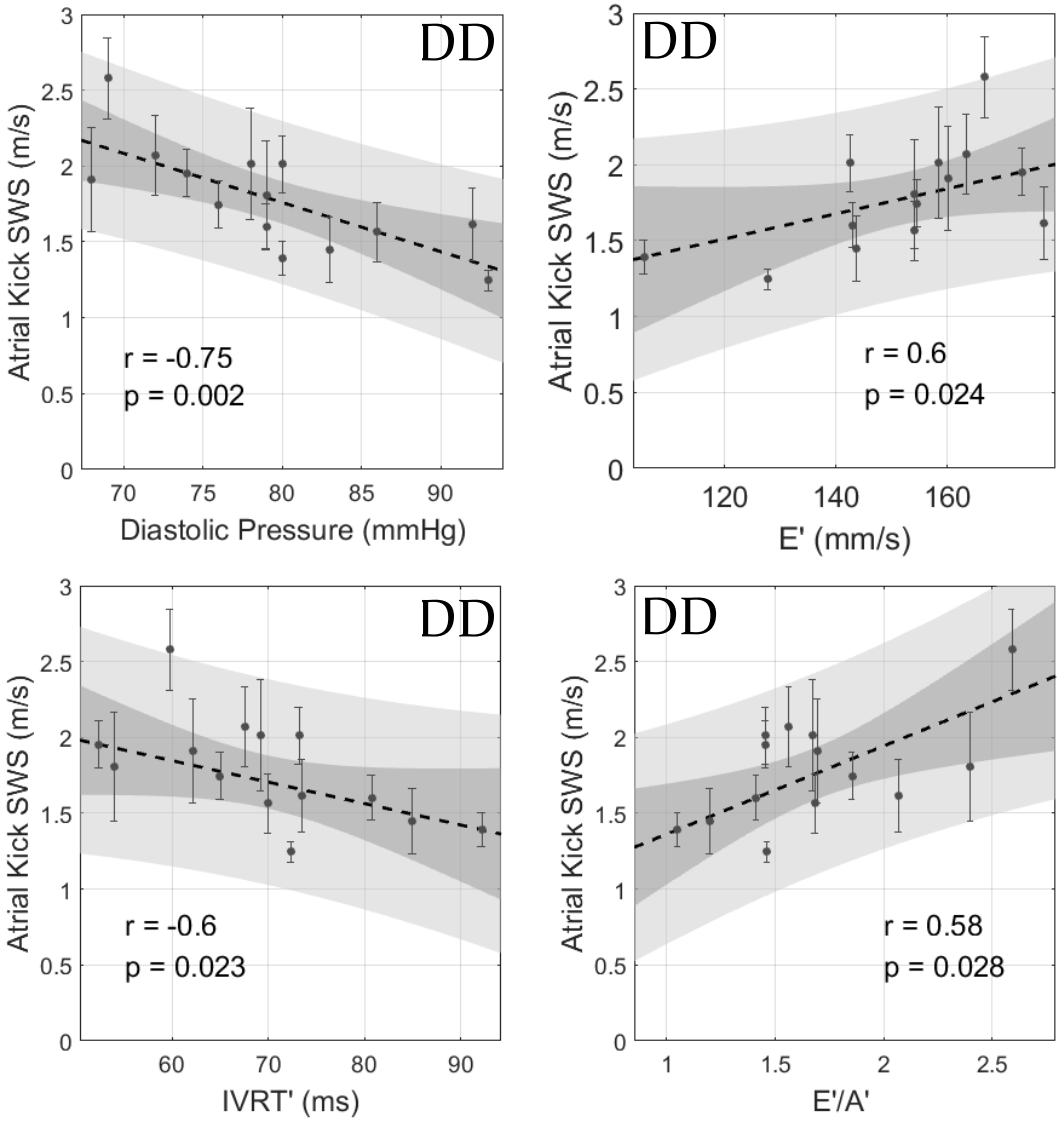

Figure 4.18 Atrial Kick SWS plotted against the four statistically significant correlators, (a) systemic diastolic pressure, (b) E', (c) IVRT', and (d) E'/A'. Markers and error bars represent the mean and standard deviation of the atrial kick SWS for each subject. The black dashed line represents the linear regression where the r and p-values were estimated. The dark gray band represents the 95% confidence interval of the linear regression and the light gray band represents the 95% observation prediction interval. The "DD" markers indicate where diastolic dysfunction is more likely to occur.

4.3.1. Intra- and Inter-rater Variability

Table 4.3 shows the results from the intra- and inter-rater repeatability test and Figure 4.19 shows a visualization of these results. A single SWS measurement from different readers had a slightly higher correlation coefficient then the when the same reader measured the SWS. However, the MAE, measuring the average difference of the paired SWS measurements was lower when the same reader estimated the SWS. There was no statistically significant difference between the intra-rater and inter-rater SWS measurements for both a single estimate or the per subject estimate.

Table 4.3 Intra- and Inter-rater Correlations

	SWS Estimate	***Corr. Coef. (r)***	***MAE (m/s)***
Intra-rater	Single SWS Estimate	0.80	0.16
	Per-subject SWS	0.85	0.13
Inter-rater	Single SWS Estimate	0.82	0.18
	Per-subject SWS	0.90	0.11

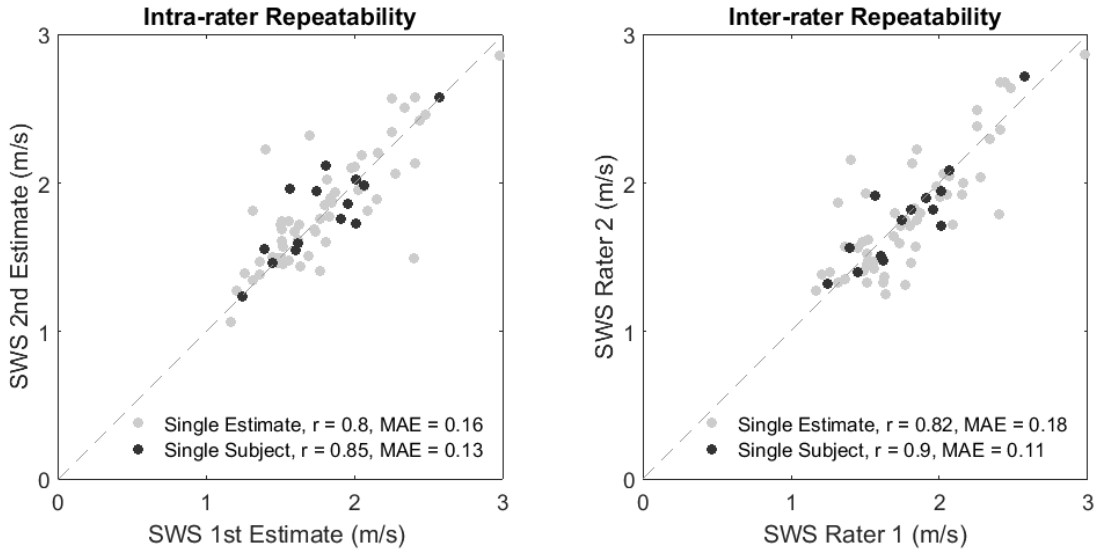

Figure 4.19 The intra- and inter-rater repeatability of the SWS estimate. The light gray dots indicate the SWS measurement from a single data acquisition. The dark gray dots indicate the average SWS measurement for a single participant. r indicates the correlations between the measurements and MAE is the mean absolute error.

4.4. Discussion and Conclusion

This study is the first to use ultrafast ultrasound imaging to estimate the atrial kick SWS on humans. This is because in diverging wave imaging the frame rate and field of view are inherently high. This not only allows the imaging of multiple regions of the heart in the apical view, but also allows for the imaging of the atrial kick shear wave from the parasternal long axis view where the tissue is oriented longitudinally across the imaging region. The parasternal long axis view is seen in Figure 4.20. Further, because the parasternal view is oriented perpendicular to the apical view, the orthogonal components of the shear wave can be evaluated. Because the SWS differs when propagating across or through the myocardial fibers, the different shear wave components are expected to have

different speeds (Couade et al. 2011; Song et al. 2015; Song et al. 2016a). Future studies will determine if the imaging view has a statistically significant impact of the estimated SWS.

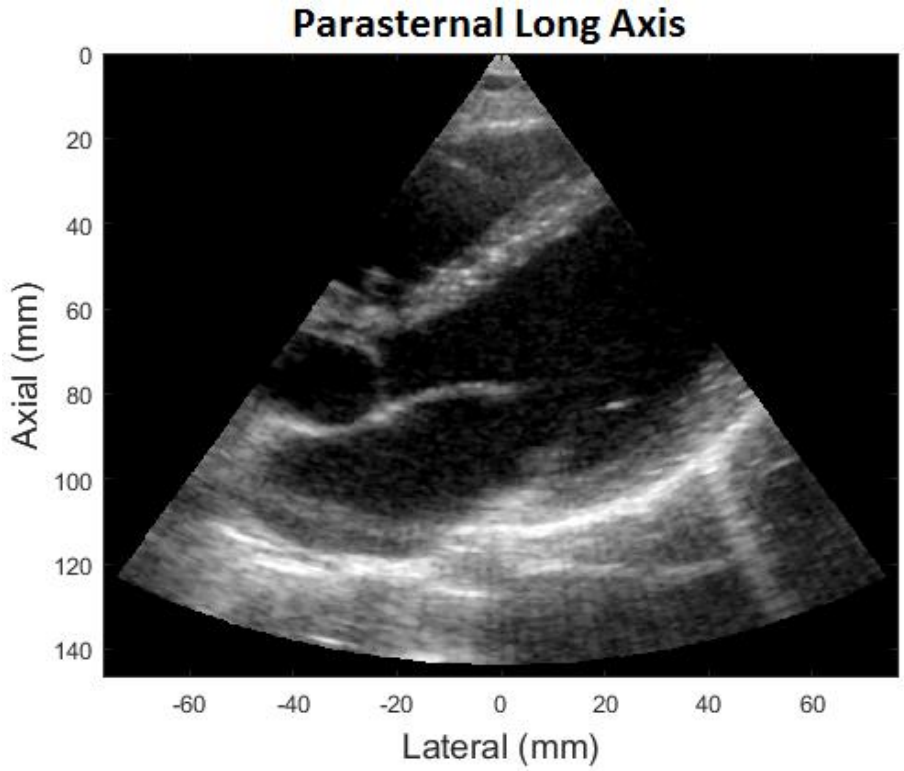

Figure 4.20 Parasternal long axis view of the heart.

4.4.1. Classification of the Atrial Kick Shear Wave

Previous cardiac SWE studies relied on the ARF for the generation of the shear wave (Pernot et al. 2011). Because the transducer controls this form of shear wave generation, the classification of the wave is well known. In contrast, the study here utilizes the transient force of the atrial kick as a mechanical stimulus to generate the shear wave. This occurs naturally in every heart cycle. In this way the atrial kick shear wave acts much like the shear wave generated during transient

elastography (Sandrin et al. 1999; Sandrin et al. 2002b; Sandrin et al. 2003). This wave may be represented as a longitudinal shear wave rather than a transverse shear wave (Catheline and Benech 2015). However, because the wave is generated naturally within the heart and not controlled from the transducer, the classification of the wave is unknown and need further study.

Other methods in SWE report either the SWS (c_S) or the shear modulus (μ) as a measure of tissue stiffness. The equation relating shear modulus to the SWS is $\mu = \rho c_s^2$, where (ρ) is the density of the tissue under investigation. Because the classification of the wave is unknown, and the shear wave movement may be influenced by chamber size, the wall thicknesses, the orientation of myocardial fibers, and the viscoelastic properties of the myocardium, this research only reports the atrial kick SWS. A definitive mathematical model relating SWS to cardiac shear modulus is needed before the atrial kick shear wave can be used to estimate the shear modulus. These models will need to be developed in future research.

Currently the measurement of the atrial kick SWS is a global measurement designed for assessment of LV function and stiffness. The contribution of the RV is discounted. With improved modeling of the wave propagation, the separation and investigation of both sides of the heart will help provide clinicians with accurate information about the progression of diastolic function throughout the heart.

4.4.2. Positive Correlation of the SWS to Measures of Diastolic Function

Significant correlators to the atrial kick SWS were the E', E'/A', IVRT', and systemic diastolic pressure. For each, it was seen that the SWS was positively correlated to the other measures of diastolic function. This is the opposite of what was originally expected. This is because diastolic function is related to myocardial stiffness; thus, as stiffness increases the diastolic function is expected to be reduced. In conventional SWE, as stiffness increases the SWS also increases. Thus, we would expect the SWS to increase when the other measures show diastolic function decreasing. Reasons for the positive correlation are unknown and need further study. Measurement of the atrial kick SWS in conjunction with cardiac catheter derived measured of chamber pressure may help to determine the correlations seen here.

E' and A' are respectively the peak tissue velocities for the early and late portions of the diastolic phase of the heart cycle. The E'/A' ratio is a common measure of ventricular filling and reflects diastolic function because as myocardial stiffness increases, early filling is ineffective and late filling must compensate more to adequately fill the left LV. Because there was no significant correlation between A' and the atrial kick SWS, this suggests the SWS does not depend on the magnitude of the initial pulse generating the wave (within normal physiological limits). Because E' was correlated to the SWS while A' was not, the correlation with E'/A' may only reflect the correlation to E'.

IVRT' is defined as the time between the closing of the aortic valve and the opening of the mitral valve, where the opening and closing of valves is regulated by chamber pressures. During this time, the LV begins to relax following the systolic contraction of the myocardium. The relaxation expands the LV chamber which causes the LV chamber pressure to fall. The end of the isovolumetric relaxation is at the time of mitral valve opening, which occurs when the LV chamber pressure falls below the LA chamber pressure. If relaxation is impaired, or the myocardium is stiffer, the natural reduction of LV pressure is slowed and IVRT' increased.

All significant correlations between the atrial kick SWS and the other health measures were related to current measures of cardiac function and were found in a healthy population. This suggests that the SWS, which has previously been shown to be influenced by ventricular loading and myocardial mechanical properties (Pislaru et al. 2014), has an underlying relationship to cardiac function in the absence of disease. Because of this, other factors may be needed to better assess the deviations of the atrial kick SWS caused by disease, and a single measurement of the SWS may not be enough to assess disease progression. To account for the deviation in the SWS measurement in a healthy population, the SWS may be reported along with a z-score. The z-score indicates the difference of the measurement from the population mean when normalized to standard deviation (Colan 2013). Z-scores allow for a simple clinical interpretation of abnormalities and are commonly reported in clinical practice for patient assessment (Lopez et al. 2010).

4.4.3. Limitations

As seen in Figure 4.21, E'-A' fusion can be a cause of an unsuccessful estimate of SWS. This further shows that other physiological factors affect the generation or visualization of the atrial kick shear wave. In subject two, the shear wave was well detected on days 1 and 3; however, because of an increased heart rate reducing the length of diastole the shear wave was not visualized. Other potential causes for an unsuccessful estimate of the SWS may be because of disease directly affecting atrial contraction such as atrial fibrillation.

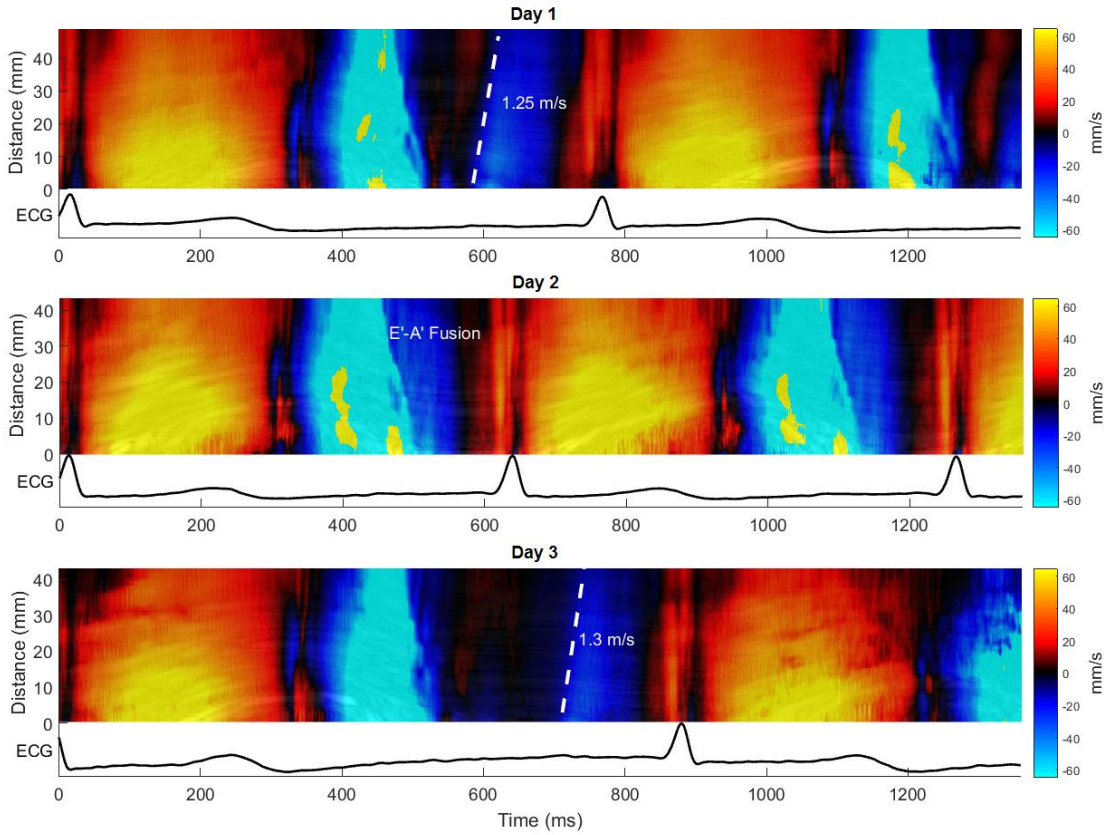

Figure 4.21 Tissue velocity along the IVS for a subject 3. E'-A' fusion occurred on day two and no SWS estimate was possible.

When comparing the SWS against other measures of diastolic function, measurements such as ejection fraction (EF), septal thickness, and other baseline measurements for cardiac chamber quantification were not estimated. Because these measurements are also used in the assessment of cardiac structure and function when designing an intervention plan for a patient with disease, Future research will need to relate these baseline measurements to the SWS. This will need to be performed on both a healthy and symptomatic population.

Chapter 5.

Discussion and Summary

5.1. Introduction

This Chapter provides an overview of the research performed and presented in this dissertation and future directions of this research are provided.

5.2. Summary

5.2.1. Validation of Shear Wave Elastography

The development of a method used to estimate SWS in ultrasound based SWE and a validation of methods used in SWE was presented in Chapter 3. The SWS was estimated from the ratio of 1st order spatial and temporal derivatives of the shear wave tissue velocity signal. Where the shear wave was generated by mechanical excitation on the surface of a tissue mimicking gelatin phantom. The method for SWS estimation was validated on three phantoms of differing stiffness and compared to three other methods used in SWS estimation (a 2nd order wave equation, a 2-D TTP method, and a 2-D CC method). The Young's modulus of each phantom was measured using a destructive mechanical testing; then, from the equations defined in Chapter 2 the nominal SWS was estimated compared to the ultrasound measured SWS. All ultrasound based methods were shown to provide a similar SWS estimation to the nominal SWS. This research also investigated the ability of the four methods of SWS estimation to resolve a hard inclusion placed in

a soft background of a tissue mimicking phantom. Each method was capable of imaging the inclusion using the same shear wave data.

5.2.2. Cardiac Atrial Kick Shear Wave Elastography

The researched performed in the development of Cardiac Atrial Kick SWE was presented in Chapter 4. This method uses diverging waves to insonify the heart, image the shear wave produced by the atrial kick, and then estimate the SWS. The SWS was estimated from a linear regression along the leading edge of the wave, which was a different method than the one developed and tested in Chapter 3. This wavefront regression based method was chosen because it allowed for the estimation of the SWS from the wavefront without interference from the non-wave-like motion which follows. The atrial kick is the contraction of the LA during late-diastole which allows the LV to more completely fill up with blood. The disturbance caused by atrial contraction propagates up through the LV myocardium. Because the LV myocardium is passive and not contracting at this time the SWS is representative of the passive stiffness of the myocardium. Ultrafast imaging using diverging wave transmits allows the imaging of multiple regions of the heart at once as well as the estimation of SWS from tissues not oriented directly toward the transducer.

An *in vivo* pilot study was performed which estimated the atrial kick SWS in 14 healthy adults. The resulting SWSs were correlated to other measures of health taken in the clinic and were found to be statistically significantly correlated to four

measures of diastolic function, suggesting the atrial kick SWS may also provide a measure of diastolic function. The correlations were positive, where the SWS increased as diastolic function increased. This was opposite than expected and future research is needed to determine the physiological reason for these correlations.

The long-term goal of this research, as stated in Chapter 1, was to develop an ultrasound based elastography method—using the cardiac muscle contraction as the impulse for tissue deformation—to noninvasively assess the *in vivo* stiffness of the heart. Increased stiffness of the heart is associated with the loss of diastolic function which progresses to DHF. Results from the research presented in this dissertation showed that the measurement of a SWS can provide a quantitative and objective measure of the stiffness of tissues. Cardiac Atrial Kick SWE was introduced as a method which measures the SWS and results from this research show it is a promising method for the measurement of diastolic function and myocardial stiffness allowing for improved diagnosis and improved care of those suffering from DD and DHF.

5.3. Future Directions

5.3.1. Interleaved PI and Fundamental Tissue Velocity Estimation

Future directions of this research will compare PI imaging and fundamental imaging for tissue velocity estimation with varying number of ultrasound transmits and transmit profiles. Because PI imaging uses consecutive transmits at opposite polarity, but the same transmit profile, the number of angles to be used

for coherent summation is reduced by a factor of two when compared to fundamental imaging. The question which will be answered by performing this research is: when imaging using weakly focused transmit beams—which have a poor 2nd harmonic generation—is it better to use the fundamental frequency for tissue velocity estimation with N coherently summed data frames, or PI for tissue velocity estimation with N/2 coherently summed data frames?

To answer this question, multiple imaging sequences will be interleaved to provide a direct comparison of the methods under the same *in vivo* imaging conditions. These sequences will consist of **1)** conventional fundamental transmits, **2)** PI transmits, **3)** multiplane wave techniques for the fundamental frequency (Tiran et al. 2015) and **4)** multiplane wave techniques for the 2nd harmonic (Gong et al. 2017). Figure 5.1 shows the interleaved data collection sequence to be used for future research. The data collection sequence was designed to keep tissue velocity estimation parameters the same for both methods. The parameters to be kept the same are **1)** the number of transmits per IQ data frame, **2)** the PRF, and **3)** the receive demodulation frequency. The sequence shown is for a comparison of fundamental and PI tissue velocity imaging when using two transmits per IQ data frame. The PI sequence has consecutive transmits at opposite polarities but all images are taken from the same angle and no coherent summation can be used. The fundamental sequence uses coherent compounding and collects data by imaging at two separate angles. To ensure tissue velocity images are interleaved, rather than simply IQ data frames, the sequence is designed to interleave two IQ

data images for each method (1, 1, 2, 2, 1, 1, …). The tissue velocity is estimated from these data frames using phase based techniques. The PI sequence used a transmit frequency half that of the fundamental to keep the demodulation frequency the same. This is because PI used the 2nd harmonic while fundamental uses the 1st. In this way, the PRF and Nyquist velocity are similar for both methods and to a non-interleaved sequence.

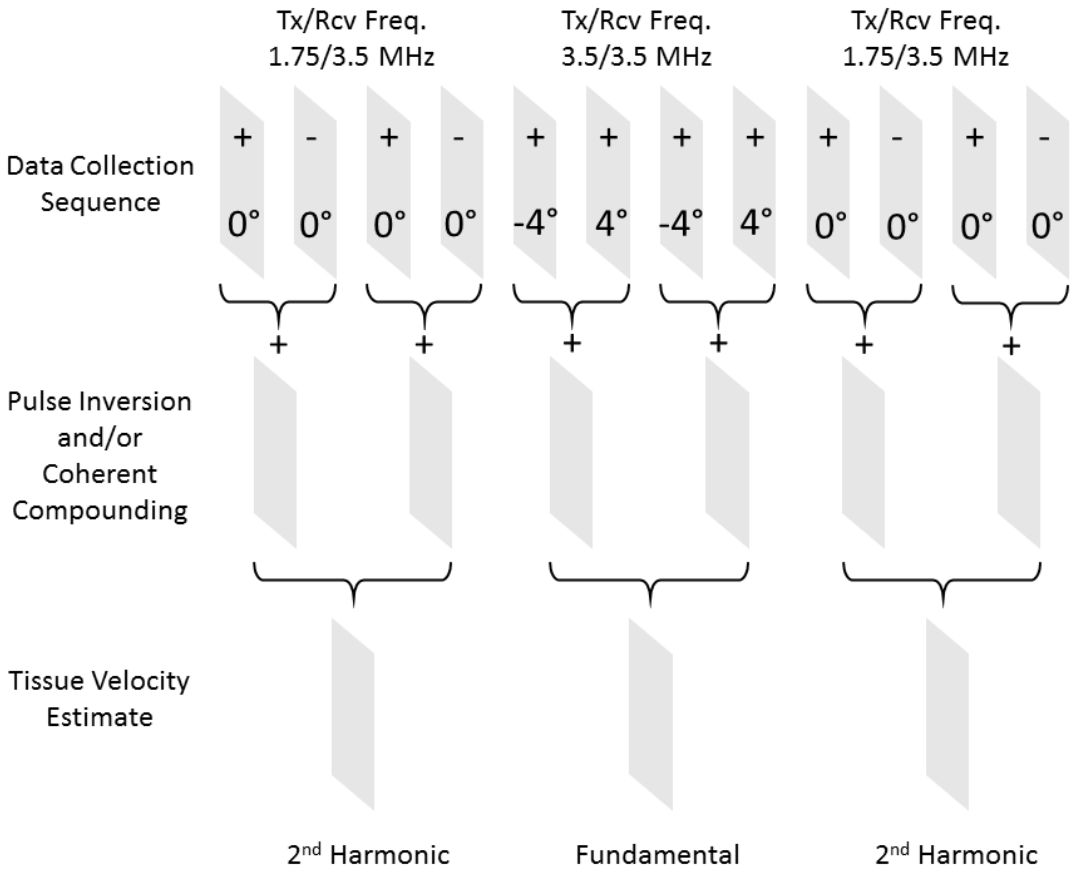

Figure 5.1 Method of data collection for interleaving PI and fundamental tissue velocity images. The PI sequence changes polarity of a 1.75 MHz transmit pulse and receives at a frequency of 3.5 MHz. The fundamental sequence changes imaging angle, transmits and receives at a frequency of 3.5 MHz.

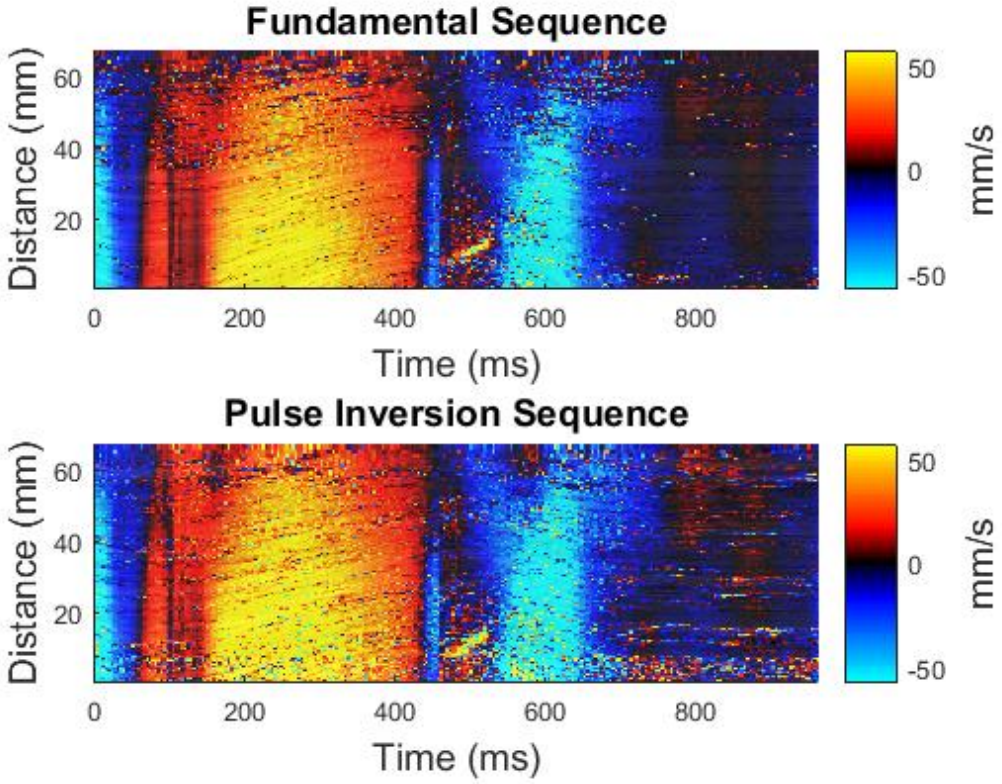

Figure 5.2 Tissue velocity reconstructed along a line through the IVS for the interleaved fundamental and PI imaging sequences. No spatial averaging or median filtering was performed.

Figure 5.2 shows the raw tissue velocity data reconstructed along a line through the IVS when a total of four ultrasound transmits were used to reconstruct a single IQ data image. With four transmits a total of two angles of the PI sequence and four angles for fundamental sequence were used to image the tissue and then estimate its velocity. No spatial or temporal filtering has been performed. The PI sequence shows a visibly higher noise content than the fundamental sequence.

Figure 5.3 shows the mean and standard deviation of the tissue velocity taken from a 9x9 block of pixels in the center of the IVS. Here, the PI derived tissue velocity estimate also shows a visibly higher standard deviation than the fundamental. These suggest that when estimating tissue velocity in SWE methods, PI may not always provide the optimal SNR. The diverging waves used here may have not generated high enough 2nd harmonics signal to provide an improvement. Future research will use the interleaved method presented here to investigate how varying the number of coherently compounded angles and transmit profiles affects the SNR of the tissue velocity measurement.

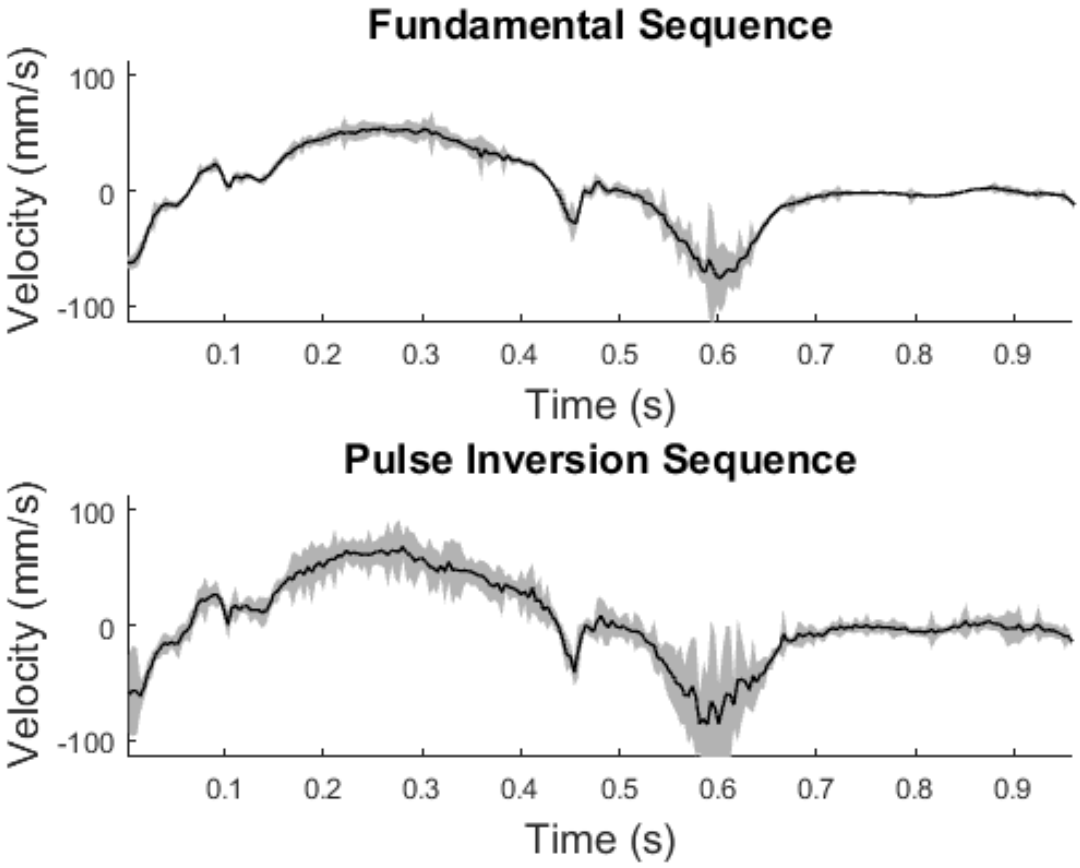

Figure 5.3 Tissue velocity from a 9x9 block of pixels at a single point in the IVS from the interleaved fundamental and PI imaging sequences. The black line represents the mean of the block and the gray the standard deviation. The fundamental sequence shows less standard deviation then the PI method.

5.3.2. Estimation of Atrial Stiffness

The long-term goal of this research is to develop a cardiac SWE method which estimates SWS from naturally occurring shear waves in the heart. This includes the estimation of wave speeds from valve closure as well as the atrial kick shear wave. Future research will estimate the SWS of the mitral valve induced shear wave in the atria. At end diastole, the mitral valve is forced closed by the increased pressure in the LV. As the mitral valve closes a shear wave propagates away from the mitral annulus and through the myocardium of both the ventricles and atria. Because the ventricles are beginning to actively contract, the SWS is a combination of their passive stiffness and their contractile state. In contrast, because the atria have finished contracting the resulting shear wave propagates through a passive atria; thus, the SWS represents its passive stiffness.

Figure 5.4 shows the tissue velocity reconstructed along the LA (0-25 mm) and LV (25-80 mm) free walls. The mitral valve closes around 100 ms after the start of data collection. At this time, the shear wave propagates up through the LV and down through the LA. The SWS in the LA was at 1.06 m/s while in the LV it was 5.33 m/s. Future research will investigate the SWS through the LA, compare it to the SWS through the IVS, and investigate its relationship to the myocardial stiffness of the LA.

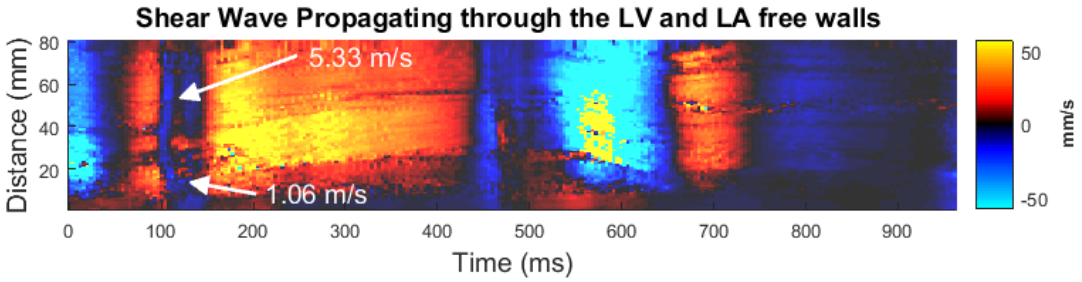

Figure 5.4 Tissue velocity reconstructed along the LA free wall (0-25 mm) and the LV free wall (25-80 mm). The Mitral valve closes around 100 ms and a shear wave propagates up through the LV and down through the LA. The LV SWS was 5.33 m/s and the LA SWS was 1.06 m/s.

5.4. Contributions

Peer-reviewed Journal Articles

[1] **Engel AJ**, Bashford GR, "A New Method for Shear Wave Speed Estimation in Shear Wave Elastography," *IEEE Transactions on Ultrasonics, Ferroelectrics, and Frequency Control*, vol. 62, no. 12, pp. 2106-2114, 2015. doi:10.1109/TUFFC.2015.007282

Conference Proceedings

[1] **Engel AJ**, Hsu HH, Song P, Bashford GR, "Cardiac Atrial Kick Shear Wave Elastography with Ultrafast Diverging Wave Imaging: An *In Vivo* Pilot Study," IEEE IUS, Washington, D.C., September. 2017.

[2] **Engel AJ**, Bashford GR, "Enabling Real-Time Ultrasound Imaging of Soft Tissue Mechanical Properties by Simplification of the Shear Wave Motion Equation," IEEE EMBS, Milan, Italy, Aug. 2015. doi:10.1109/EMBC.2015.7319229

Conference Abstracts

[1] **Engel AJ**, Hsu HH, Song P, Bashford GR, "Cardiac Atrial Kick Shear Wave Elastography with Ultrafast Diverging Wave Imaging: An *In Vivo* Pilot Study," IEEE IUS, Washington, DC, September. 2017.

[2] **Engel AJ**, Bashford GR, "Myocardial Elasticity Measurement via high Frame Rate Ultrasound Tissue Doppler Imaging," BMES, Minneapolis, Minnesota, Oct. 2016.

Bibliography

Abhayaratna WP, Marwick TH, Smith WT, Becker NG. Characteristics of left ventricular diastolic dysfunction in the community: an echocardiographic survey. Heart 2006;92:1259–1264. Available from: http://heart.bmj.com/content/92/9/1259

Allen TH, Krzywicki HJ, Roberts JE. Density, fat, water and solids in freshly isolated tissues. J Appl Physiol 1959a;14:1005–1008. Available from: http://www.dtic.mil/dtic/tr/fulltext/u2/238727.pdf

Allen TH, Welch BE, Trujillo TT, Roberts JE. Fat, water and tissue solids of the whole body less its bone mineral. J Appl Physiol 1959b;14:1009–1012. Available from: http://www.dtic.mil/dtic/tr/fulltext/u2/238727.pdf

Apostolakis IZ, Nandlall SD, Konofagou EE. Piecewise Pulse Wave Imaging (pPWI) for detection and monitoring of focal vascular disease in murine aortas and carotids in vivo. IEEE Trans Med Imaging 2016;35:13–28. Available from: http://www.ncbi.nlm.nih.gov/pubmed/26168432

Asher CR, Klein AL. Diastolic Heart Failure: Restrictive Cardiomyopathy, Constrictive Pericarditis, and Cardiac Tamponade: Clinical and Echocardiographic Evaluation. Cardiol Rev 2002;10:218–229.

Barr RG, Nakashima K, Amy D, Cosgrove D, Farrokh A, Schafer F, Bamber JC, Castera L, Choi BI, Chou Y-H, Dietrich CF, Ding H, Ferraioli G, Filice C, Friedrich-Rust M, Hall TJ, Nightingale KR, Palmeri ML, Shiina T, Suzuki S, Sporea I, Wilson S, Kudo M. WFUMB Guidelines and Recommendations for Clinical Use of Ultrasound Elastography: Part 2: Breast. Ultrasound Med Biol 2015;41:1148–1160. Available from: http://dx.doi.org/10.1016/j.ultrasmedbio.2015.03.008%0AWFUMB

Benjamin EJ, Blaha MJ, Chiuve SE, Cushman M, Das SR, Deo R, de Ferranti SD, Floyd J, Fornage M, Gillespie C, Isasi CR, Jiménez MC, Jordan LC, Judd SE, Lackland D, Lichtman JH, Lisabeth L, Liu S, Longenecker CT, Mackey RH, Matsushita K, Mozaffarian D, Mussolino ME, Nasir K, Neumar RW, Palaniappan L, Pandey DK, Thiagarajan RR, Reeves MJ, Ritchey M, Rodriguez CJ, Roth GA, Rosamond WD, Sasson C, Towfighi A, Tsao CW, Turner MB, Virani SS, Voeks JH, Willey JZ, Wilkins JT, Wu JH, Alger HM, Wong SS, Muntner P. Heart Disease and Stroke Statistics—2017 Update: A Report From the American Heart Association. Circulation. 2017. Available from: http://circ.ahajournals.org/content/early/2017/01/25/CIR.0000000000000485

Bercoff J, Tanter M, Fink M. Supersonic Shear Imaging : A New Technique for Soft Tissue Elasticity Mapping. IEEE Trans Ultrason Ferroelectr Freq Control 2004;51:396–409. Available from: ieeexplore.ieee.org/iel5/58/29253/01320804.pdf

Berk BC, Fujiwara K, Lehoux S. Review series ECM remodeling in hypertensive heart disease. J Clin Invest 2007;117:568–575. Available from: https://www.ncbi.nlm.nih.gov/pubmed/17332884

Bernal M, Nenadic I, Urban MW, Greenleaf JF. Material property estimation for tubes and arteries using ultrasound radiation force and analysis of propagating modes. J Acoust Soc Am 2011;129:1344–1354. Available from: https://www.ncbi.nlm.nih.gov/pubmed/21428498

Bernardo BC, Weeks KL, Pretorius L, McMullen JR. Molecular distinction between physiological and pathological cardiac hypertrophy: Experimental findings and therapeutic strategies. Pharmacol Ther Elsevier Inc., 2010;128:191–227. Available from: http://dx.doi.org/10.1016/j.pharmthera.2010.04.005

Bonow RO, Bacharach SL, Green M V, Kent KM, Rosing DR, Lipson LC, Leon MB, Epstein SE. Impaired left ventricular diastolic filling in patients with coronary artery disease: assessment with radionuclide angiography. Circulation 1981;64:315–23. Available from: http://www.embase.com/search/results?subaction=viewrecord&from=export&id=L25047231%5Cnhttp://sfx.aub.aau.dk/sfxaub?sid=EMBASE&issn=01615505&id=doi:&atitle=Impaired+left+ventricular+diastolic+filling+in+patients+with+acromegaly:+Assessment+with+radionuclid

Brum J, Bernal M, Gennisson JL, Tanter M. In vivo evaluation of the elastic anisotropy of the human Achilles tendon using shear wave dispersion analysis. Phys Med Biol 2014 [cited 2014 Apr 29];59:505–23. Available from: http://www.ncbi.nlm.nih.gov/pubmed/24434420

Catheline S, Benech N. Longitudinal shear wave and transverse dilatational wave in solids. J Acoust Soc Am 2015;137:El200-EL205. Available from: http://dx.doi.org/10.1121/1.4907742

Catheline S, Wu F, Fink M. A solution to diffraction biases in sonoelasticity: the acoustic impulse technique. J Acoust Soc Am 1999;105:2941–2950. Available from: http://asa.scitation.org/doi/10.1121/1.426907

Chen S, Urban MW, Pislaru C, Kinnick R, Zheng Y, Yao A, Greenleaf JF. Shearwave Dispersion Ultrasound Vibrometry (SDUV) for Measuring Tissue Elasticity and Viscosity. 2009;56:55–62. Available from: https://www.ncbi.nlm.nih.gov/pubmed/19213632

Cohn JN, Ferrari R, Sharpe N. Cardiac remodeling - concepts and clinical implications: a consensus paper from an international forum on cardiac remodeling. Behalf of an International Forum on Cardiac Remodeling. J Am Coll Cardiol 2000;35:569–582. Available from: http://dx.doi.org/10.1016/S0735-1097(99)00630-0

Colan SD. The why and how of Z scores. J Am Soc Echocardiogr 2013;26:38–40. Available from: http://www.onlinejase.com/article/S0894-7317(12)00879-6/fulltext

Cortes DH, Suydam SM, Silbernagel KG, Thomas S, Elliott DM. Continuous Shear Wave Elastography: a New Method to Measure in-vivo Viscoelastic Properties of Tendons. Ultrasound Med Biol 2016;41:1518–1529. Available from: https://www.ncbi.nlm.nih.gov/pubmed/25796414

Costet A, Provost J, Gambhir A, Bobkov Y, Danilo P, Boink GJJ, Rosen MR, Konofagou EE. Electromechanical wave imaging of biologically and electrically paced canine hearts invivo. Ultrasound Med Biol 2014;40:177–187.

Couade M, Pernot M, Messas E, Bel A, Ba M, Hagege A, Fink M, Tanter M. In Vivo quantitative mapping of myocardial stiffening and transmural anisotropy during the cardiac cycle. IEEE Trans Med Imaging 2011;30:295–305. Available from: http://ieeexplore.ieee.org/document/5575428/

Daigle RE. Ultrasound Imaging System with Pixel Oriented Processing. 2009.

Deffieux T, Gennisson J-L, Larrat B, Fink M, Tanter M. The variance of quantitative estimates in shear wave imaging: theory and experiments. IEEE Trans Ultrason Ferroelectr Freq Control 2012;59:2390–410. Available from: http://www.ncbi.nlm.nih.gov/pubmed/23192803

Deffieux T, Gennisson J, Bercoff J, Tanter M. On the Effects of Reflected Waves in Transient Shear Wave Elastography. IEEE Trans Ultrason Ferroelectr Freq Control Ieee, 2011;58:2032–2035. Available from: https://www.institut-langevin.espci.fr/IMG/pdf/2011_on_the_effects_of_reflected_waves_in_transient_shear_wave_elastography.pdf

Diamond JA, Phillips RA. Hypertensive heart disease. Hypertens Res 2005;28:191–202. Available from: https://www.nature.com/hr/journal/v28/n3/pdf/hr200525a.pdf

Doherty JR, Dahl JJ, Trahey GE. Harmonic tracking of acoustic radiation force-induced displacements. IEEE Trans Ultrason Ferroelectr Freq Control 2013;60:2347–2358. Available from: https://www.ncbi.nlm.nih.gov/pmc/articles/PMC3974334/

Donald I, MacVicar J, Brown TG. Investigation of Abdominal Masses by Pulsed Ultrasound. Lancet 1958;271:1188–1194.

Dubin D. Rapid Interpretation of EKG's. 6th ed. USA: Cover Publishing Company, 1996.

Duck FA. Nonlinear acoustics in diagnostic ultrasound. Ultrasound Med Biol 2002;28:1–18. Available from: http://www.umbjournal.org/article/S0301-5629(01)00463-X/abstract

Eby SF, Song P, Chen S, Chen Q, Greenleaf JF, An KN. Validation of shear wave elastography in skeletal muscle. J Biomech Elsevier, 2013 [cited 2014 Apr 29];46:2381–2387. Available from: http://www.ncbi.nlm.nih.gov/pubmed/23953670

Edler I, Lindström K. The history of echocardiography. Ultrasound Med Biol 2004;30:1565–1644. Available from: http://www.umbjournal.org/article/S0301-5629(99)00056-3/pdf

Elgeti T, Beling M, Hamm B, Braun J, Sack I. Cardiac Magnetic Resonance Elastography: toward the diagnosis of abnormal myocardial relaxation. Invest Radiol 2010;45:782–787.

Elgeti T, Knebel F, Hättasch R, Hamm B, Braun J, Sack I. Shear-wave Amplitudes Measured with Cardiac MR Elastography for Diagnosis of Diastolic Dysfunction.

Radiology 2014;271:681–687. Available from: https://doi.org/10.1148/radiol.13131605

Elzinga G, Westerhof N. Pressure and flow generated by the left ventricle against different impedances. Circ Res 1973;32:178–186. Available from: http://circres.ahajournals.org/content/circresaha/32/2/178.full.pdf

Evans A, Whelehan P, Thomson K, McLean D, Brauer K, Purdie C, Jordan L, Baker L, Thompson A. Quantitative shear wave ultrasound elastography: initial experience in solid breast masses. Breast Cancer Res 2010;12:R104. Available from: http://breast-cancer-research.biomedcentral.com/articles/10.1186/bcr2787

Firestone FA. The supersonic Reflectoscope, an instrument for inspecting the interior of solid parts by means of sound waves. J Acoust Soc Am 1946;17:287–299. Available from: https://pdfs.semanticscholar.org/0bf7/4a61b8229b12dc61ce5f39ac95d9c1f8c698.pdf

Fisher RA. On the probable error of a coefficient of correlation deduced from a small sample. Metron 1921;1:3–32. Available from: https://hekyll.services.adelaide.edu.au/dspace/bitstream/2440/15169/1/14.pdf

Frank O. On the dynamics of cardiac muscle. Am Heart J 1959;58:467–478.

Gaasch WH, Zile MR. Left ventricular diastolic dysfunction and diastolic heart failure. Annu Rev Med 2004;55:373–394. Available from: http://www.annualreviews.org/doi/pdf/10.1146/annurev.med.55.091902.104417

Geliko. The Proper Dissolution of Gelatin. 2008.

Gennisson J-L, Catheline S, Chaffaï S, Fink M. Transient elastography in anisotropic medium: application to the measurement of slow and fast shear wave speeds in muscles. J Acoust Soc Am 2003;114:536–541. Available from: https://doi.org/10.1121/1.1579008

Gong P, Song P, Chen S. Delay-Encoded Harmonic Imaging (DE-HI) in Multiplane-Wave Compounding. IEEE Trans Med Imaging 2017;36:952–959. Available from: https://doi.org/10.1109/TMI.2016.2638639

Greenleaf JF, Fatemi M, Insana M. Selected methods for imaging elastic properties of biological tissues. Annu Rev Biomed Eng 2003 [cited 2014 May 3];5:57–78. Available from: https://doi.org/10.1146/annurev.bioeng.5.040202.121623

Grossman W, Jones D, McLaurin LP. Wall stress and patterns of hypertrophy in the human left ventricle. J Clin Invest 1975;56:56–64.

Harris FJ. On the use of windows for harmonic analysis with the discrete Fourier transform. Proc IEEE 1978;66:51–83. Available from: http://ieeexplore.ieee.org/lpdocs/epic03/wrapper.htm?arnumber=1455106

Hasegawa H, Kanai H. High-frame-rate echocardiography using diverging transmit beams and parallel receive beamforming. J Med Ultrason 2011;38:129–140.

Haycock GB, Schwartz GJ, Wisotsky DH. Geometric method for measuring body surface area: a height-weight formula validated in infants, children, and adults. J Pediatr 1978;93:62–66.

Heidenreich PA, Albert NM, Allen LA, Bluemke DA, Butler J, Fonarow GC, Ikonomidis JS, Khavjou O, Konstam MA, Maddox TM, Nichol G, Pham M, Piña IL, Trogdon JG. Forecasting the impact of heart failure in the united states a policy statement from the american heart association. Circ Hear Fail 2013;6:606–619.

Heron M. Deaths: Leading Causes for 2014. Natl Vital Stat Rep 2016;65:1–96. Available from: http://www.ncbi.nlm.nih.gov/pubmed/27376998

Jessup M, Brozena S. Heart Failure. N Engl J Med 2003;26:2007–2018.

Kanai H. Propagation of spontaneously actuated pulsive vibration in human heart wall and in vivo viscoelasticity estimation. IEEE Trans Ultrason Ferroelectr Freq Control 2005;52:1931–1942.

Kasai C, Namekawa K, Koyano A, Omoto R. Real-Time Two-Dimensional Blood Flow Imaging Using an Autocorrelation Technique. IEEE Trans Sonics Ultrason 1985;32:458–464.

Katz AM, Katz PB. Diseases of the heart in the works of Hippocrates. Br Heart J 1962;24:257–64. Available from: http://www.pubmedcentral.nih.gov/articlerender.fcgi?artid=1017881&tool=pmcentrez&rendertype=abstract

Kinsler LE, Frey AR, Coppens AB, Sanders J V. Fundamentals of Acoustics. 4th ed. John Wiley & Sons, Inc., 1999.

Konofagou E, Lee W-N, Luo J, Provost J, Vappou J. Physiologic cardiovascular strain and intrinsic wave imaging. Annu. Rev. Biomed. Eng. 2011. Available from: http://www.ncbi.nlm.nih.gov/pubmed/21756144

Konofagou EE, Provost J. Electromechanical wave imaging for noninvasive mapping of the 3D electrical activation sequence in canines and humans in vivo. J Biomech Elsevier, 2012;45:856–864. Available from: http://dx.doi.org/10.1016/j.jbiomech.2011.11.027

Kornbluth M, Liang DH, Paloma A, Schnittger I. Native Tissue Harmonic Imaging Improves Endocardial Border Definition and Visualization of Cardiac StructuresNo Title. J Am Soc Echocardiogr 1998;11:693–701.

Krumm J. Savitzky-Golay Filters for 2D Images. Microsoft Res. 2001. Available from: www.research.microsoft.com/users/jckrumm/SavGol/SavGol.htm

Kruse SA, Rose GH, Glaser KJ, Manduca A, Felmlee JP, Jr. CRJ, Ehman RL. Magnetic Resonance Elastography of the Brain. Neuroimage 2008;39:231–237.

Kuznetsova T, Herbots L, López B, Jin Y, Richart T, Thijs L, González A, Herregods MC, Fagard RH, Díez J, Staessen JA. Prevalence of left ventricular diastolic dysfunction in

a general population. Circ Hear Fail 2009;2:105–112.

Lopez L, Colan SD, Frommelt PC, Ensing GJ, Kendall K, Younoszai AK, Lai WW, Geva T. Recommendations for Quantification Methods During the Performance of a Pediatric Echocardiogram: A Report From the Pediatric Measurements Writing Group of the American Society of Echocardiography Pediatric and Congenital Heart Disease Council. J Am Soc Echocardiogr Elsevier Inc, 2010;23:465–495. Available from: http://dx.doi.org/10.1016/j.echo.2010.03.019

Loupas T, Powers JT, Gill RW. An Axial Velocity Estimator for Ultrasound Blood Flow Imaging, Based on a Full Evaluation of the Doppler Equation by Means of a Two-Dimensional Autocorrelation Approach. IEEE Trans Ultrason Ferroelectr Freq Control 1995;42:672–688.

Maksuti E, Widman E, Larsson D, Urban MW, Larsson M, Bjällmark A. Arterial Stiffness Estimation by Shear Wave Elastography: Validation in Phantoms with Mechanical Testing. Ultrasound Med Biol 2015;42:308–321.

Mandinov L, Eberli FR, Seiler C, Hess OM. Diastolic Heart Failure. Cardiovasc Res 2000;45:813–825.

Manduca A, Lake DS, Kruse SA, Ehman RL. Spatio-temporal directional filtering for improved inversion of MR elastography images. Med Image Anal 2003;7:465–473.

Manduca A, Oliphant TE, Dresner M a., Mahowald JL, Kruse S a., Amromin E, Felmlee JP, Greenleaf JF, Ehman RL. Magnetic resonance elastography: Non-invasive mapping of tissue elasticity. Med Image Anal 2001;5:237–254. Available from: http://linkinghub.elsevier.com/retrieve/pii/S1361841500000396

Mariappan YK, Kolipaka A, Manduca A, Hubmayr RD, Ehman RL, Araoz P, McGee KP. Magnetic resonance Elastography of the Lung parenchyma in an in situ porcine model with a non-invasive mechanical driver: Correlation of Shear Stiffness with Trans-respiratory system Pressures. Magn Reson Med 2012;67:724–732.

Maron BJ. Hypertrophic cardiomyopathy A Systenatic Review. Jouranl Am Med Assoc 2002;287:193–198.

Maron BJ, Ommen SR, Semsarian C, Spirito P, Olivotto I, Maron MS. Hypertrophic cardiomyopathy: Present and future, with translation into contemporary cardiovascular medicine. J Am Coll Cardiol 2014;64:89–99.

Marple SL. Computing the Discrete-Time “Analytic” Signal via FFT. IEEE Trans Signal Process 1999;47:2600–2603.

McLaughlin J, Renzi D. Shear wave speed recovery in transient elastography and supersonic imaging using propagating fronts. Inverse Probl 2006 [cited 2014 Dec 4];22:681–706. Available from: http://stacks.iop.org/0266-5611/22/i=2/a=018?key=crossref.e92b3a3f702b6a11355102ec38e53756

McMurray JJV, Adamopoulos S, Anker SD, Auricchio A, Böhm M, Dickstein K, Falk V,

Filippatos G, Fonseca C, Gomez-Sanchez MA, Jaarsma T, Kober L, Lip GYH, Maggioni A Pietro, Parkhomenko A, Pieske BM, Popescu BA, Ronnevik PK, Rutten FH, Schwitter J, Seferovic P, Stepinska J, Trindade PT, Voors AA, Zannad F, Zeiher A, Bax JJ, Baumgartner H, Ceconi C, Dean V, Deaton C, Fagard R, Funck-Brentano C, Hasdai D, Hoes A, Kirchhof P, Knuuti J, Kolh P, Mcdonagh T, Moulin C, Reiner Ž, Sechtem U, Sirnes PA, Tendera M, Torbicki A, Vahanian A, Windecker S, Bonet LA, Avraamides P, Ben Lamin HA, Brignole M, Coca A, Cowburn P, Dargie H, Elliott P, Flachskampf FA, Guida GF, Hardman S, Iung B, Merkely B, Mueller C, Nanas JN, Nielsen OW, Orn S, Parissis JT, Ponikowski P. ESC Guidelines for the diagnosis and treatment of acute and chronic heart failure 2012. Eur J Heart Fail 2012;14:803–869.

Montaldo G, Tanter M, Bercoff J, Benech N, Fink M. Coherent plane-wave compounding for very high frame rate ultrasonography and transient elastography. IEEE Trans Ultrason Ferroelectr Freq Control 2009;56:489–506.

Mosterd A, Deckers JW, Hoes AW, Nederpel A, Smeets A, Linker DT, Grobbee DE. Classification of Heart Failure in Population Based Research : An Assessment of Six Heart Failure Scores. Eur J Epic 1997;13:491–502.

Mozaffarian D, Benjamin EJ, Go AS, Arnett DK, Blaha MJ, Cushman M, Das SR, de Ferranti S, Despres JP, Fullerton HJ, Howard VJ, Huffman MD, Isasi CR, Jim??nez MC, Judd SE, Kissela BM, Lichtman JH, Lisabeth LD, Liu S, Mackey RH, Magid DJ, McGuire DK, Mohler ER, Moy CS, Muntner P, Mussolino ME, Nasir K, Neumar RW, Nichol G, Palaniappan L, Pandey DK, Reeves MJ, Rodriguez CJ, Rosamond W, Sorlie PD, Stein J, Towfighi A, Turan TN, Virani SS, Woo D, Yeh RW, Turner MB. Heart Disease and Stroke Statistics - 2016 Update: A Report From the American Heart Association. Circulation. 2015.

Muthupillai R, Ehman RL. Magnetic Resonance Elastography. Nat Med 1996;2:601–603. Available from: https://www.nature.com/articles/nm0596-601.pdf

Muthupillai R, Lomas JD, Rossman PJ, Greenleaf JF, Manduca A, Ehman RL. Magnetic resonance elastography by direct visualization of propagating acoustic strain waves. Science (80-) 1995;269:1854–1857.

Nagueh SF, Appleton CP, Gillebert TC, Marino PN, Oh JK, Smiseth OA, Waggoner AD, Flachskampf FA, Pellikka PA, Evangelista A. Recommendations for the Evaluation of Left Ventricular Diastolic Function by Echocardiography. J Am Soc Echocardiogr 2009;22:107–133.

Nagueh SF, Smiseth OA, Appleton CP, Benjamin F. Byrd I, Dokainish H, Edvardsen T, Flachskampf FA, Gillebert TC, Klein AL, Lancellotti P, Marino P, Oh JK, Popescu BA, Waggoner AD. Recommendations for the Evaluation of Left Ventricular Diastolic Function by Echocardiography: An Update from the American Society of Echocardiography and the European Association of Cardiovascular Imaging. J Am Soc Echocardiogr Elsevier Inc, 2016;29:277–314. Available from: http://dx.doi.org/10.1016/j.echo.2016.01.011

Nenadic IZ, Urban MW, Mitchell S a, Greenleaf JF. Lamb wave dispersion ultrasound

vibrometry (LDUV) method for quantifying mechanical properties of viscoelastic solids. Phys Med Biol 2011 [cited 2014 May 15];56:2245–2264. Available from: http://www.pubmedcentral.nih.gov/articlerender.fcgi?artid=3086697&tool=pmcentrez&rendertype=abstract

New York Heart Association. Criteria Committee and New York Heart Association. Nomenclature and Criteria for Diagnosis of Diseases of the Heart and Great Vessels. 9th ed. Little, ed. Boston, Mass.: Little & Brown, 1994.

Nichols WW, O'Rurke MF, Vlachopoulos C. McDonald's Blood Flow in Arteries: Theoretical, Experimental and Clinical Principals. 6th ed. London: Hodder Arnold, 2011.

Nightingale K, McAleavey S, Trahey G. Shear-wave generation using acoustic radiation force: in vivo and ex vivo results. Ultrasound Med Biol 2003 [cited 2014 Oct 31];29:1715–1723. Available from: http://linkinghub.elsevier.com/retrieve/pii/S0301562903010809

Nightingale K, Rouze N, Rosenzweig S, Wang M, Abdelmalek M, Guy C, Palmeri M. Derivation and analysis of viscoelastic properties in human liver: Impact of frequency on fibrosis and steatosis staging. IEEE Trans Ultrason Ferroelectr Freq Control 2015;62:165–175.

O'Donnell M, Skovoroda a. R, Shapo BM, Emelianov SY. Internal displacement and strain imaging using ultrasonic speckle\ntracking. IEEE Trans Ultrason Ferroelectr Freq Control 1994;41:314–325.

Oliphant TE, Manduca A, Ehman RL, Greenleaf JF. Complex-Valued Stiffness Reconstruction for Magnetic Resonance Elastography by Algebraic Inversion of the Differential Equation. Magn Reson Med 2001;310:299–310.

Ophir J, Alam SK, Garra BS, Kallel F, Konofagou EE, Krouskop T, Merritt CRB, Righetti R, Souchon R, Srinivasan S, Varghese T. Elastography: Imaging the elastic properties of soft tissues with ultrasound. J Med Ultrason 2002;29:155–171.

Ophir J, Céspedes I, Ponnekanti H, Yazdi Y, Li X. Elastography: A quantitative method for imaging the elasticity of biological tissues. Ultrason Imaging 1991;13:111–134.

Owan T, Hodge D. Trends in prevalence and outcome of heart failure with preserved ejection fraction. N Engl J Med 2006;355:251–259. Available from: http://www.nejm.org/doi/full/10.1056/NEJMoa052256

Palmeri ML, Wang MH, Dahl JJ, Frinkley KD, Nightingale KR. Quantifying Hepatic Shear modulus In Vivo Using Acoustic Radiation Force. Ultrasound Med Biol 2008;34:546–558.

Parfrey PS, Foley RN, Harnett JD, Kent GM, Murray D, Barre PE. Outcome and risk factors of ischemic heart disease in chronic uremia. Kidney Int 1996;49:1428–34. Available from: http://www.ncbi.nlm.nih.gov/pubmed/8731110

Parker KJ, Huang SR, Musulin R a, Lerner RM, Musulin. Tissue Response to Mechanical Vibrations for "Sonoelastic Imaging." Ultrasound Med Biol 1990;16:241–46. Available from: http://osteoporoza-pluskiewicz.pl/dokumenty/2.pdf%5Cnhttp://www.ncbi.nlm.nih.gov/entrez/query.fcgi?cmd=Retrieve&db=PubMed&dopt=Citation&list_uids=2194336

Paulus WJ, Tschöpe C, Sanderson JE, Rusconi C, Flachskampf FA, Rademakers FE, Marino P, Smiseth OA, De Keulenaer G, Leite-Moreira AF, Borbély A, Édes I, Handoko ML, Heymans S, Pezzali N, Pieske B, Dickstein K, Fraser AG, Brutsaert DL. How to diagnose diastolic heart failure: A consensus statement on the diagnosis of heart failure with normal left ventricular ejection fraction by the Heart Failure and Echocardiography Associations of the European Society of Cardiology. Eur Heart J 2007;28:2539–2550.

Peck AL. Aristotle Generation of Animals. Cambridge: Harvard University Press, 1942.

Pernot M, Couade M, Mateo P, Crozatier B, Fischmeister R, Tanter M. Real-time assessment of myocardial contractility using shear wave imaging. J Am Coll Cardiol Elsevier Inc., 2011;58:65–72. Available from: http://dx.doi.org/10.1016/j.jacc.2011.02.042

Pernot M, Fujikura K, Fung-Kee-Fung SD, Konofagou EE. ECG-gated, Mechanical and Electromechanical Wave Imaging of Cardiovascular Tissues In Vivo. Ultrasound Med Biol 2007;33:1075–1085.

Piccolino M. Luigi Galvani and animal electricity: Two centuries after the foundation of electrophysiology. Trends Neurosci 1997;20:443–448.

Pislaru C, Pellikka PA, Pislaru S V. Wave propagation of myocardial stretch: correlation with myocardial stiffness. Basic Res Cardiol 2014;109. Available from: http://link.springer.com/10.1007/s00395-014-0438-5

Pislaru C, Thaden MMAJJ, Pellikka PA, Maurice Enriquez-Sarano SVP. Intrinsic Wave Propagation of Myocardial Stretch, A New Tool to Evaluate Myocardial Stiffness: A Pilot Study in Patients with Aortic Stenosis and Mitral Regurgitation. J Am Soc Echocardiogr 2017;

Poirier P, Bogaty P, Garneau C, Marois L, Dumesnil JG. Diastolic dysfunction in normotensive men with well-controlled type 2 diabetes: Importance of maneuvers in echocardiographic screening for preclinical diabetic cardiomyopathy. Diabetes Care 2001;24:5–10.

Provost J, Gambhir A, Vest J, Garan H, Konofagou EE. A clinical feasibility study of atrial and ventricular electromechanical wave imaging. Hear Rhythm Elsevier, 2013;10:856–862. Available from: http://dx.doi.org/10.1016/j.hrthm.2013.02.028

Provost J, Lee W-N, Fujikura K, Konofagou EE. Imaging the electromechanical activity of the heart in vivo. Proc Natl Acad Sci U S A 2011;108:8565–70. Available from: http://www.pnas.org/content/108/21/8565.long

Ramamurthy BS, Trahey GE. Potential and Limitation of Angle-Independent Flow

Detection Algorithms Using Radio-Frequency And Detected Echo Signals. Ultrason Imaging 1991;268:252–268.

Redfield MM, Jacobsen SJ, Burnett JC, Mahoney DW, Bailey KR, Rodeheffer RJ. Burden of Systolic and Diastolic Ventricular Dysfunction in the Community. Intern Med 2003;289:194–202.

Russo C, Jin Z, Homma S, Rundek T, Elkind MS V, Sacco RL, Di Tullio MR. Effect of obesity and overweight on left ventricular diastolic function: A community-based study in an elderly cohort. J Am Coll Cardiol Elsevier Inc., 2011;57:1368–1374. Available from: http://dx.doi.org/10.1016/j.jacc.2010.10.042

Sandrin L, Catheline S, Tanter M, Hennequin X, Fink M. Time-Resolved Pulsed Elastography with Ultrafast Ultrasonic Imaging. Ultrason Imaging 1999;21:259–272. Available from: http://uix.sagepub.com/content/21/4/259.abstract

Sandrin L, Fourquet B, Hasquenoph J-M, Yon S, Fournier C, Mal F, Christidis C, Ziol M, Poulet B, Kazemi F, Beaugrand M, Palau R. Transient elastography: a new noninvasive method for assessment of hepatic fibrosis. Ultrasound Med Biol 2003;29:1705–1713.

Sandrin L, Tanter M, Catheline S, Fink M. Shear modulus imaging with 2-D transient elastography. IEEE Trans Ultrason Ferroelectr Freq Control 2002a;49:426–435. Available from: http://ieeexplore.ieee.org/lpdocs/epic03/wrapper.htm?arnumber=996560

Sandrin L, Tanter M, Gennisson J-L, Catheline S, Fink M. Shear elasticity probe for soft tissues with 1-D transient elastography. IEEE Trans Ultrason Ferroelectr Freq Control 2002b;49:436–446.

Sarvazyan AP, Rudenko O V, Swanson SD, Fowlkes JB, Emelianov SY. Shear wave elasticity imaging: a new ultrasonic technology of medical diagnostics. Ultrasound Med Biol 1998;24:1419–1435.

Sarvazyan AP, Urban MW, Greenleaf JF. Acoustic Waves in Medical Imaging and Diagnostics. Ultrasound Med Biol 2013 [cited 2014 May 9];39:1133–1146. Available from: http://www.ncbi.nlm.nih.gov/pubmed/23643056

Sasayama S, ROSS J, FRANKLIN D, BLOOR CM, BISHOP S, DILLEY RB. Adaptations of the Left Ventricle to Chronic Pressure Overload. Circ Res 1974;35:64–70. Available from: http://www.embase.com/search/results?subaction=viewrecord&from=export&id=L5091624%5Cnhttp://sfx.library.uu.nl/utrecht?sid=EMBASE&issn=00097330&id=doi:&atitle=Adaptations+of+the+left+ventricle+to+chronic+volume+overload&stitle=CIRC.+RES.&title=Circulation+

Savitzky A, Golay MJE. Smoothing and Differentiation of Data by Simplified Least Squares Procedures. Anal Chem 1964;36:1627–1639.

Scharhag J, Schneider G, Urhausen A, Rochette V, Kramann B, Kindermann W. Athlete's

Heart. J Am Coll Cardiol 2002;40:634–640. Available from: http://linkinghub.elsevier.com/retrieve/pii/S0735109702024786

Shahmirzadi D, Li RX, Konofagou EE. Pulse-Wave Propagation in Straight-Geometry Vessels for Stiffness Estimation: Theory, Simulations, Phantoms and In Vitro Findings. J Biomech Eng 2012;134:114502.

Shiina T, Nightingale KR, Palmeri ML, Hall TJ, Bamber JC, Barr RG, Castera L, Choi BI, Chou Y-H, Cosgrove D, Dietrich CF, Ding H, Amy D, Farrokh A, Ferraioli G, Filice C, Friedrich-Rust M, Nakashima K, Schafer F, Sporea I, Suzuki S, Wilson S, Kudo M. WFUMB guidelines and recommendations for clinical use of ultrasound elastography: Part 1: basic principles and terminology. Ultrasound Med Biol England, 2015;41:1126–1147.

Sluysmans T, Colan SD. Theoretical and empirical derivation of cardiovascular allometric relationships in children. J Appl Physiol 2005;99:445–57. Available from: http://www.ncbi.nlm.nih.gov/pubmed/15557009

Snieder R. Imaging and Averaging in Complex Media. Diffus Waves Complex Media 1999. pp. 405–454.

Song P, Bi X, Mellema DC, Manduca A, Urban MW, Greenleaf JF, Chen S. Quantitative Assessment of Left Ventricular Diastolic Stiffness Using Cardiac Shear Wave Elastography: A Pilot Study. J Ultrasound Med 2016a;:51–59. Available from: http://www.ncbi.nlm.nih.gov/pubmed/27208201

Song P, Bi X, Mellema DC, Manduca A, Urban MW, Greenleaf JF, Chen S, Hospital T. A Systematic Investigation of Feasible Acoustic Windows and the Impact of Myocardial Anisotropy for In Vivo Human Cardiac Shear Wave Elastography. IEEE Int Ultrason Symp Proc 2015;

Song P, Bi X, Mellema DC, Manduca A, Urban MW, Pellikka PA, Chen S, Greenleaf JF. Pediatric Cardiac Shear Wave Elastography for Quantitative Assessment of Myocardial Stiffness: A Pilot Study in Healthy Controls. Ultrasound Med Biol 2016b;42:1719–1729. Available from: http://www.umbjournal.org/article/S0301562916001484/fulltext

Song P, Manduca A, Zhao H, Urban MW, Greenleaf JF, Chen S. Fast Shear compounding using robust 2-D shear wave speed calculation and multi-directional filtering. Ultrasound Med Biol 2014a [cited 2014 Oct 31];40:1343–55. Available from: http://www.ncbi.nlm.nih.gov/pubmed/24613636

Song P, Urban MW, Chen S, Manduca A, Zhao H, Nenadic IZ, Pislaru S V, Pislaru C, Greenleaf JF. In Vivo Transthoracic Measurement of End-diastolic Left Ventricular Stiffness with Ultrasound Shear Wave Elastography : A Pilot Study. IEEE Int Ultrason Symp Proc 2014b;:109–112.

Song P, Zhao H, Manduca A, Urban MW, Greenleaf JF, Chen S. Comb-Push Ultrasound Shear Elastography (CUSE): A Novel Method for Two-Dimensional Shear Elasticity

Imaging of Soft Tissues. IEEE Trans Med Imaging 2012;31:1821–1832.

Song P, Zhao H, Urban M, Manduca A, Pislaru S, Kinnick R, Pislaru C, Greenleaf J, Chen S. Improved Shear Wave Motion Detection Using Pulse-Inversion Harmonic Imaging with a Phased Array Transducer. IEEE Trans Med Imaging 2013;32:2299–2310. Available from: http://www.ncbi.nlm.nih.gov/pubmed/24021638

Sonnenblick EH, Downing SE. Afterload as a primary determinant of ventricular performance. Am J Physiol 1963;204:604–610.

Starling EH. The Linacre Lecture on the Law of the Heart. London: Longmans, Green, & Company, 1918.

Strachinaru M, Bosch JG, van Dalen BM, van Gils L, van der Steen AFW, de Jong N, Geleijnse ML, Vos HJ, Chen S, Cosgrove D, Dietrich CF, Ding H, Amy D, Farrokh A, Ferraioli G, Filice C, Friedrich-Rust M, Nakashima K, Schafer F, Sporea I, Suzuki S, Wilson S, Kudo M. Cardiac Shear Wave Elastography Using a Clinical Ultrasound System. Ultrasound Med Biol 2017;43:753–764. Available from: http://linkinghub.elsevier.com/retrieve/pii/S0301562917301771

Tanter M, Bercoff J, Athanasiou A, Deffieux T, Gennisson J-L, Montaldo G, Muller M, Tardivon A, Fink M. Quantitative assessment of breast lesion viscoelasticity: initial clinical results using supersonic shear imaging. Ultrasound Med Biol 2008 [cited 2014 Dec 29];34:1373–86. Available from: http://www.ncbi.nlm.nih.gov/pubmed/18395961

Tanter M, Bercoff J, Sandrin L, Fink M. Ultrafast compound imaging for 2-D motion vector estimation: application to transient elastography. IEEE Trans Ultrason Ferroelectr Freq Control 2002;49:1363–1374. Available from: http://ieeexplore.ieee.org/lpdocs/epic03/wrapper.htm?arnumber=1041078

Tanter M, Fink M. Ultrafast imaging in biomedical ultrasound. IEEE Trans Ultrason Ferroelectr Freq Control 2014;61:102–19. Available from: http://www.ncbi.nlm.nih.gov/pubmed/24402899

Thomas JD, Rubin DN. Tissue harmonic imaging: Why does it work? J Am Soc Echocardiogr 1998;11:803–808. Available from: http://www.onlinejase.com/article/S0894-7317(98)70055-0/pdf

Thune JJ, Solomon SD. Left ventricular diastolic function following myocardial infarction. Curr Heart Fail Rep 2006;3:170–174.

Tiran E, Deffieux T, Correia M, Maresca D, Osmanski B-F, Sieu L-A, Bergel A, Cohen I, Pernot M, Tanter M. Multiplane wave imaging increases signal-to-noise ratio in ultrafast ultrasound imaging. Phys Med Biol IOP Publishing, 2015;60:8549–8566. Available from: http://stacks.iop.org/0031-9155/60/i=21/a=8549?key=crossref.0af5c4f84e9506dfd5a70e4eb26df274

Velagaleti RS, Pencina MJ, Murabito JM, Wang TJ, Parikh NI, D'Agostino RB, Levy D, Kannel WB, Vasan RS. Long-Term Trends in the Incidence of Heart Failure after Myocardial Infarction. Circulation 2008;118:2057–2062.

Venkatesh SK, Yin M, Ehman RL. Magnetic Resonance Elastography of Liver: Technique, Analysis and Clinical Applications. J Magn Reson Imaging 2013;37:544–555.

Vos HJ, van Dalen BM, Heinonen I, Bosch JG, Sorop O, Duncker DJ, van der Steen AFW, de Jong N. Cardiac Shear Wave Velocity Detection in the Porcine Heart. Ultrasound Med Biol 2017;43:753–764. Available from: http://linkinghub.elsevier.com/retrieve/pii/S0301562916304124

Wagner RF, Insana MF, Smith SW. Fundamental Correlation Lengths of Coherent Speckle in Medical Ultrasonic Images. IEEE Trans Ultrason Ferroelectr Freq Control 1988;35:34–44.

Wagner RF, Smith SW, Sandrik JM, Lopez H. Statistics of Speckle in Ultrasound B-Scans. IEEE Trans Sonics Ultrason 1983;30:156–163.

Waller AD. A demonstration of man of electromotive changes accompanying the heart's beat. J Physiol 1887;8:229–234.

Wassenaar PA, Eleswarpu CN, Schroeder SA, Mo X, Raterman BD, White RD, Kolipaka A. Measuring age-dependent myocardial stiffness across the cardiac cycle using MR elastography: A reproducibility study. Magn Reson Med 2016;75:1586–1593.

Weber KT. Cardiac interstitium in health and disease: The fibrillar collagen network. J Am Coll Cardiol Elsevier Masson SAS, 1989;13:1637–1652. Available from: http://dx.doi.org/10.1016/0735-1097(89)90360-4

Welch PD. The Use of Fast Fourier Transform for the Estimation of Power Spectra: A Method Based on Time Averaging Over Short, Modified Periodograms. IEEE Trans Audio Electroacoust 1967;15:70–73.

Yamakoshi Y, Sato J, Sato T. Ultrasonic Imaging of Internal Vibration of Soft Tissue under Forced Vibration. IEEE Trans Ultrason Ferroelectr Freq Control 1990;37:45–53.

Yancy CW, Jessup M, Bozkurt B, Butler J, Casey DE, Drazner MH, Fonarow GC, Geraci S a., Horwich T, Januzzi JL, Johnson MR, Kasper EK, Levy WC, Masoudi F a., McBride PE, McMurray JJ V, Mitchell JE, Peterson PN, Riegel B, Sam F, Stevenson LW, Tang WHW, Tsai EJ, Wilkoff BL. 2013 ACCF/AHA guideline for the management of heart failure: A report of the American college of cardiology foundation/american heart association task force on practice guidelines. J Am Coll Cardiol Elsevier, 2013;62:e147–e239. Available from: http://dx.doi.org/10.1016/j.jacc.2013.05.019

Zhao H, Song P, Meixner DD, Kinnick RR, Callstrom MR, Sanchez W, Urban MW, Manduca A, Greenleaf JF, Chen S. External Vibration Multi-Directional Ultrasound Shearwave Elastography (EVMUSE): Application in Liver Fibrosis Staging. IEEE Trans Med Imaging 2014;33:2140–2148.

Zile MR, Baicu CF, Gaasch WH. Diastolic heart failure--abnormalities in active relaxation and passive stiffness of the left ventricle. N Engl J Med 2004;350:1953–1959.

Zile MR, Baicu CF, Ikonomidis JS, Stroud RE, Nietert PJ, Bradshaw AD, Slater R, Palmer

BM, Van Buren P, Meyer M, Redfield MM, Bull DA, Granzier HL, LeWinter MM. Myocardial stiffness in patients with heart failure and a preserved ejection fraction contributions of collagen and titin. Circulation 2015;131:1247–1259.

Zile MR, Brutsaert DL. New concepts in diastolic dysfunction and diastolic heart failure: Part I: Diagnosis, prognosis, and measurements of diastolic function. Circulation 2002;105:1387–1393.

Appendices

APPENDIX A. Gelatin Phantoms

A.1. Procedure for Making Gelatin Phantoms

Gelatin phantoms are made with a combination if water, gelatin, Metamucil (for ultrasound scattering), propanol, and glycerol. The following equation represents how much water, in mL, is required to make a 1L phantom.

$$H_20 = 1000\ - Gel - Met\ - 0.803 * Prop - 1.26 * Glyc \qquad (A.1)$$

Ingredients

1. Water (H_20) measured in milliliters (mL).
2. Gelatin (Gel) measured in grams (g).
3. Metamucil (Met) measured in g.
4. Propanol ($Prop$) measured in mL.
5. Glycerol ($Glyc$) measured in mL.

A typical amount of ingredients for a 7% gelatin phantom is shown below.

1. 808 mL (H_20)
2. 70 g (Gel)
3. 20 g (Met)
4. 25 mL ($Prop$), optional
5. 65 mL ($Glyc$), optional

The procedure to make the tissue mimicking phantom requires multiple beakers, hotplates, and glass thermometers, pam, a large container filled with water, and a small container to hold any gelatin phantoms. Do not heat up the gelatin mixture above 60 C. The procedure for making the phantoms is partially taken from (Geliko 2008). It listed below.

Procedure to make Gelatin Phantom

1. Collect deionized water
2. Separate water into two different beakers, one containing about 250 mL of water for gelatin mixture and one with the remaining water which will be used for the Metamucil mixture.
3. While stirring vigorously, quickly add the Metamucil into its water beaker. Stir until it forms a solution.
4. Strain the Metamucil solution into a different beaker and heat to no more than 60 C.
5. Into the first beaker containing only water, add the propanol and stir (optional).
6. Quickly dump the gelatin in the beaker containing propanol and water. Stir vigorously until all gelatin is wetted and saturated. Should happen quickly.
7. As soon as the gelatin is saturated, add it to the beaker containing the Metamucil solution. There is now only one beaker.
8. Add glycerol to the mixture (optional).

9. Remove any clumps.
10. To degas the gelatin mixture, leave heated to no more than 60 C. Do not stir.
11. Prepare the small container to hold the phantom by spraying it with pam. Let sit until it creates an even layer. (optional, only if you want to take the phantom out of the container easily)
12. In a large container pour water. The water is to help the gelatin phantom cool evenly and to catch gelatin as it spills out of the small container.
13. Place the small container, which will hold the phantom, in the large container with water.
14. Pour, smoothly, the warm gelatin solution into the small container. Pour on a spatula or glass rod taking care to limit the amount of bubbled formed. Overfill the small container and have the overflowing gelatin drip into the water. Because any gas bubbles will be at the top of the phantom, the small later with gas bubbles will overflow into the water and create a smooth degassed top later of the phantom and allow for ultrasound imaging.
15. To cool the phantom, cover and place into a refrigerator for at least 6 hours, or leave to set at room temperature for at least 12 hours.

Extra notes: The gelatin phantom will continue to solidify for a few days. If testing immediately after preparing the phantom, make sure all tests are done relatively quickly of each other.

A.2. Inclusion Phantoms.

1. Place a small glass test tube through the side of the container holding the gelatin phantom. The test tube is placed horizontally. Don't worry about small gaps in the container where the test tube is inserted. The cold water will quickly solidify the gelatin and fill the holes to limit leakage.
2. When the gelatin phantom has solidified, slowly remove the glass test tube. The gelatin phantom may cave in as the removal of the test tube will create a vacuum. Poke a hole with a needle into the gap behind the tube to allow air in.
3. Place the phantom sideways so the hole is facing up.
4. Let the first phantom sit at room temperature to warm up so it does not immediately solidify the gelatin mixture for the inclusion.
5. Let the gelatin solution prepared for the inclusion sit at room temperature until it is only warm and not hot. If it is hot it will melt the 1st phantom.
6. Pour the inclusion gelatin into the hole of the 1st phantom which was created by the removal of the test tube. The heat from the gelatin solution will slightly melt the internal surface of the phantom and allow for a smooth transition from the inclusion to the background gelatin of the phantom.
7. Place in fridge to let set.

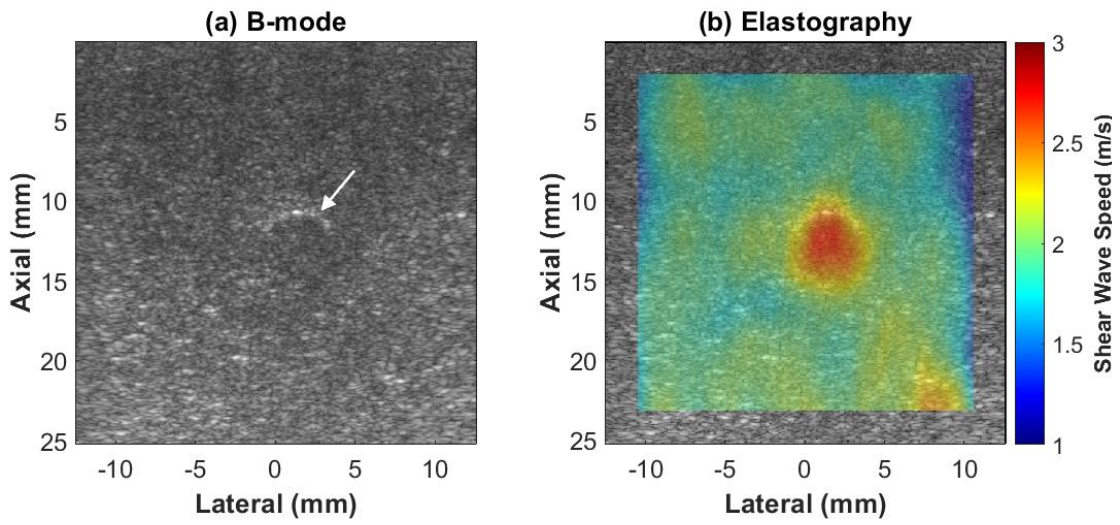

Figure A.1 Example of inclusion Phantom. (left) B-mode image. (right) SWS image. Different concentrations of gelation produced a different stiffness for the inclusion and the background. There is a difficulty distinguishing the inclusion from the background in the B-mode image, but this is seen in the SWS image. The 5mm inclusion was made with a glass stir rod rather than a test tube.

APPENDIX B. Computer-Generated Waves

Chapter 3 performed directional filtering of shear waves and estimated the speed of propagation of the waves by the ratio of spatial and temporal partial derivatives. Validation of these methods was done using computer-generated waves which could be coded to propagate in different direction. MATLAB code for generating these waves is shown in Figure B.1.

```
% Wave Generation
%
% By: Aaron J. Engel

numRows = 256;
numCols = 256;
numFrames = 128;

waves = zeros(numRows,numCols,numFrames, 'single');
[f1, f2] = freqspace(256, 'meshgrid');
index = 1;
speedIndex = 1;
for phase = 126:-1:1

    % waves(:,:,index) = waves(:,:,index) + sin(2*pi.*((f1+1).^2)+phase*2*pi/20); % right ↙
moving wave
    % waves(:,:,index) = waves(:,:,index) + sin(2*pi.*((f1-1).^2)+phase*2*pi/20); % left ↙
moving wave
    % waves(:,:,index) = waves(:,:,index) + sin(2*pi.*((f2+1).^2)+phase*2*pi/20); % down ↙
moving wave
%     waves(:,:,index) = waves(:,:,index) + sin(2*pi.*((f2-1).^2)+phase*2*pi/20); % up ↙
moving wave
    waves(:,:,index) = waves(:,:,index) + sin(1/speedIndex*2*pi.*sqrt((f2).^2+(f1).^2) ↙
+phase*2*pi/20); % diagonal wave

    index = index + 1;
end

% Wave Visualization
for n = 1:128
    figure(1)
    clf
    imagesc(waves(:,:,n))
    pause(0.01)
end
```

Figure B.1 MATLAB code used to generate a video of waves propagating through space.

APPENDIX C. Materials Testing with an Axial Compression Test

An axial compression test can be used to find the Young's Modulus (stiffness) of the material.

$$E = \frac{\sigma}{\varepsilon}, \qquad (C.1)$$

where E is Young's Modulus, σ is stress, and ε is strain. Stress and strain are defined as:

$$\sigma = \frac{F}{A}, \qquad (C.2)$$

$$\varepsilon = \frac{\Delta l}{L}, \qquad (C.3)$$

where F is the force measured during axial compression and A is the surface area where force is applied, Δl is the amount of axial compression and L is the initial length of the sample. The Young's Modulus can be measured from gelatin phantoms using the following procedure.

Procedure to calculate Young's Modulus

1. Materials testing is performed on small cubes cut from the phantom. Cut five small cubes (about 1 cm on each side) from the center of the phantom.

2. Measure the length, width, and height of each cube and record the measurements in units of meters.
3. Place a single block on the testing bed as seen in Figure C.1.
4. Using a TMS-Pro with a small load cell (2 Newtons), compress the sample at 2 mm/s for a distance of 1 mm. If compression is slower than 2 mm/s the sample may experience creep during testing and Young's modulus will be underestimated.
5. Record the Force and Displacement as measured from the load cell. Record Force in Newtons and Displacement in meters.
6. Export the raw data, for future processing.
7. For each compression, record the starting and ending displacements in case the exported data is corrupted.
8. $\sigma = \frac{Force_{end} - Force_{start}}{(length)(width)}$
9. $\varepsilon = \frac{Position_{end} - Position_{start}}{height}$
10. $E = \frac{\sigma}{\varepsilon}$
11. Record the mean and standard deviation of the Young's modulus for the five samples.
12. Record the shear wave speed as $SWS = \sqrt{\frac{E}{3000}}$. The factor of 3000 is 3 times the density of the material (1000 kg/m^3).

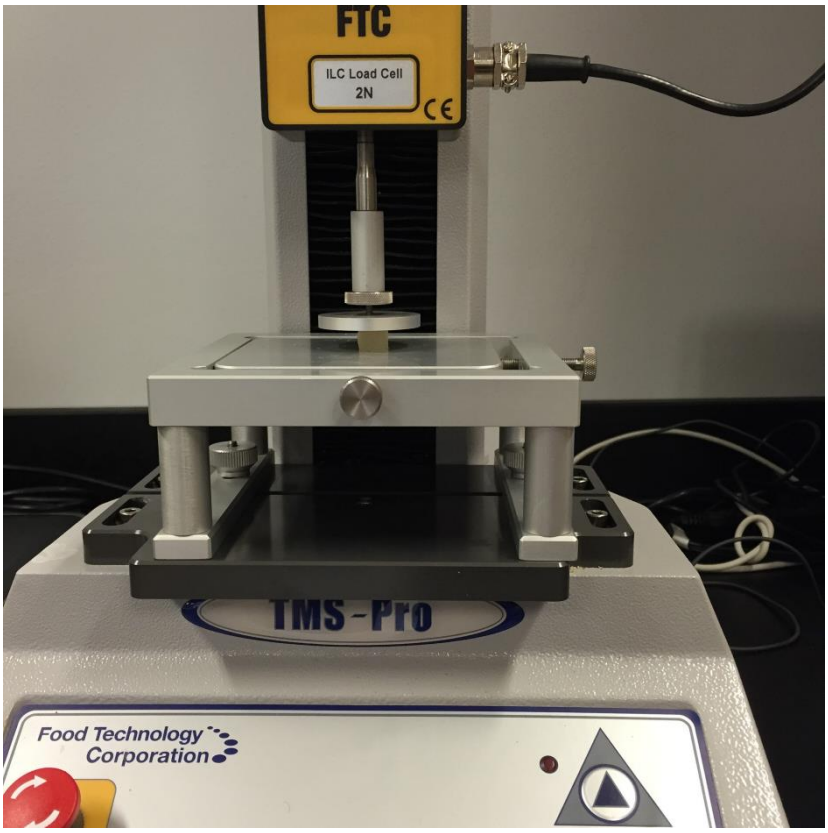

Figure C.1 Compression test on a small block cut from a gelatin phantom.

APPENDIX D. Spectral Doppler

The recommended methods for the quantification of tissue velocity in a clinical echocardiogram assessment is through the use of spectral Doppler techniques. Spectral Doppler, as it sounds, is a method which measures the frequency spectrum of tissue movement, where the frequency spectrum is then related to the tissue velocity through the Doppler equation:

$$f_{Doppler} = \frac{2 f_c v \cos\theta}{c}, \qquad (D.1)$$

where $f_{Doppler}$ is the Doppler frequency, f_c is the center frequency of the recorded ultrasound pulse, v is the axial tissue velocity, c is the speed of sound (1540 m/s), and θ is the angle between the ultrasound beam and the true direction of tissue motion. The angle is used as a correction factor for the calculated velocity measurement because only the axial tissue velocity can be measured.

The frequency spectrum of tissue movement is estimated by **1)** recording several (~1000) consecutive transmit receive events and reconstructing the IQ data for a single point in space, and **2)** performing a Short-time Fast Fourier Transform (STFFT) through time for the reconstructed data. A STFFT is done by breaking the entire data set into smaller and overlapping blocks of data and them calculating the frequency spectrum on the smaller blocks of data. This is similar to Welch's method of estimating the PSD of a signal except here each velocity spectrum is plotted and displayed column by column based on the average time of the data in

the block. Because spectral Doppler is performed at one spatial location through time it has a high temporal and spatial resolution.

In the study, the data blocking size was 32 temporal pixels long and the overlap size was 31 temporal pixels. A Hanning window was applied on each block of data to reduce the sidelobes in the velocity spectrum. Because ultrasound data were acquired at a high frame rate for a large region of space, a 9x9 pixel (4 × 4 mm) spatial average was taken prior to the STFFT. Figure D.1 shows the spectral Doppler tissue velocity measurement along with the phase based autocorrelation tissue velocity measurement. Three locations along the IVS are shown. There is a general agreement in the two velocity measurements. The borders on the spectral Doppler measurement are reflective of the 32-temporal pixel block size.

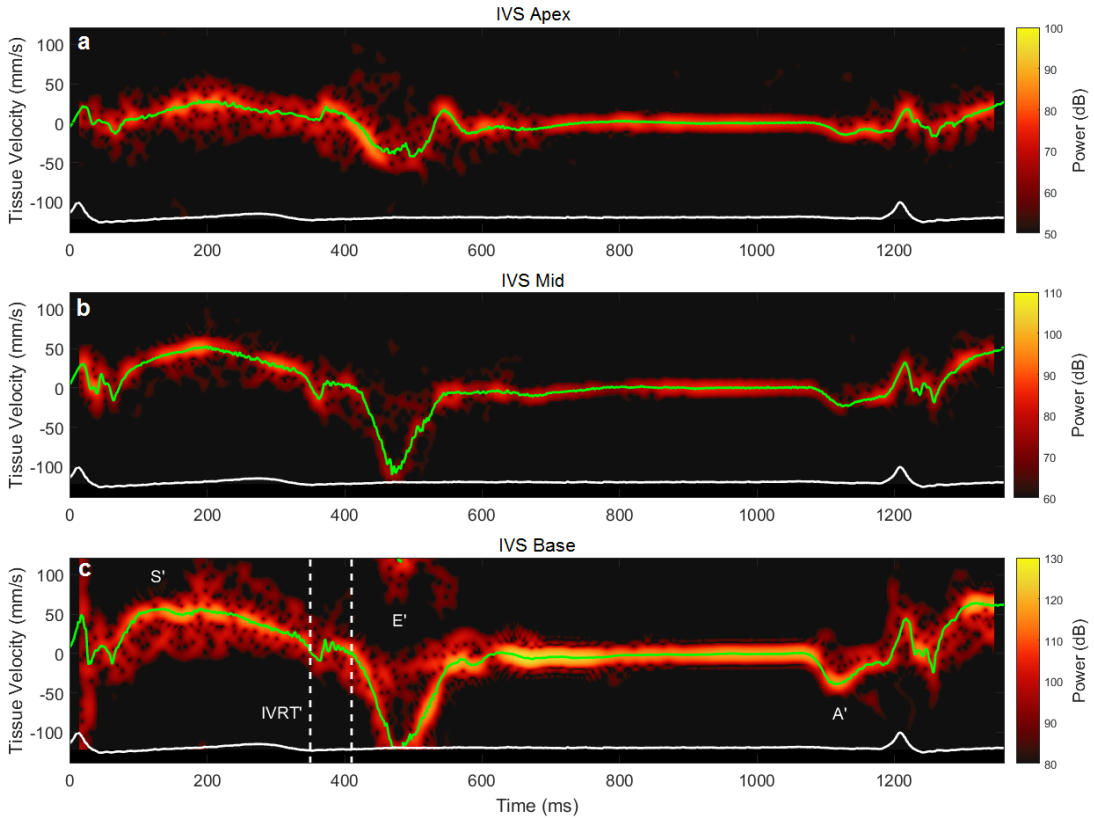

Figure D.1 Tissue velocity reconstructed at three points along the IVS. Tissue velocity derived from spectral Doppler is in the background and tissue velocity from the autocorrelation technique is the solid green line.

APPENDIX E. Institutional Review Board Consent Form

All participants in the studies which were performed and presented in this dissertation provided their written informed consent before their inclusion into the studies. The following pages are the copy of the informed consent form which was approved by the University of Nebraska-Lincoln IRB.

University of Nebraska Lincoln

DEPARTMENT OF BIOLOGICAL SYSTEMS ENGINEERING

RESEARCH CONSENT FORM

Project Title: Ultrasound Imaging of Cardiac Motion

IRB#: 15713

Principal Investigator: Dr. Gregory R. Bashford

Please read this information carefully. It tells you important things about this research study. A member of our research team will talk to you about taking part in this study. If you have any questions at this time, please feel free to ask us.

Take your time to decide. Feel free to discuss the study with your family and friends before you make your decision.

To help you decide if you want to take part in the study, you should know:

- Taking part in this study is completely voluntary.
- You can choose not to participate
- You are free to change your mind at any time if you choose to participate.
- Your decision won't cause any penalties or loss of benefits to which you're otherwise entitled.

For purposes of this form,

If you decide to take part in this research study, you will sign this consent form to show that you want to take part. We will give you a copy of this form to keep.

Contact Information

You can contact …	At …	If you have questions or about …
Principal Investigator: Gregory R. Bashford	**Phone:** (402) 472-1745 **Address:** 230 L.W. Chase Hall East Campus Lincoln, NE 68583	• Study test and procedures • Research-related injuries or emergencies • Any research-related concerns or complaints • Withdrawing from the study • Materials you receive • Research-related appointments
UNL Institutional Review Board (IRB)	**Phone:** (402) 472-6965	• Rights of a research participant • Any research-related concerns or complaints

1. Why are you being asked to take part in this study?

You are being asked to take part in this study because you are over 19 years old and have no history of cardiovascular disease.

The goal is to have 40 healthy volunteer participate in this study at UNL.

2. Why is this research being done?

We are evaluating an ultrasound-based technique to measure the stiffness of your heart muscle. Using the natural motion of your heart during a single heartbeat, we will measure the stiffness of your heart. We will validate this technique using other existing techniques which use ultrasound to noninvasively measure the stiffness of your heart muscle.

3. Information you should know

Who is funding this Research Study?

This study is being funded by internal UNL funding.

Information Regarding Conflict of Interest:

None of the investigators have any conflicts of interest related to this research study.

4. How long will you be in this research study?

You will be in this study for 1 session. This session will take no longer than 60 minutes.

5. What will happen to you while you are in this research study?

If you agree to participate in this study, you will have one data collection session. In this session, we will first measure your height, weight, and blood pressure. We will then acquire

electrocardiogram (ECG) signals from the surface of your body. To acquire ECG data, three self-adhesive electrodes the size of a quarter will be placed on the surface of your body. Two electrodes will be placed on your wrists and a third electrode will be placed on one elbow. Before placing the electrodes on your body, the skin where they will be place will be cleaned. We will then use ultrasound to image the motion of your heart. To do this, gel will be applied to a wand-like ultrasound transducer, this transducer will then be gently placed on the surface of your body near your heart. You may be asked lay on your left side in order to obtain an optimal image of your heart. The sonographer will sit on your right side and may use their body weight to help you stay in an optimal position for imaging. You may be asked to hold your breath during the measurements. We will use the ECG signal to synchronize the ultrasound imaging to your heart beat. All the measurements are completely noninvasive.

6. What are the possible risks or discomforts from being in this research study?

The ultrasound techniques used for this study meet the safety requirements set by the Food and Drug Administration (FDA). The risks of the ultrasound measurements in this study are not different from what you would have at a routine clinical ultrasound exam. All the ultrasound techniques are going to be done on the surface of your body, which is noninvasive. Breath holds may be required and will be spaced according to your comfort. You may be uncomfortable removing articles of clothing, a gown will be provided

7. Are there reasons you might leave this research study early?

Taking part in this research study is voluntary. You may decide to stop at any time. You should tell the researcher if you decide to stop and you will be advised whether any additional tests may need to be done for your safety.

In addition, the researchers, or UNL may stop you from taking part in this study at any time:

- If you do not follow the study procedures
- If the study is stopped

We will tell you about any new information that may affect you willingness to stay in the research study.

8. What if you are injured from your participation in this research study?

Where to get help:

If you think you have suffered a research-related injury, you should promptly notify the Principal Investigator listed in the Contact Information at the beginning of this form.

9. What are the possible benefits from being in this research study?

There are no known benefits to participating in this study. It is for the benefit of research.

10. What alternative do you have if you choose not to participate in this research study?

This study is only being done to gather information. You may chose not to take part in this study.

11. What tests or procedures will you need to pay for if you take part in this research study?

You will not need to pay for tests and procedures which are done for this research study. These tests and procedures are:

- Experimental ultrasound
- ECG

12. Will you be paid for taking part in this research?

You will receive nothing of monetary value for your participation in this study.

ENROLLMENT AND PERMISSION SIGNATURES

Your signature documents your permission to take part in this research.

Printed Name	/ / Date	: AM/PM Time

Signature

Person Obtaining Consent

- I have explained the research study to the participant.
- I have answered all questions about this research study to the best of my ability.

Printed Name	/ / Date	: AM/PM Time

Signature